Ruprecht-Karls-Universität Heidelberg
Naturwissenschaftlich-Mathematische Gesamtfakultät

Dynamics of chromatin structure and nuclear multiprotein complexes investigated by quantitative fluorescence live cell microscopy and computational modeling

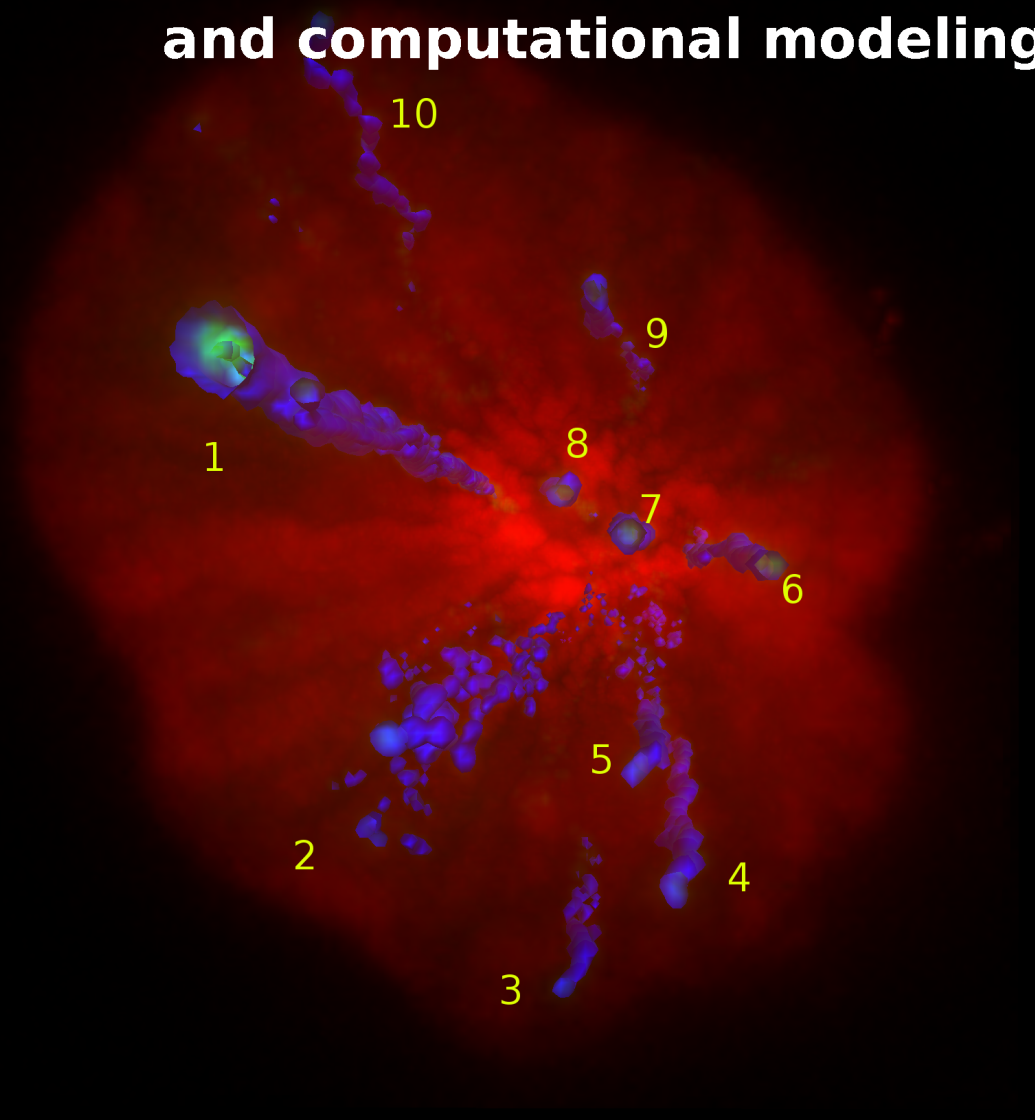

presented by
Diplom-Biochemiker Norman Constantin Kappel
born in Worms, Germany
July 2009

Dissertation

submitted to the combined faculties for the natural sciences and for
mathematics of the Ruperto-Carola University of Heidelberg, Germany
for the degree of Doctor of Natural Sciences

presented by:
Diplom-Biochemiker Norman Constantin Kappel
born in Worms, Germany
Oral examination: July 2009

Dynamics of chromatin structure and nuclear multiprotein complexes investigated by quantitative fluorescence live cell microscopy and computational modeling

Referees: Prof. Dr. Roland Eils
Prof. Dr. Harald Herrman-Lerdon

Acknowledgements

I wish to thank Prof. Dr. Roland Eils for welcoming me to the unique and highly dynamic research environment he has created within, both, German Cancer Research Center and Bioquant. He has given me a perspective into quantitative biology at the interface of cell biology, physics and computer science. I would like to thank him for giving me the time and guidance I needed to develop my own ideas and for his enthusiastic support regarding all aspects of this work. Last but not least I have benefited from his numerous collaborations which were essential in creating this work.

I thank Prof. Dr. Harald Herrmann-Lerdon for refereeing this work and for numerous suggestions and ideas as well as practical advice for conducting the experimental parts of this work. He also supported me with his profound overview of cell biology and often pointed me into the direction of interesting work done in my field. In this way his support helped me to shape particularly the work done on chromatin dynamics.

I wish to thank Prof. Dr. Peter Lichter for sharing some of his laboratory facilities and for being a member of my PhD commitee.

I also wish to thank Prof. Dr. David Robinson for being a member of my PhD commitee.

I owe special thanks to Dr. Joel Beaudouin who has been of invaluable support during this work. His critical advice, many fruitful discussion and practical support, both in the lab as well as interpreting data have been of great importance.

Thanks to Prof. David Spector and Dr. Yi-Chun Chen at Cold Spring Har-

bour Laboratories for a fruitful collaboration on the dynamics of promyelotic leukemia bodies.
Thanks to Dr. Markus Ulrich who collaborated with me on the chromatin dynamics project and with whom I collaborated on the design as well as implementation of Tropical.
Thanks to Dr. Evgeny Gladilin, Dr. Stefan Wörz for collaborations on nuclear mechanics, cell tracking and image registration techniques.
I thank Dr. Michaela Reichenzeller for sharing her experience on confocal microscopy, cell culture and molecular biology as well as for experimental collaboration and critical discussions on numerous parts of my projects. I also thank her for good comradeship and her cheerful character.
Many thanks to Dr. Matthias Weiss and Dr. Gernot Guigas for sharing their FCS module and giving me a practical introduction into the FCS technique.
I thank Dr. Bernd Kalbfuss for introducing me to FRAP experiments and numercial simulations for their quantitative analysis.
Thanks to Dr. Christian Bacher for advice on particle tracking with TIKAL.
Thanks also belong to Dr. Hauke Busch for many fruitful discussions on topics related to biophysics and systems biology.
Many thanks also to Karina Drobbe and Johannes Fredebohm, two internship students who created some of the primary data for the project on nuclear H1° dynamics under my supervision.
I also thank all members of the Herrman-Lerdon lab as well as all members of the theoretical bioinformatics department for creating a good working atmosphere throughout my thesis and for giving me a good time.

Zusammenfassung

Die Biologie hat sich schnell in eine datengetriebene, quantitave Wissenschaft verwandelt. Die Anforderungen an die biologische Bildgebung bewegt sich daher in Richtung quantitativer Annotation von Genen *in vivo*. In dieser Dissertation habe ich die räumlich-zeitliche Verteilung, sowie deren molekulare Interaktionen von Proteinpopulationen wie auch von Multiproteinkomplexen untersucht. Ich habe Methoden entwickelt, mit denen man biophysikalische Parameter, wie Diffusionskoeffizienten, anomale Diffusion und das Bindungsgleichgewicht von Proteinpopulationen mit Hilfe von Fluoreszenzphotobleichen, numerischer Simulation und Parameterschätzung bestimmen kann. Bei der Analyse von Multiproteinkomplexen erweiterte ich bestehende Ansätze des *Single-particle-tracking*, um den exakten Zeitpunkt von Dynamikänderungen einzelner Partikel in lebenden Zellen automatisch detektieren zu können. Dabei ist es mir gelungen, quantitative Parameter, wie Diffusionskoeffizienten, anomale Diffusion, Geschwindigkeit und Chromatininteraktion zu bestimmen. Die nukleäre Proteinpopulation, die ich untersuchte, war das Linkerhiston H1° der Maus in Form von GFP-Konstrukten. Ich konnte zeigen, daß Diffusion und Bindung von H1°-GFP an Chromatin mit Fluoreszenzphotobleichen und numerischer Modellierung untersucht werden kann. Somit erhielt ich die Diffusionskoeffizienten von Wildtyp-H1°, sowie von sieben Punktmutanten mit jeweils unterschiedlicher Bindungsaffinität, die von $D \sim 0.01 \mu m^2/s$ (höchste Affinität) bis $D \sim 0.1 \mu m^2/s$ (niedrigste Affinität) reichte. Außerdem konnte ich die nicht gebundene Fraktion abschätzen, die entsprechend von $\sim 400\ ppm$ bis $\sim 3000\ ppm$ reichte. Als Beispiel für

große Multiproteinkomplexe wählte ich *PML nuclear bodies* (PML NBs), die nach ihrem Hauptbestandteil, dem Promyelotischen-Leukämie-Protein benannt sind. Ich untersuchte exakt deren dynamische Bewegung während der frühen Mitose, die von der Prophase bis zur Prometaphase reicht. Es konnte während dieses Zeitraums eine dramatische globale Zunahme in der Beweglichkeit der PML NBs festgestellt werden, bei der die Diffusionskonstante von $D \sim 0.001 \mu m^2/s$ während der Interphase auf $D \sim 0.005 \mu m^2/s$ während der Prophase ansteigt. In ähnlicher Weise erhöhten sich die Geschwindigkeiten von $v \sim 0.7 \mu m/min$ auf $v \sim 1.4 \mu m/min$, was mit einer Abnahme in subdiffusiver Bewegung (also anomaler Diffusion) einher ging. Ich konnte zeigen, daß eine Loslösung von Chromatin die wahrscheinlichste Ursache für die Zunahme der Beweglichkeit darstellt im Gegensatz zu mechanischem Fluss von Nukleoplasma oder zu Chromatinverdichtung. Schließlich konnte ich die genaue zeitliche Abfolge der Beweglichkeitszunahme mit anderen zellulären Ereignissen in Verbindung bringen. So trat die Zunahme der Beweglichkeit von PML NBs hauptsächlich nach dem Eindringen von Zyklin B1 in den Zellkern auf, welches die Zelle unumkehrbar auf Mitose programmiert, sowie vor der Auflösung der Zellkernmembran.

Abstract

Biology has rapidly been transformed into a mainly data-driven, quantitative science. Demands on biological imaging are moving towards quantitative annotations of genes *in vivo*. In this work I have studied in detail the spatio-temporal distribution and the molecular interaction of protein ensembles as well as of multiprotein aggregates. I have provided the methodology to estimate biophysical parameters such as diffusion coefficients, anomalous diffusion and the free fraction in the binding equilibrium of protein ensembles using fluorescence photobleaching analysis and numcerical modeling and parameter estimation. On the side of protein complexes I have extended existing single particle tracking approaches to allow to automatically detect the exact timing of mobility changes of single particles in live cells. Here, I was able to provide quantitative parameters also on the diffusion coefficient, anomalous diffusion, velocity and chromatin interaction. The nuclear protein ensemble I studied was murine linker histone H1° fused to GFP. I was able to show that diffusion and binding of H1°-GFP to chromatin can be addressed using photobleaching analysis and numcerical modeling. I have thus obtained diffusion coefficients for wild-type H1° and seven point mutants with differential binding affinity ranging from $D \sim 0.01 \mu m^2/s$ (strongest binder) to $D \sim 0.1 \mu m^2/s$ (weakest binder). Likewise, I was able to estimate the free fraction to range from $\sim$ 400 ppm to $\sim$ 3000 ppm. Exemplary of large multiprotein complexes I chose PML nuclear bodies (PML NBs), named after their constituent promyelotic leukemia protein. I studied in detail their dynamic mobility during early mitosis, ranging from prophase to prometaphase.

A dramatic global increase in PML NB mobility was found during this period with the diffusion coefficient increasing from $D \sim 0.001 \mu m^2/s$ at interphase to $D \sim 0.005 \mu m^2/s$ at prophase. Similarly, velocities increased from $v \sim 0.7 \mu m/min$ to $v \sim 1.4 \mu m/min$ and concomittant with a loss in subdiffusive motion. I was able to establish loss of tethering to chromatin as the most likely reason behind this increase as opposed to material flow or chromatin condensation. Lastly, I was also able to relate the timing of the mobility increase to other important cellular events. The increase of PML NB mobility predominantly occured after nuclear entry of cyclin B1, which irreversibly commits the cell to mitosis, and before nuclear envelope breakdown (NEBD).

Declaration

Some portions of this work and some materials have been created in collaboration with other scientists inside and outside the group of Roland Eils. All other portions of this work have been created solely by myself. To indicate the origin of the work a declaration is provided here: The work on histone H1° dynamics (chapter 4.1) is based on originally three cell lines with mutants of histone H1° of different chromatin affinity fused to GFP. These cell lines were kindly provided by Tom Misteli. As the project grew, seven new cell lines were provided by his lab. I conceptualized the project under supervision of Roland Eils, planned and conducted all cell culture work, all image acquisition and processing by myself with experimental support by two internship students by the end of the project. The quantitative analysis of the FRAP experiments was conducted by myself using the self-developed software TROPICAL. I was critically involved in the design as well as implementation of this software. On the latter I collaborated with Markus Ulrich, Stefan Hetzel and Jochen Ulrich, all working in the lab of Roland Eils at the time [181]. To demonstrate the utility of TROPICAL material using the same constructs has appeared in the thesis of Markus Ulrich [182]. The primary data used there is not the same as in this work. I used a strategy for estimation of the bound fraction of reaction-diffusion systems described by Joel Beaudouin, a post-doctoral fellow at the group of Roland Eils [20].
The work on the dynamics of promyelotic leukemia bodies (chapter 4.2) during mitosis was spurred by David Spector and Yi-Chun Chen who was one of his PhD students at the time. The primary image data, control ex-

periments with Western blot analysis, treatments with chemical drugs, co-transfection with cyclin B1 and IBB contructs and all cell culture work was done in the lab of David Spector. My part in that work was to design and conduct the image processing workflow for noise reduction, image registration and single particle tracking. For this I developed several ImageJ macros and used the TIKAL software developed by Christian Bacher, formerly a PhD student at the Eils group [14]. I also designed and implemented the classification scheme of movement types using mean square displacement analysis similar to that previously published by the group of Roland Eils in collaboration with David Spector and Tom Misteli [180, 54]. Automatic detection of changes in diffusion coefficient during mitosis was done using a customized maximum likelihood estimation scheme based on work by the group of H. Yang [189]. I adapted this method, which was developed for the analysis if photon traces from single molecule spectroscopy, to single particle tracking in biology and implemented a number of MATLAB functions to apply and validate the method. I was also instrumental in the interpretation of the quantitative results gained from MSD classification and MLE-based detection of changes in diffusive dynamics.

To Martina

Publications

During this thesis the following publications with my contribution have appeared:

Peer-reviewed papers

Markus Ulrich †, Constantin Kappel †, Joel Beaudouin, Stefan Hezel, Jochen Ulrich and Roland Eils. Tropical—parameter estimation and simulation of reaction–diffusion models based on spatio-temporal microscopy images. *Bioinformatics* (2006) 22:2709-2710; † These authors are mentioned as joint first authors in the publication. I contributed to the conceptualization and implementation of the software Tropical, I also contributed to figure 1 out of 1 and to the model describing the B23 reaction-diffusion system.

Yi-Chun M. Chen, Constantin Kappel, Joel Beaudouin, Roland Eils and David L. Spector. Live cell dynamics of PML nuclear bodies upon entry into and exit from mitosis. *Mol. Biol. Cell* (2008) 19:3147–3162. I contributed to figures 2, 3, 5, 6, 7 and supplementary figure 1 out of 11 in total (including 3 supplementary figures). My contributions was all of the image processing, image registration, single particle tracking, mean square displacement analysis, classification of movement types, classification of PML NB movement into sub-phases during early mitosis, automated detection of break points in trajectories as well as interpreting the quantitative results.

Conference papers

Dietmar Volz , Martin Eigel , Chaitanya Athale , Peter Bastian , Harald Herrmann-Lerdon , Constantin Kappel and Roland Eils. Spatial Modeling and Simulation of Diffusion in Nuclei of Living Cells. *Lecture Notes in Computer Science* (2004):161-171. I reviewed, edited and submitted the material and presented the paper at the conference on *Computational Methods in Systems Biology* (2004) in Paris.

Evgeny Gladilin, Constantin Kappel, Roland Eils. Motion Detection and Pattern Tracking in Microscopical Images Using Phase Correlation Approach. *Proc. of SPIE* (2006) 6512:65121V1-9. I contributed to figures 3 and 4 out of 4.

Ilhan Kim , Siwei Yang , Pierre Le Baccon , Edith Heard , Yi-Chun Chen , Constantin Kappel , Roland Eils , and Karl Rohr. Non-rigid temporal registration of 2D and 3D multi-channel microscopy image sequences of human cells. *International Symposium on Biomedical Imaging* (2007):1328-1331. I contributed to 2 out of 3 Figures in the paper.

Il-Han Kim, Siwei Yang, Patricia Le Baccon, Edith Heard, Constantin Kappel, Roland Eils, Karl Rohr. Non-rigid Temporal Alignment of 2D and 3D Multi-channel Microscopy Image Sequences of Human Cells. *Bildverarbeitung für die Medizin* 2007: 16-20

Stefan Wörz, Constantin Kappel, Roland Eils and Karl Rohr. Model-based segmentation and quantification of fluorescent bacteria in 3D microscopy live cell images. *Proc. SPIE Medical Imaging* (2007).

Posters

Constantin Kappel, Markus Ulrich, Tom Misteli, Bernd Kalbfuss, Roland Eils. Spatial modeling of protein mobility in living cells. *International conference on systems biology* (2004), Heidelberg.

Constantin Kappel, Michaela Reichenzeller, Markus Ulrich, Harald Herrman-Lerdon, Roland Eils. Live cell imaging in a FlAsH: Low molecular weight protein tags for microscopy. Annual meeting of histochemical society, Nordwijkerhout (2005).

Contents

Chapter 1

Introduction

1.1 Biology of the cell nucleus

"The nucleus is the defining feature of eukaryotic cells" ([178]). - This quotation was true already in 1831 when the botanist Robert Brown first coined the term "nucleus" and it is all the more true today. While the nucleus has been viewed for a long time essentially as a liquid-filled bag, which contains a more or less homogenous mixture of chromatin and its constituent proteins this view has now increasingly been replaced by the concept of a highly organized and tightly regulated structure. This structure, possessing a nuclear envelope and putatively its own nucleoskeleton, appears almost like a "cell-in-cell"-type of organelle. Considering its main function as the storage site of genetic information and partitioner of transcription and translation this prominent postition makes sense. Important cellular events, such as DNA replication, RNA transcription and processing as well as biogenesis of ribosome subunits all take place inside the nucleus. This biological activity implies that there is a continuous flux of macromolecules between the nucleoplasm and the cytoplasm, such as export of mRNA or import of histones during S phase to package newly replicated DNA. The nucleus is subject to dramatic reorgani-

sation throughout the cell cycle. In particular during mitosis (see chapter 1.3) the nuclear chromatin content condenses thereby revealing individual chromosomes, the nuclear envelope breaks down and many nuclear constituents, such as PML nuclear bodies, at least partially disassemble and reform after mitosis. Chromatin compaction occuring in complex with histones which regulate this process serves chromatin segregation into daughter cells. These changes are mostly driven by postranslational modifications of histone proteins as well as covalent modifications of DNA bases themselves (see chapter 1.2). Heterochromatin is stabilized by dozens of candidate genes. One of the best known markers for heterochromatin is HP1. It is thought of as an adaptor protein interacting with a large number of proteins many of which are involved in heterchromatin formation or stabilization. Among these interaction partners are components of the SWI/SNF complex ([101]), lamin-B receptor (LBR) at the nuclear envelope ([197]) and Sp100, a prominent component of PML nuclear bodies (PML NBs) ([158]). The interaction with LBR may help to explain the accumulation of heterochromatin at the nuclear periphery.

Nuclear bodies, entities occuring mostly during interphase, represent accumulation sites for proteins with specific functions: PML NBs, interchromatin granule speckles, centromeric heterochromatin, PcG domains as well as Cajal bodies. Arguably, the prominent nucleolus may be viewed as an especially large and complex nuclear body. For details on PML NBs see chapter 1.4.

The nucleolus forms around tandem repeats of ribosomal genes and is the site of rRNA transcription, processing and ribosome subunit assembly. It breaks down during mitosis and reforms during interphase while the cell is actively expressing genes. Next to rRNA synthesis by RNA Polymerase I nucleoli are involved in the biochemical modification of rRNA, such as 2'-O-Ribosyl-methylation and pseudo-uridine formation. In this it is aided by small nucleolar ribonucleoproteins (snoRNPs).

At the beginning of this work the nucleus was known to possess a highly ordered spatial organization consisting of chromosome territories, nucleoli, interchromatin granule clusters and a diverse assortment of nuclear

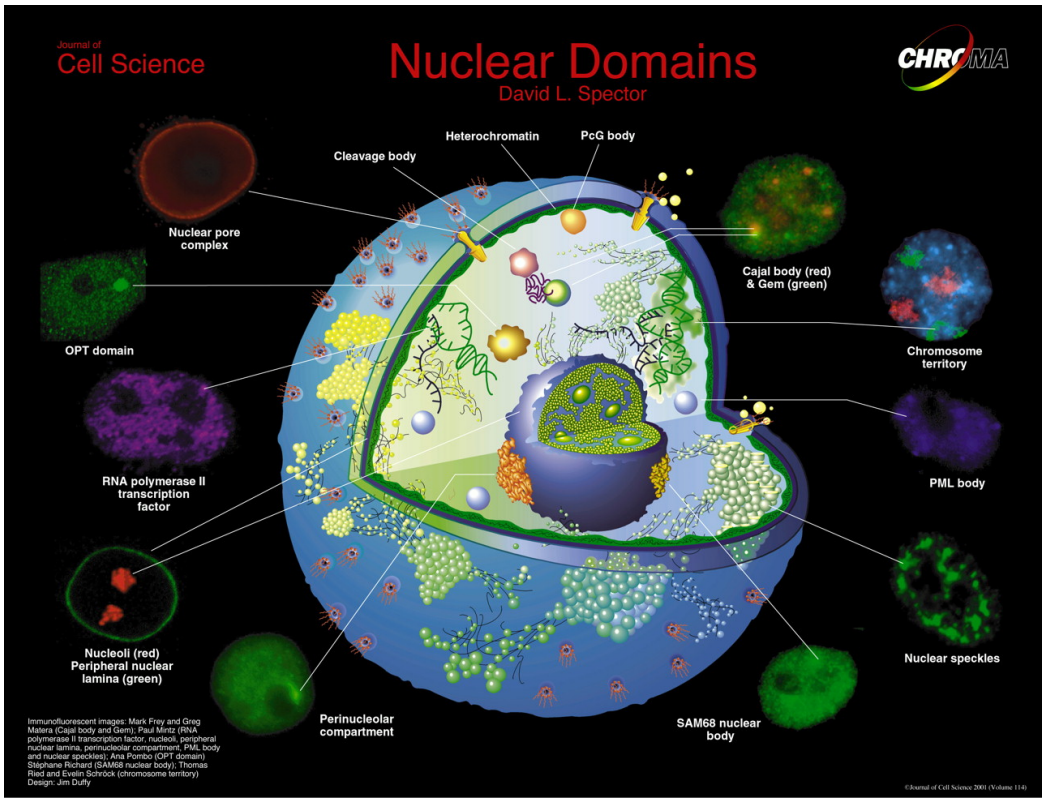

Figure 1.1: Overview of nuclear domains. This well-known poster visualisation of nuclear architecture summarizes some of the most promiment structures found in the nucleus which had been addressed by fluorescence microscopy at the time around 2001. This image has been both motivation and challenge to help extending the picture. From [166].

bodies.

Chromosome territories are the fraction of intranuclear space occupied by each chromosome during interphase, separated by a complex network of clefts called interchromatin domain. There are at least four different models for the spatial organization of chromosome territories, but they all have in common that actively transcribed genes reside on the periphery of chromosome territories and the nascent mRNA transcripts are extruded into the interchromatin domain for further processing ([6, 112, 113, 40, 26, 5]). There is evidence for a global scheme of chromatin organization such that actively transcribed genes become located in different regions of the nu-

cleus as opposed to inactive genes. This suggests the existence of a general mechanism for gene regulation based on nuclear organization over space and time. Some aspects of the chromosome domain model will be discussed in chapter 1.3.1.
The nucleus is thus a highly dynamic structure which responds to many metabolic requirements and undergoes dramatic reorganization throughout the cell cycle. Its overall organization is dominated by chromatin structure on the one hand side and by nuclear bodies and other substructures on the other hand. Many of its constituent proteins are organized in aggregates which are at equilibrium with a nucleoplasmic pool. The inherent structural and functional flexibility of the nucleus must be highly regulated, both spatially and temporally. In this work I study in detail two proteins which are crucial for the overall nuclear organization into chromatin and nuclear bodies. I use histone H1° as an example of a protein which stabilizes chromatin secondary structures and PML bodies (PML NBs) as examples of nuclear bodies. On this organizational level the dynamics of functional protein aggregates inside the nucleus can be studied in relation to the current cell cycle state. Histone H1° is studied quantitatively on the level of protein-DNA interaction and diffusional mobility of its nucleoplasmic pool.

1.2 Biology of Histone H1°

Linker histones comprise a functionally highly conserved protein family, which is found throughout all eukaryotes. In metazoans it is found in all tissues, though different variants of H1 histones are expressed in a tissue-specific manner ([33]). The relative composition of a cell's H1 complement varies not only with cell-type, but also with different states of differentiation during embryonic developement ([95]). Their overall protein structure is conserved in metazoans. The canonical H1 histone has a tripartite domain structure with a central globular domain which is flanked by

two smaller N- and C-terminal domains. The globular domain is highly conserved throughout evolution, while the tailing domains show specific variations in each H1 subtype.

1.2.1 Histones in chromatin structure

Chromatin has come a long way since its recognition as the material of genetic inheritance. It is nowadays viewed as a highly dynamic structure, with is both flexible and metabolically active. This flexibility is required for the adaptability of a cell responding to numerous external signals and environments (gene expression) as well as for its basal functionality during proliferation (DNA replication) and differentiation (gene regulation). It has been known for a long time that chromatin is an ordered structure at different organizational levels.
Nucleosomes are the basic units of chromatin organisation and are comprised of the core histones H2A, H2B and H3 and H4 which form the canonical octamers around which 146 bp of the DNA fiber are wound in 1.8 turns. The nucleosome spacing varies from 180 - 230 bp (in murine species [172]), see figure 1.2 (A, B). This chromatin fiber in turn occurs as a 10 nm fiber, a 30 nm fiber as well as other higher-order chromatin structures (figure 1.2 C). These structures are constantly being reorganized which allows chromatin to fulfill its various functions. Therefore nucleosome remodeling is essential to such processes as mitosis with a dramatic compaction and decondensation of chromatin. Likewise, all DNA-centered processes such as transcription, DNA repair, recombination and replication require at least to some degree also chromatin remodeling. Such remodeling processes involve (de-)stabilization of higher-order structures, nucleosome sliding, modulation of inter-nucleosome distance as well as regulation of the activity of nucleosome remodeling complexes. All of these processes having a large impact on transcriptional activity are strongly impacted by binding of histone H1. Its target is the DNA dyad on nucleosomes, where it resides bracing the two DNA strands emerging

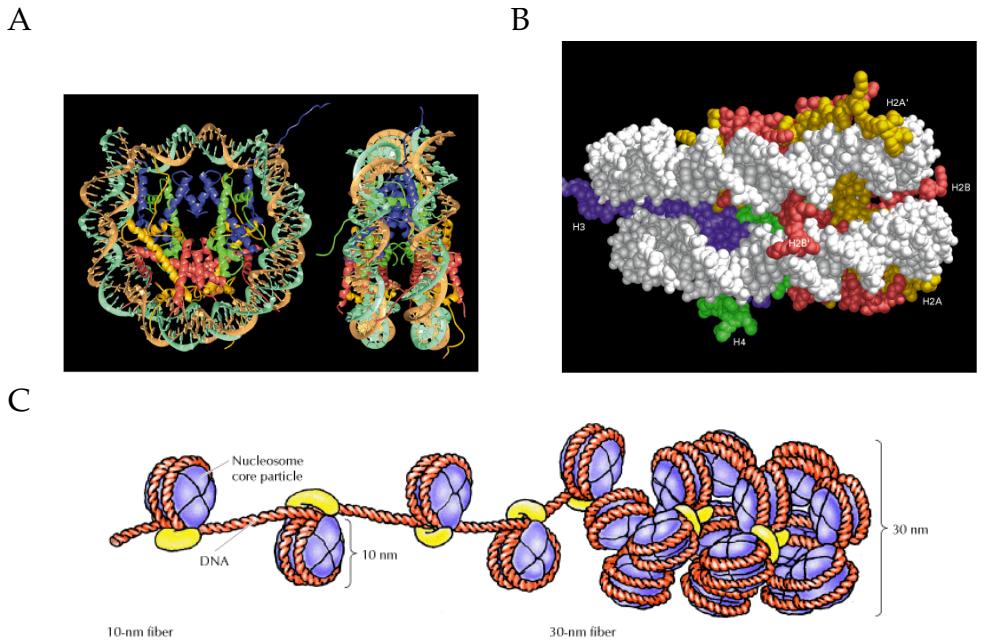

Figure 1.2: Structure of nucleosomes and the chromatin fiber. (A) Crystal structure of nucleosome octamer with DNA dyad (orange and light green) at 2.8 A resolution (ribbon model). (B) Space-filling model of nucleosome with the DNA shown in white. H2A is yellow, H2B is red, H3 is blue, H4 is green. Frontal and side view. From [108]. (C) Sketch of 30 nm chromatin fiber. The 10 nm fiber coils into a solenoid with 30 nm diameter. DNA is red, nucleosomes are blue, linker histone is yellow. From [43].

from the nucleosome. Upon binding H1 histone pushes chromsome structure into higher degrees of compaction (i.e. stabilizing the 30 nm fiber) and is observed in genome regions with a lower overall gene activity.
Considering the fact of histone H1 being involved so centrally in chromatin structure and dynamics it came in surprisingly that it is at least partially dispensable when the first viable H1-free organism was produced in Tetrahymena. Similar observations where made in other model organisms such as yeast and mice (reviewed in [94]). Usually downregulation of one or few H1 subtypes leads to upregulation of other subtypes with which the cell compensates. Mice lacking H1t (see chapter 1.2.2) are fully fertile, also knockout of H1° does not appear to have detrimental effects on mice. In the following I shall briefly review the different variants of histone H1 in order to outline the functional niche occupied by the subtype H1°.

1.2.2 Histone H1 variants - structure and function

Despite being functionally well conserved and ubiquitously found among eukaryotes, the H1 protein family is found in many isoforms. Most of these are differentially regulated depending on the proliferative potential of the respective cells or tissues. In mammals seven H1 subtypes are found (reviewed in [94, 27]), two of which are germ-line specific (CS H1 and H1t) and one is mostly developmentally controlled (H1°). Cleavage state H1 (CS H1) is upregulated in most vertebrate oocytes, while testis-specific H1t is preferentially expressed during spermatid maturation. H1° is upregulated at specific stages of embryonic development. For example, in *Xenopus* it is the most prominent histone during later stages of embryogenesis (after tail-bud-tadpole transition) which are marked by reduced proliferation and an extended duration of the cell cycle. Generally, H1° constitutes a considerable fraction of a cell's H1 complement in senescent cells or less proliferative tissues, such as liver, where it constitutes about 30 % of all H1 histones (Khochbin 2001). H1° shares this property with its (putative) functional and structural avian homolog H5. In spite of the

Figure 1.3: 3D Rendering of histone H1° globular domain. The globular domain of linker histones is known to confer DNA binding at the nucleosome dyad. Secondary structure predicted with SPDB viewer spdbv `http://spdbv.vital-it.ch/`. Protein backbone in gray, helices 1 and 2 in red and blue, respectively, short ß-sheet in green, N-terminus in yellow, C-terminus in brown. Rendered using SPDB viewer and POVRAY Povray `http://www.povray.org/` using a solution NMR structure from entry 1GHC.PDB at RCSB `http://www.rcsb.org/pdb/home/home.do`.

variety of H1 isoforms found throughout vegetal and animal kingdoms H1 histones seem to be functionally quite conserved as demonstrated by genetic experiments and most organisms deficient in one subtype are able to maintain a constant H1-to-nucleosome ratio. However, the subtle differences found are related to H1's binding affinity to chromatin, which leads to a differential stabilization of chromatin structure and epigenetic memory (see chapter 1.2.3). The relative composition of the H1 complement appears to be regulated on three levels (Khochbin 2001, Bustin 2005): There are cis-acting elements in the H1 one promotor which are sensitive to cell's proliferative potential. H1 mRNA stability is regulated by poly-adenylation. Finally, there is also translational control of H1 expression. In the context of this work it is important to mention that in contrast to previous beliefs H1 histones were shown to be quite mobile *in vivo* ([121, 28, 102, 103]). Instead of each individual H1 protein molecule resid-

ing on its respective binding site rather the overall equilibrium ratio of H1 to nucleosomes remains conserved. A secondary structure representation based on an 3D NMR solution structure is given in figure 1.3.
As described here H1 and its variant H1° take an important part in stabilizing chromatin secondary structure and to some extent in gene regulation. Many higher organisms possess a different regulatory level which is intricately interlinked with chromatin structure. This control scheme is subject of the next chapter.

1.2.3 Epigenetics

Large, complex genomes such as those found in metazoans and higher plants appear to require a form of gene regulation which persists throughout cell cycle. This is necessary to maintain differentiation states of cells in a multitude of tissues, some of which may require active proliferation while others show increased metabolic activity. There is an entire array of mechanisms conveying control over gene expression on the level of chromatin structure collectively known as epigenetics. This term underlines the important property of epigenetics to bypass control of gene regulation on the level of transcription. Molecular mechanisms of epigenetics involve alterations of chromatin structure, mostly chromatin compaction, as well as biochemical changes of both, histone complement and DNA. These biochemical modifications are seen as signals for transcriptionally active or silenced chromatin. On the level of DNA the most prominent observation is hypermethylation of Cytosine residues[1] to mark silenced genes. It is particularly frequent in pericentromeric chromosome regions which it stabilizes. Interestingly, DNA methylation appears to confer genomic imprinting as demonstrated with nuclear transplantation experiments ([162]). On the histone level there are a number of postranslational modifications leading to gene silencing: hypoacetylation of histones H3

[1] In mammals preferentially those cytosines are 5′-methylated which are part of CpG repeats amounting to about 2-3% of total cytosines found in their methylated form.

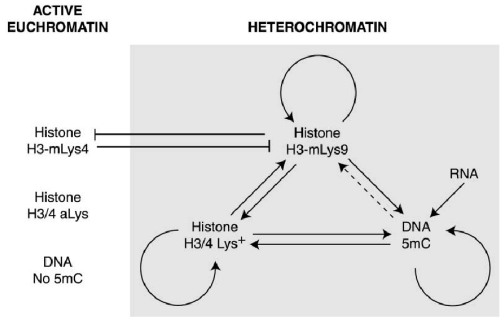

Figure 1.4: Epigenetic markers. Methylation of histone H3-Lys4, hyperacetylation of H3 and H4 and DNA hypermethylation of 5-Cytosine are signals for euchromatin (active genes). On the other hand methylation of H3-Lys9, hypoacetylation of histones H3/H4 and DNA hypomethylation are markers of heterochromatin (silenced genes). Arrows point out possible propagation of epigenetic markers which reinforce each other as well as themselves. The methylation signals H3-mLys4 and H3-mLys9 are antagonists. Adapted from [143].

and H4, methylation of residue Lys9 in H3. Conversely, methylation of Lys4-residue in H3 is characteristic of euchromatin. Figure 1.4 sums up the most important biochemical mechanisms. This, however, does not capture the full complexity of post-translational modifications, because the N-terminal tails of both H3 and H4 can be phosphorylated and acetylated next to methylation, for review see [143]. Not only post-translational modifications stabilize heterochromatin, but also binding of protein markers such as HP1 (heterochromatin protein 1) and its homologs (e.g. Swi6 in yeast). HP1 specifically recognizes H3-mLys9 to which it binds in heterochromatin regions. It serves to perpetuate and spread gene silencing signals. The temporal sequence of events in heterochromatin formation is thought to be: Histone H3 deacetylation, methylation of Lys9, HP1 binding and DNA cytosine-5-methylation (summed up in figure 1.5).

There is evidence that nucleation of heterochromatic foci is supported by dicer-dependent siRNAs. Once H3-Lys9 methylation has occured, the siRNA machenery may further stabilize heterochromatin and enhance its local spreading ([91, 131]). Since methylated DNA helps to recruit methyl-

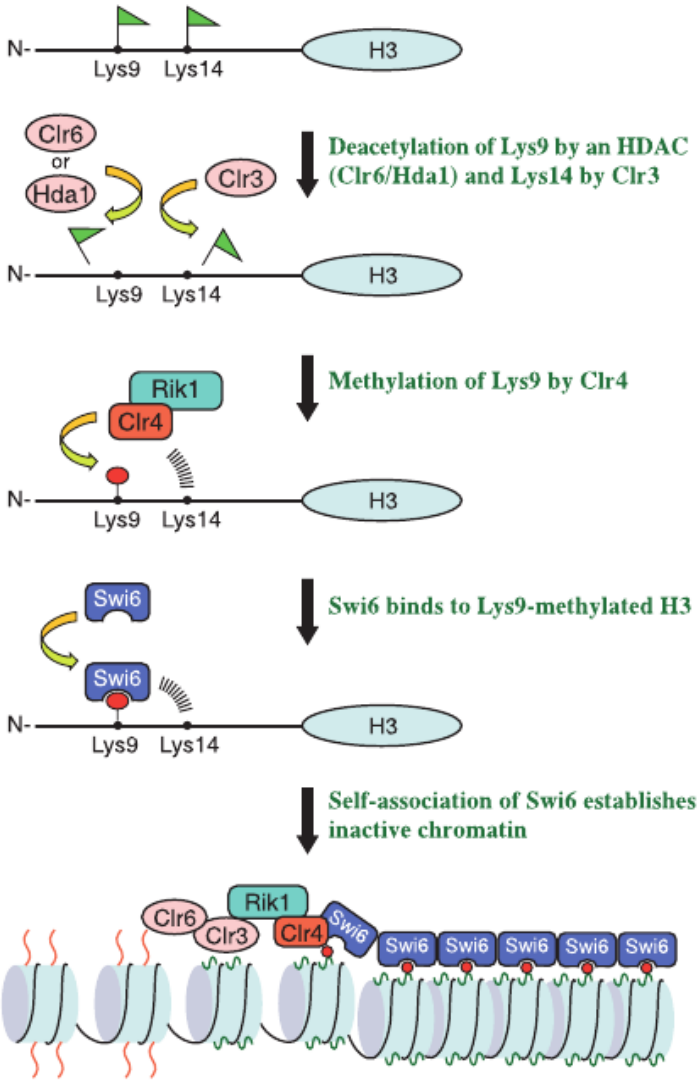

Figure 1.5: Steps of heterochromatin formation in fission yeast. The putative temporal sequence of events is histone H3 deacetylation (removal of green flags), methylation (addition of red lollipops) by the methyltransferase Clr4 (an SUV39H1 homolog), binding and self-association of Swi6, an HP1 homolog. Adapted from [129].

transferases, such as SUV39H1, via HP1 as well as the siRNA machinery heterochromatin formation appears to be a self-reinforcing and self-propagating process.
The linker histone H1 is related to epigenetic gene silencing by preserving the current state of epigenetic information. It does so by protecting certain genome regions from posttranslational modifications, s.a. hypermethylation [18], nucleosome acetylation [86], as well as from nucleosome remodeling by hSWI/SNF [87]. SWI/SNF is an ATP-dependent chromatin remodeling complex which facilitates the sliding of nucleosomes on DNA, a process which is believed to facilitate transcription in hypersensitive (i.e. transcriptionally active) genome regions. This shows that H1 has a somewhat ambiguous function in both inhibiting gene silencing (via methylation) as well as euchromatin formation (by inhibiting acetylation and chromatin remodeling).

1.2.4 Available mutants of histone H1°

To study quantitatively the binding behaviour of H1° several point mutations were introduced into the globular domain, where two putative binding sites are ([48, 28]). The mutations were chosen to be part of these putative binding sites (as for H25G, R74A, K97A) or basic residues nearby which are potential candidates for binding (R47A, K82V). Mutant K59A may lie on the non-binding half of H1° (judging from mapping it to the crystal structure of avian H5). One acidic residue was mutated to check if reducing acidity would enhance binding (E62H). All these mutants had been fused to GFP and tested semi-quantitatively using FRAP analysis ([28]) and were a generous gift by Tom Misteli.

1.3 Cell cycle

Proliferation is one of the basic functions of life enabling a species to propagate itself. On a cellular level proliferation requires sharing of cellular components, therefore cell growth, and of genetic material, therefore DNA replication, as well as their distribution to daughter cells. It was found ([126, 130, 96]) that these processes follow a strict temporal sequence, the cell cycle (illustrated in figure 1.6). One can distinguish at least four different stages, called G_1 phase, S phase, G_2 phase and M phase. The former three are part of interphase while the latter is equivalent to mitosis. The cell spends about 95 % of its time in interphase which is followed by mitosis.

1.3.1 Interphase

During interphase chromosomes are decondensed and distributed throughout the nucleus. Though decondensed, they appear to occupy a defined volume inside the nucleus, the chromosome territories ([45]) and their positions appear to be conserved ([67]). Interphase is the time during which DNA replication and cell growth occur thereby preparing the cell for division. Classically, three sub-stages could be identified:

- G_1 phase (or gap 1) corresponds to an interval between cytokinesis and the onset of DNA replication. This phase is characterized by metabolic activity and cell growth.
- During S phase (synthesis) DNA replication takes place, where the haploid genome is duplicated.
- G_2 phase (or gap 2) is marked by completion of cell growth as well as protein synthesis in preparation for mitosis

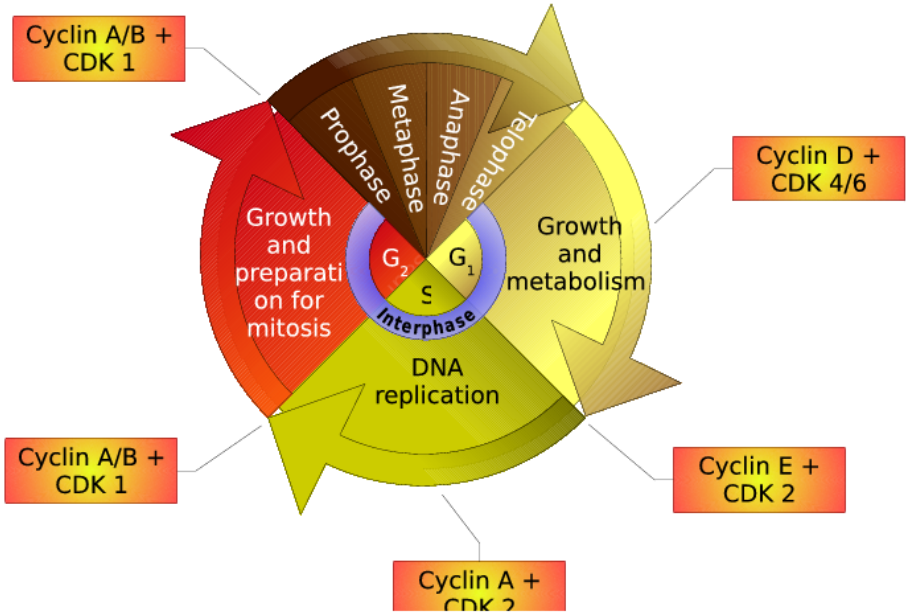

Figure 1.6: Eukaryotic cell cycle. Nuclear division (karyokinesis) and cell division (cytokinesis) occur during mitosis, while cell growth and DNA replication occur during interphase. Mitosis is classically divided into four phases, prophase, metaphase, anaphase and telophase. Interphase is characterized by DNA replication during S phase and two gap phases G_1 and G_2 in between. Cell cycle progression is regulated by the interplay of cyclically regulated genes, the cyclins and cyclin-dependent kinases (CDK's), which integrate intrinsic and extrinsic signals at specific check points to ensure successful cell proliferation.

Depending on the proliferation potential of certain tissues or organisms the length of the cell cycle phases may vary considerably. Cells in non-proliferative tissue, such as skin or nerve cells, as well as senescent cells may still be metabolically active, but do not undergo cell division. Such cells are known to occupy a quiescent stage, the G_0 phase.

Interchromatin domain

By the beginning of this work experimental evidence had mounted pointing towards the existence of defined volumes which are occupied by decondensed chromosomes during interphase, the chromosome territories. Though decondensed, those interphase chromosomes are thought to have a specific topology. The space not taken up by chromatin known as the interchromatin domain (ICD) is thought to be more accessible to proteins and nuclear bodies. This has led to the development of a putative topological model of gene regulation (figure 1.7, see also [29, 30, 42, 45, 183, 41, 184, 185]). In this view, several aspects of chromosome topology affect gene activity. Interphase chromosomes may exist in several states of condensation with loops or 100-kbp chromatin domains stretching out from the surface of the bulk chromosome (figure 1.7 a). The gene activity on these loops may change with their proximity to heterochromatin domains (figure 1.7 b). The overall density of interphase chromosomes seems to be spatially distinct with low density parts stretching into the ICD (figure 1.7 c). This overall chromosome structure appears to consist of ~1 Mbp chromosome domains with differential gene activity. The less gene-active (mid-to-late-replicating) domains tend to be located towards the nuclear interior as well as in close contact with the nuclear lamina (figure 1.7 d), while the more gene-active (early-replicating) domains are situated away from those loci. Genes on the surface of 1 Mbp domains appear to be more gene active than those located towards their interior (figure 1.7 e). This may be due to an increased availability of transcription factors, splicing factors, DNA repair machinery in pools within the ICD (figure 1.7 f). The

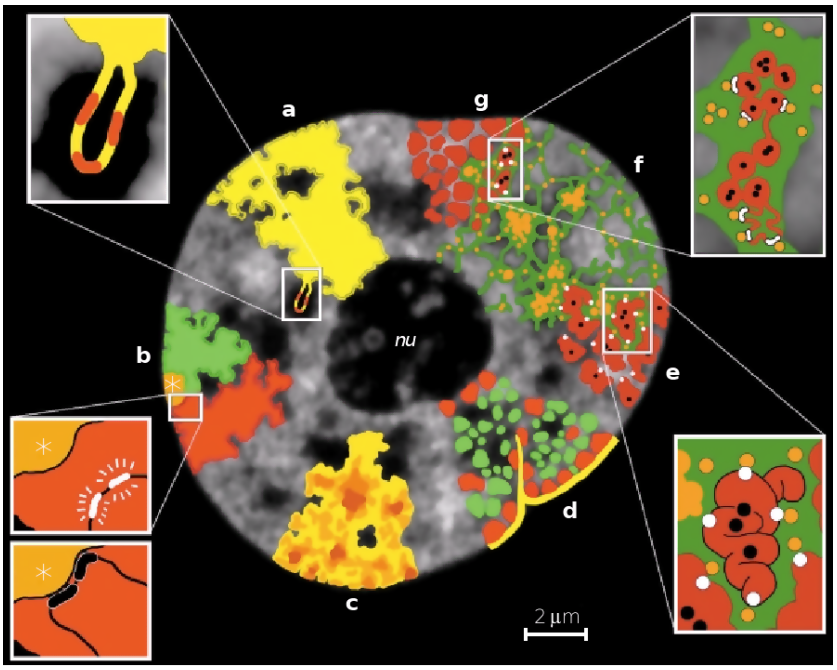

Figure 1.7: Model of functional chromatin architecture. A fluorescence micrograph of a HeLa cell nucleus with chromatin counterstain overlaid with a cartoon highlighting several aspects of topological gene regulation. In the middle a nucleolus is visible (nu). For details see text. Adapted from [45].

mechanism conveying gene activity is not clear, but several ideas exist, such as the decondensation of 1 Mbp domains into smaller loops stretching into the ICD (figure 1.7 f, inset bottom) or genes available to transcription factors on the surface of individual 1 Mbp domains (figure 1.7 f, inset top).

Part of the motivation behind this work is to study the influence of chromatin condensation and hence enlargement of the ICD during mitosis on PML nuclear bodies. Of particular interest is how chromatin domains or linkage to chromatin restrain the mobility of nuclear bodies.

1.3.2 Cell cycle regulation

The complex interplay of different stages during cell cycle and cell cycle progression are tightly regulated processes. The common principle is the existence of check points at the end of or during each phase which integrate extracellular and intracellular signals to ensure that the cell is ready to enter the next stage. For example before entering mitosis which involves chromosome segregation DNA replication must be completed, otherwise a catastrophic cell division would ensue where one of the daughter cells inherits an incomplete copy of the genome.
A highly conserved mechanism behind check point control is the interaction of two protein families known as cyclins and cyclin-dependent kinases (reviewed in [132, 130]) which form functional complexes. Cyclins are a class of proteins which exhibit a periodic synthesis and degradation. By means of this mechanism the availability of functional complexes is determined (reviewed in [96]). Cyclin-dependent kinases (CDK's) on the other hand phosphorylate downstream protein kinases or tumor suppressors which act as hubs integrating signals such as availability of nutrients, cell-cell contacts, growth factors. CDK's in turn are activated both by binding to specific cyclins and phosphorylation at conserved Tyrosine residues ([72]). A common example in eukaryotic cells is the *cdc2* gene (in vertebrates also known as *CDK1*) which interacts with class B cyclins to control the $G_2 - M$ transition ([79, 19]). This complex is also known as the maturation progression factor (MPF, figure 1.8, see also [133]).

The MPF also has roles in controlling chromosome condensation, nuclear envelope break-down (NEBD), fragmentation of Golgi and ER as well as spindle formation during mitosis. Another important checkpoint control is regulated by a related mechanism involving a complex between cyclin D and CDK 4 during G_1, where many environmental signals are integrated. During interphase the cell's constituent material is doubled and its metabolic activity is large. Distribution of cell material to its daughter cells occurs during mitosis which is subject of the subsequent chapter.

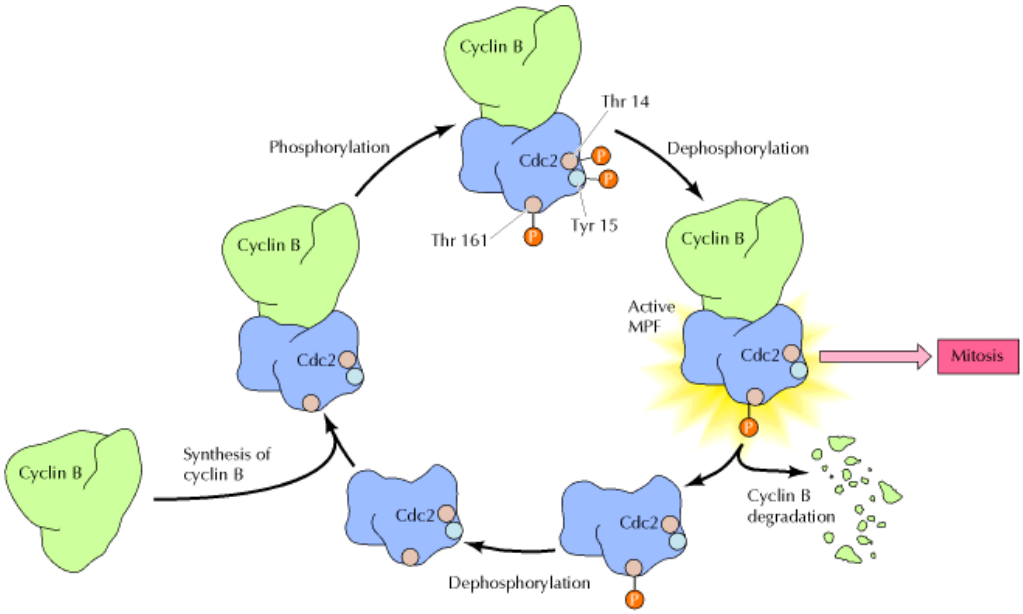

Figure 1.8: Cell cycle checkpoint control by the maturation progression factor (MPF). The active MPF is formed by a cyclin B member and a *cdc*2, a cyclin-dependent kinase (CDK). MPF activity is controlled by cyclin B synthesis and proteasomal degradation one the one hand and *cdc*2 phosphorylation on the other hand. The formation of a complex between cyclins and CDK's represents a common paradigm in cell cycle control. Figure adapted from .[43]

1.3.3 Mitosis

Of all the cell cycle phases the most staggering changes occur during mitosis. Both, the genetic material as well as all other cellular constituents are distributed between two daughter cells involving karyokinesis and cytokinesis. The gross morphological changes as well as chromatin condensation could be observed by early light microscopy.
[2]Therefore, classically, the sub-stages of mitosis are defined according to overall changes in cell morphology (compare figure 1.9). Mitosis is considered to begin at chromatin condensation (*prophase*). The condensed chromosomes rearrange and the nuclear envelope breaks down (NEBD). This stage is known as *prometaphase*. Chromosomes arrange to form a plane in the middle of the dividing cell with sister chromatids facing opposite poles of the mitotic spindle (*metaphase*), forming the so-called metaphase plate. Sister chromatids are pulled apart towards the poles (*anaphase*) and the daughter nuclei begin to reform (*telophase*). Finally, the cell is divided into daughter cells by a contractile ring in the same plane as the metaphase plate, the actual cell division (*cytokinesis*).
This common classification scheme for the stages of mitosis is challenged by the fact that the temporal sequence of events during mitosis are not conserved among all eukaryotes. For example chromatin condensation is not visible in many fungi, such as yeast, or NEBD occurs at a later stage in nematodes (**[116, 63]**). Moreover, the formation of a metaphase plate is not universal either. Therefore, a classification scheme based on molecular events has been proposed in order to achieve an unambiguous staging ([136]). Here the progression through mitosis is interpreted in terms of transitions each of which is characterized specifically by the activity of cell cycle regulators (figure 1.9 B). Checkpoints between transitions are characterized by the onset of activity of a different set of cell cycle regulators. Transition 1 constitutes a series of molecular events which reversibly prepare the cell for mitosis, most markedly the beginning of

[2]Chromosomes are named according to their property of being stainable entities (Greek: $\chi\rho\omega\mu\alpha$ = colour, $\sigma\omega\mu\alpha$= body).

chromosome condensation. The central regulator during transition 1 is the *cyclin A-CDK* complex, as well as *Plk1* (polo-like kinase) preparing the centromers and *cdc25* which in turn activates the MPF (cyclinB-CDK1). The equilibrium of *cyclinB-CDK1* nucleo-cytoplasmic shuttling is shifted from predominantly cytosolic to nuclear upon N-terminal phosphorylation. This onset of nuclear *cyclinB-CDK1* activity marks the point-of-no-return which irreversibly commits the cell to mitosis ([144]). The next stage,termed transition 3 is characterized by the activity of both cyclin B as well as the anaphase-promoting complex (*APC*) in conjunction with the kinase *cdc20*. The APC latter is a ubiquitin ligase which targets proteins (s.a. *securin*) necessary for dis-joining of chromosomes for proteasomal degradation, thus promoting the escape from mitosis. Transition 3 can be identified with prometaphase. Full APC activity is reached only after kinetochore attachment marking transition 4, which comprises metaphase and most of anaphase until cytokinesis. *APC-cdc20* activity leads to a decrease in active cyclinB-CDK1, thus allowing the reformation of a nuclear envelope. In the final stage, transition 5, *Cdc20* is replaced by *Cdh1* facilitating *APC-Cdh1* mediated proteolysis which leads to escape from mitosis and a suppression of mitotic events during interphase.
In summary, a molecular staging scheme for mitosis has been suggested which aims to reduce ambiguities of the existing morphological classification scheme.

1.4 Biology of PML nuclear bodies

PML nuclear bodies (PML NBs, a.k.a. nuclear domain 10, ND10, or PML onkogenic domains, PODs) are termed after their main constituent, PML protein, whose corresponding gene is disrupted in acute promyelotic leukemia (APL) due to a chromosomal translocation t(15:17) ([152, 171]). The disruption of the PML gene prevents the formation of PML NBs. Due to

A

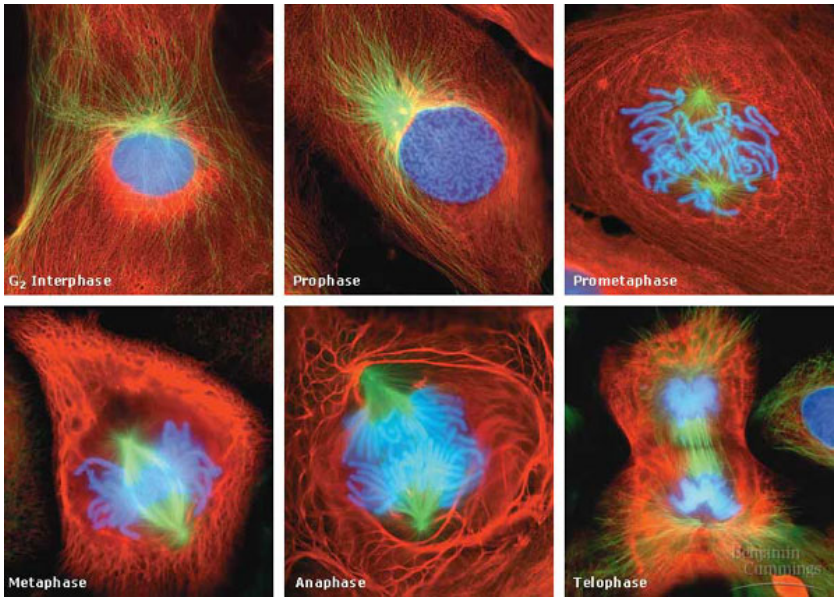

B

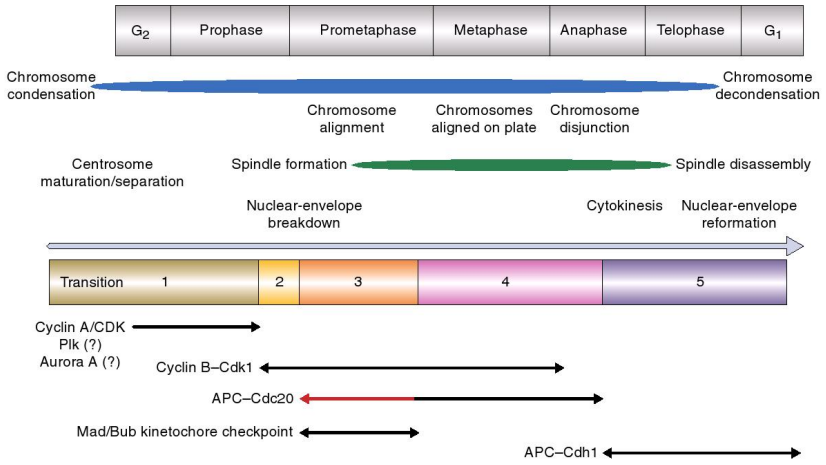

Figure 1.9: (A) Morphological stages of mitosis. Fluorescence micrographs of Newt lung cells highlighting the morphological stages of mitosis showing chromatin (blue), microtubules (green) and keratin (red). The image was originally produced by C. L. Rieder (New York State University, Wadsworth Center) and published in [127]). (B) Molecular classification scheme for the stages of mitosis. Activity of several cell cycle regulators allows the subdivision of mitosis into sub-stages which are compared to the temporal sequence of morphological changes classically identified with mitotic progression. Adapted from [136].

the dominant negative action of the gene fusion to retinoic acid receptor α PML protein can not act as a tumor suppressor. Therefore it is found in many cancers ([78, 153]).

1.4.1 PML NB structure and function

PML NBs are multi-protein complexes with an average diameter around 0.5 μm. Depending on cell type and the current stage of cell cycle varying numbers are found ranging from 30 in G_2 phase to zero during mitosis. PML NBs are believed to act as storage domains for proteins involved in DNA repair, RNA processing, regulation of transcription as well as antiviral defense and apoptosis ([39, 198, 46, 141, 59, 153]). The remarkable dynamics of PML NBs with regard to their number is caused by their tendency to fuse and form mitotic accumulations of PML protein, *MAPPs* ([47]), which eventually dissolve. Thus, there must be a mechanism which regulates PML NB formation as well as recruitment of their constituent proteins. It has been suggested, that this regulation is mediated by post-translational modification with the small ubiquitin-like polypeptide *SUMO-1* ([170, 92, 93, 124, 50]). According to this model PML protein forms a frame work cross-linked by SUMOylation and SUMO-binding sites (figure 1.10). Phosphorylation of PML protein has been implicated in disruption of PML NBs during prometaphase ([60]). PML NBs make multiple contacts to the surrounding chromatin ([24]) and respond to multiple environmental stresses with morphological changes ([60, 47, 22]).

1.4.2 Dynamics of PML nuclear bodies during mitosis

As mentioned previously (chapter 1.4.1), PML NBs dissolve during mitosis and reform afterward. As the cell progresses from G_1 to G_2 phase the number of PML NBs increases during a series of splitting and merging

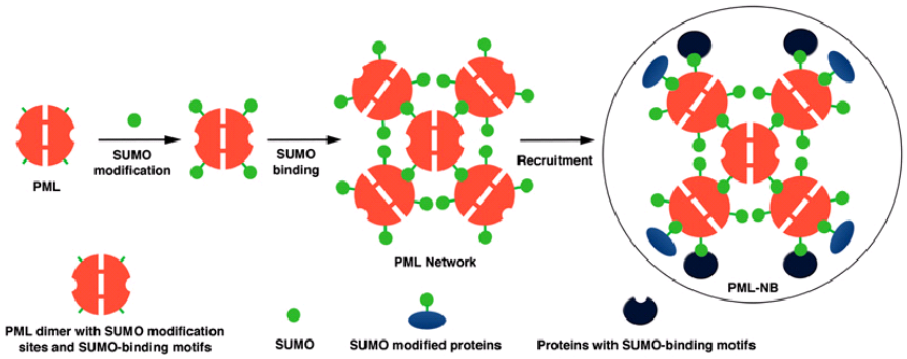

Figure 1.10: Model for PML NB formation. PML protein with two SUMOylation sites and one SUMO-binding motif dimerizes. The SUMOylated dimers form a scaffold which in turn recruits further SUMOylated proteins and proteins with SUMO-binding motifs. Up to 100 different protein constituents have been found in PML NBs. Adapted from [115].

events. PML NB number decreases dramatically during mitosis ([173, 98, 177]). PML NB disruption during mitosis is thought to be caused by de-SUMOylation ([60, 160]) and phosphorylation ([60, 170]). The process of PML NB disruption goes along with the accumulation of PML protein in MAPPs and the appearance of a mitotic isoform of PML protein. MAPPs are thought to be reservoirs for PML protein during mitosis through which the latter is passed on to the emerging daughter cells ([47]). They persist in the cytoplasm after mitosis well past G_1 phase. It has also been reported that PML NBs make close contact with surrounding chromatin which is thought to stabilize PML NBs ([57, 58]). In part, this chromatin attachment may be responsible for their relative immobility during interphase ([125, 70]). The loss of chromatin contacts during mitosis, concomitant increase of dynamics and formation of MAPPs are subject of this work.

1.5 Quantitative live cell imaging

The understanding of basic processes in cell biology heavily relies on quantitative information on the single cell level. However, the sensitivity of

established high-throughput techniques in genomics and proteomics is not yet sufficient to provide quantitative data on single cells ([179, 178]). Therefore, cell biological research utilizes fluorescence microscopy. Time-resolved information is only obtained with time-lapse microscopy, usually in conjunction with fluorescent protein (FP) technology. Traditionally, microscopic images have been interpreted mostly qualitatively to obtain an understanding of the morphology and topology of sub-cellular structures. This paradigm is shifting towards gaining quantitative knowledge about the mobility of proteins, sub-cellular protein complexes, chromosomes and sub-cellular compartments in a spatially and temporally resolved manner ([195]). A number of fluorescence-based techniques have been developed to this end, such as fluorescence recovery after photobleaching / activation (FRAP), fluorescence correlation spectroscopy (FCS), continuous photobleaching or fluorescence resonance energy transfer (FRET) (for review see, [106, 15, 81, 137]). More recently, single particle tracking has become a valuable tool to extract quantitative information on the mobility of sub-cellular complexes from time-lapse microscopy ([14, 53, 34]).

1.5.1 Fluorescence recovery after photobleaching (FRAP)

Originally developed by Axelrod et al. ([10, 99, 11]) in 1976 to study lateral diffusion in biological membranes FRAP has seen a renaissance during the last two decades (for review see [97]). With the wide-spread availability of commercial confocal laser scanning microscopes in conjunction with fluorescent protein technology FRAP has become a commonly-used tool to study the mobility of protein populations (for review see [106, 164, 107, 120, 142]). The method relies on the application of a short laser pulse to deplete the fluorescence signal locally, either in one spot or in a geometrically defined area. Immediately after this bleaching laser pulse an image series is recorded. Mobile molecules diffuse out of the bleached area into the surroundings and from there into the bleached region. Thereby the signal intensity in the bleached area is restored over

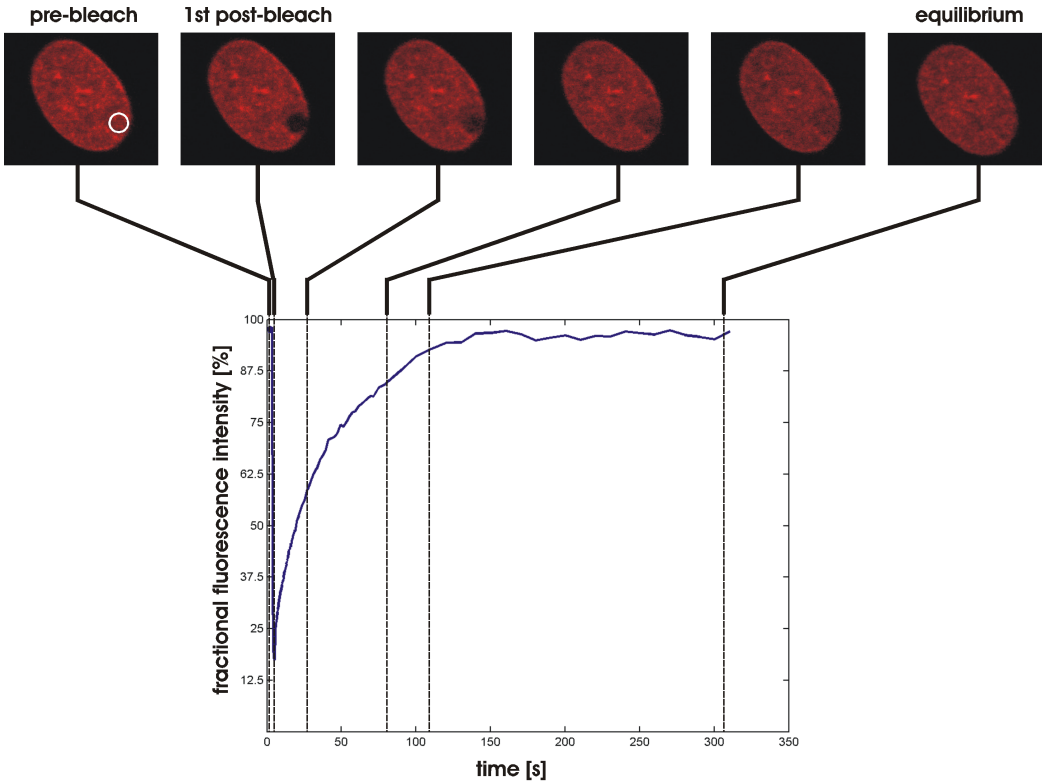

Figure 1.11: Principle of fluorescence recovery after photobleaching (FRAP). A short high-intensity laser pulse is applied to a defined region (white circle) to abolish fluorescence locally. Diffusive molecules restore the fluorescence over time. This process is recorded as a time series. Mean fractional fluorescence in the bleached region is plotted over time indicating the restoration of the perturbed system to its equilibrium.

time. The kinetics of this process gives insight into the mobility of the molecule under study as well as the mobile fraction (see figure 1.11).

The overall rate of the fluorescence recovery is governed by a number of factors, such as molecule size, viscosity of the surrounding compartment as well as binding to other cellular components. The latter slows down the rate of the recovery, which in turn can be used to quantify biochemical interactions. In the following paragraph I will outline strategies for quantitative interpretation of FRAP data by using numerical models.

1.5.2 Modeling and simulation of FRAP

Biology is dynamic. On a molecular scale this means that all molecular constituents of a cell are in constant motion. Generally, this fact is underappreciated, because *in vivo* fluorescence microscopy usually yields a snapshot of the spatial distribution of a molecule at equilibrium. As introduced above, FRAP has been designed to visualize the inherent mobility of biological molecules. In spite of its relatively simple implementation on contemporary confocal microscopes the quantitative analysis of FRAP for the most part is limited to determining the half-time of the recovery, i.e. the time until half of the initial intensity in the bleached region has been reached. While this number allows in principle the comparison of several molecules with different mobility or probing relative viscosities, it is otherwise not a very useful quantity. The half-time of the recovery is not a material constant, but is rather very specific to the experimental conditions used, such as bleaching geometry and to a lesser degree the bleaching time and recording speed. In order to obtain more generalizable parameters one has to consider the physical origin of particle movement and velocity, such as Brownian motion, directed motion (or active transport) and binding interactions. Directed motion is not the focus of this work. In the following Brownian motion and binding interactions (i.e. biochemical reactions) shall be discussed in more detail.

Modeling Brownian motion[3]

In gases or liquids small particles are subject to thermal motion, where their kinetic energy in each direction of space is

$$E_{kin} = \frac{1}{2}mv_x^2 = \frac{1}{2}kT$$

[3]Brownian motion is the term for thermal motion on a molecular scale. In ensembles of molcules such as found in solutions the term Brownian motion is often used synonymously with diffusion.

where m denotes the particle mass, v_x.. velocity along one spatial coordinate, T .. absolute temperature and $k = 1.380650310 - 23 \cdot m^2 \cdot kg \cdot s^{-2} K^{-1}$.. the Boltzmann constant. This leads to a microscopic description of Brownian motion, by which particle trajectories are understood as random walks. That view will be further discussed in the methodological section on particle tracking (see chapters 3.2.6, 3.2.7).
Since confocal imaging allows the observation of ensembles rather than single molecules, another quantitative description is more useful for the discussion of Brownian motion in a FRAP experiment. This macroscopic description was derived by the physiologist Adolf Fick in 1855 and named in his honor Fick's laws. The idea is that a material flux J_x along a spatial coordinate x is proportional to the concentration gradient along that coordinate, hence

$$J_x = -D \cdot \frac{\partial c}{\partial x}$$

with D the diffusion constant as the factor of proportionality. This is known as Fick's first law. In a closed system mass conservation requires that the flux destroys or changes the gradient over time. This is expressed in Fick's second law as the rate with which the concentration changes, which turns out to be proportional to its curvature:

$$\frac{\partial c}{\partial t} = D \cdot \frac{\partial J_x}{\partial x} = D \cdot \frac{\partial^2 c}{\partial x^2}$$

This differential equation can also be generalized to the 3-dimensional case with x being a universal spatial coordinate:

$$\frac{\partial c\left(\vec{x}, t\right)}{\partial t} = \nabla \cdot \left(D \cdot \nabla \cdot c\left(\vec{x}, t\right)\right)$$

The diffusion coefficient D can either be interpreted as spatially uniform or as non-uniform. In the latter case diffusion is anisotropic in all directions of space and D becomes a tensor, while in the former D is scalar and

diffusion is isotropic, in which case the equation simplifies to:

$$\frac{\partial c\left(\vec{x},t\right)}{\partial t} = D \times \triangle c\left(\vec{x},t\right)$$

In both cases this partial differential equation is non-trivial to solve. Many publications have therefore used assumptions or simplified geometries in order to obtain an analytical solution. For example, the original Axelrod publication [10] made the assumption of a rotationally symmetric Gaussian bleach profile and disregarded non-lateral (i.e. 3D) diffusion. In this case an isotropic diffusion coefficient can be directly obtained from the recovery half-time according to

$$D = \frac{\omega^2}{4 \cdot t_{1/2}}$$

where ω.. radius of bleach spot. This expression was later adopted and modified by other authors, for example to extend it to 3D diffusion ([165, 135, 25]). For review see [37, 36]. To simplify the mathematical treatment many studies assumed an infinite domain for the diffusion to eliminate the need for a boundary condition. However, in practical terms this condition is usually violated, because the diameter of the bleach spot can hardly become smaller than 1 μm while the diameter of the nucleus is around 10-20 μm. A few studies already took the real geometry of the nucleus or cellular compartment into account ([161, 157]).

Another complication is that the distribution of the protein under study may be inhomogenous. In this case one can not easily distinguish between spatial intensity differences based due bleaching or due to the intrinsic protein distribution. To account for this [161] have suggested to divide all post-bleach images by the pre-bleach image which represents the equilibrium distribution. In this way the spatial intensity is now only determined by the concentration gradient from bleaching and diffusion.

Most studies also disregard the three-dimensional nature of diffusion in cells or cellular compartments. This is mainly due to a lack in imaging

instrumentation which allows the acquisition of time series in 3D with sufficient speed. Moreover, since both confocal as well as wide-field microscopes acquire optical sections sequentially, there is always a time delay between sections during which diffusion may occur. Additionally, the computational complexity increases considerably with increasing dimensionality. Therefore, data acquisition and modeling in true 3D + time in live cells was not feasible for this study. However, it was shown by [20] that when using objectives with lower numerical aperture and non-confocal conditions, 3D diffusion inside the nucleus can be approximated with a 2D model. The deviation found in that study was around 14%.

Modeling reaction-diffusion systems

Diffusion or Brownian motion is not the only force which drives particle mobility in living cells. In contrast, another determining factor of the bulk diffusivity are reactions with potential binding partners. From chemical kinetics follows that binding can be modeled using differential equations. A simple example could be formulated like

$$A + B \rightleftharpoons C$$

with A.. freely diffusing and labelled reactant, B.. binding site (mobile or immobile) and C.. bound complex. The corresponding differential equations describing the time dependence of the reaction are:

$$\frac{\partial [A]}{\partial t} = k_{off} \cdot [C] - k_{on} \cdot [A] [B]$$

$$\frac{\partial [B]}{\partial t} = k_{off} \cdot [C] - k_{on} \cdot [A] [B]$$

$$\frac{\partial [C]}{\partial t} = k_{on} \cdot [A] [B] - k_{off} \cdot [C]$$

with k_{on}.. rate of the association reaction and k_{off}.. rate of the dissociation reaction. In cases where diffusion is much faster than reaction rates one can approximate the scenario as being reaction-controlled and disregard the diffusive component. Such a scenario was found by [139] where constituent proteins of nuclear pore complexes were labelled and their binding was analysed using FRAP. They established that dissociation rates in the range of $\left[10^{-6}..10^{-1}\right]\ s$ can be adressed by FRAP analysis. Lower rates would take too long to be adressed by live cell imaging and faster rates would violoate the assumption of a purely reaction-controlled situation. If the process is truly reaction-limited and diffusion can be neglegted, then the time constant of the recovery directly represents the inverse of k_{off}.
However, this can not be generalized. Many studies in fact completely neglect diffusion ([121, 135],[49, 102, 103, 28]), often by stating that a long recovery half-time (compared to free diffusion) can not be influenced by diffusion. This assumption is often wrong, as shown by [169, 20] using numerical simulations of reaction diffusion systems and FRAP data. It was estimated by [169] that about two thirds of all FRAP analyses may monitor a process which is governed both by diffusion and by biochemical reactions. Neglecting the diffusive component may lead to an error in the estimated parameters in the range of two orders of magnitude [168]. Assuming that the binding sites B are immobile one can derive a 2D reaction-diffusion model for the reaction mentioned above as

$$\frac{\partial [A]}{\partial t} = D \times \left(\frac{\partial^2 c}{\partial x^2} + \frac{\partial^2 c}{\partial y^2} \right) + k_{off} \cdot [C] - k_{on} \cdot [A]\,[B]$$

$$\frac{\partial [B]}{\partial t} = 0$$

$$\frac{\partial [C]}{\partial t} = k_{on} \cdot [A]\,[B] - k_{off} \cdot [C]$$

Since B is immobile and *bona fide* not destroyed or altered by the bleaching process it does not change over time. The bound complex C must therefore

also be immobile and thus the diffusive term does not appear in the last equation. The model and the assumptions made here are well suited to modeling of the H1° diffusion and binding to chromatin used in this work.

1.5.3 Fluorescence correlation spectroscopy (FCS)

Fluorescence correlation spectroscopy was developed in 1972 by Madge, Elson and Webb and was further developed by Rigler ([111, 146, 52, 145]) to study molecular mobility and interactions. It relies on illuminating a diffraction-limited spot to excite fluorescent molecules using laser illumination and a high numerical aperture lens. Single mobile molecules in the femto-liter (fL) observation volume (figure 1.12 A) give rise to fluctuations in the detectable fluorescence intensity which is recorded over time (figure 1.12 B). The resulting intensity trace has inherent information on periodic processes such as motion through the observation volume or dark states. This information can be extracted by a mathematical transformation known as an autocorrelation (figure 1.12 C, D). The main readouts are the diffusion time (inversely proportional to the diffusion coefficient) and the particle number (proportional to the concentration). This allows quantitation of molecular weight or viscosity, concentration, binding equilibiria and dark states ([56, 82, 65, 187, 191]). More recently, the study of the mobility type such as anomalous diffusion has moved into the focus of research ([192, 186]). Molecular interactions can be directly analysed by labeling putative interaction partners with spectrally separable fluorescence dyes and performing a crosscorrelation analysis (figure 1.12 E). This allows a direct quantitation of bound fractions *in vitro* and *in vivo* (figure 1.12 F). FCS was used in this work to obtain an estimate of the diffusion coefficient of histone H1°-GFP.

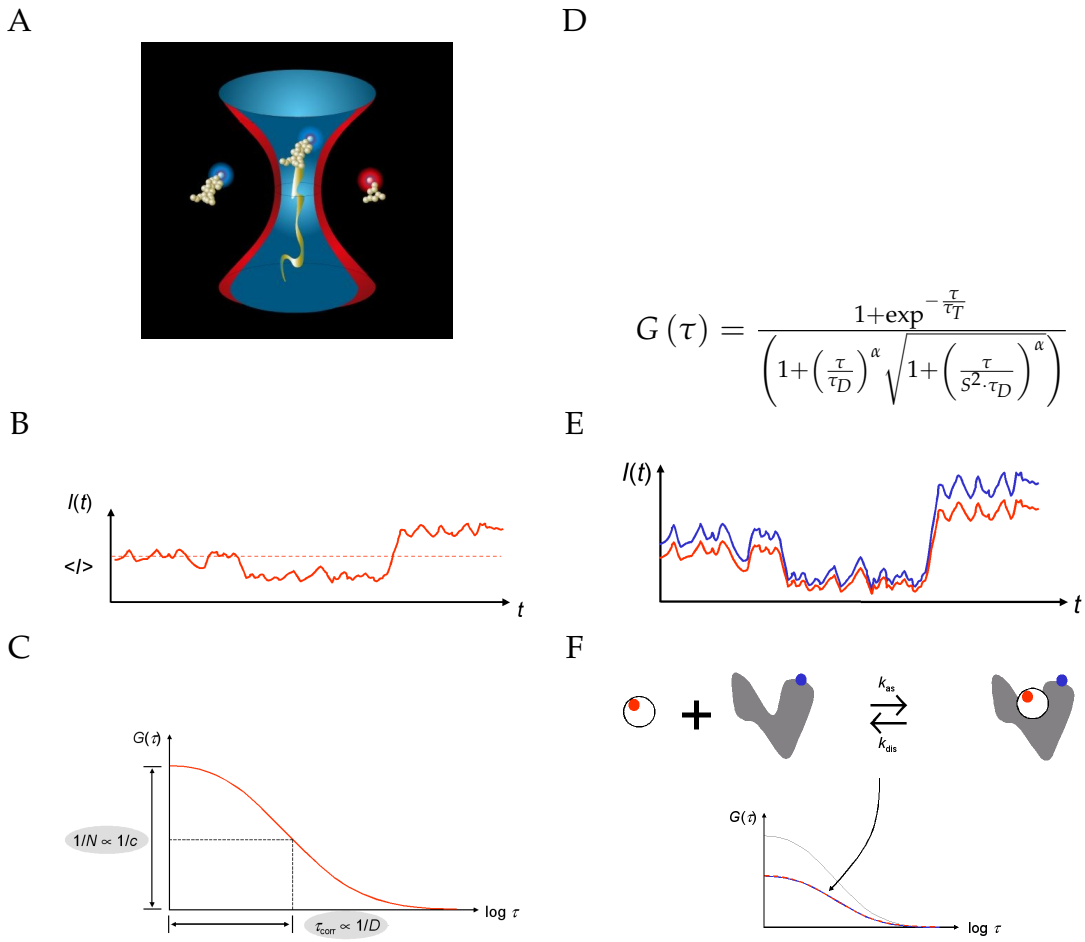

Figure 1.12: Principle of fluorescence correlation spectroscopy. (A) Diffraction limited observation volume showing overlap of two spectrally distinct fluorophores with a random trajectory. (B) Intensity trace shows random fluctuations over time (solid line) and mean intensity (dashed line). (C) Autocorrelation yields diffusion time at half-maximal decay and number of 1/(particle number) as amplitude. (D) Autocorrelation function with terms for dark states (τ_T), 2D and 3D diffusion (τ_D) and anomalous diffusion (α). (E) Fluorescence cross-correlation (FCCS). Two intensity traces of bound interaction partners show simultaneous fluctuations. (F) Bound fraction of equilibrium reactions can be probed using FCCS.

1.5.4 Single particle tracking

The biophysical techniques presented above, FCS and FRAP, are applicable to single molecules and protein populations, respectively. In cell biology single particle tracking can be applied in cases where protein clusters or cell organelles become large enough to be distinguishable by fluorescence microscopy. In such cases quantitative information on particles can be extracted. Single particle tracking is a branch of the field of motion analysis where image sequences are analyzed to obtain time-resolved, quantitative information about movement. Common to all motion analysis approaches is that a parametrized physical model is used describing the underlying motion. This makes motion analysis a parameter estimation problem of such parameters as velocity, acceleration, diffusion coefficient or the coefficient of anomalous diffusion. Widespread strategies to obtain motion information are approaches based on the optical flow or particle tracking velocimetry. In optical flow techniques the apparent motion of objects, surfaces or edges is analyzed relative to a fixed reference position, i.e. the observer. One can distinguish at least four classes of optical flow techniques:

- *Gradient-based* methods use first or second order derivatives of image intensities in both space and time domains ([88, 128, 1])
- *Region-based* matching is an alternative method in cases where the spatio-temporal resolution of the data set is inappropriate for the computation of gradients. It relies on interpreting a shift which maps images at consecutive time steps on one another as velocity ([7]).
- *Frequency-based* methods use velocity-tuned filters to identify velocity components in Fourier space ([3, 83, 61]).
- A related class of techniques are *phase-based* methods which compute the phase correlation between images as the Fourier inverse of the cross-power spectrum to obtain the translative moment between consecutive images ([62, 69]).

The technique used in this work was particle tracking velocimetry (PTV) as implemented in the image processing software TIKAL ([14, 12]). In the PTV approach individual object properties such as velocity, acceleration and volume are determined. This is combined with heuristics using physical object properties such as inertia to establish the correct connectivities in the trajectory network ([109, 110, 180, 134]).
No matter which approach has been applied the result of particle tracking is a network of their trajectories, in other words the paths which the particles have taken. If several particles are tracked simultaneously their respective trajectories form a network. This network of trajectories is usually represented as a matrix where each entry represents the position of one particle at a given time. The trajectories are then used in consecutive steps to extract velocities, diffusion coefficients and the coefficient of anomalous diffusion as presented in this work. Furthermore, the trajectories can also be employed to relate particle positions to other structures in the images, such as chromatin imaged in a spectrally distinct channel. For the PTV approach to work the gray value images must be segmented into binary images to extract trackable objects. Furthermore, any underlying movement in the instrumentation or sample under study can interfere with the motion analysis, so a previous image registration step is necessary. Both, image segmentation as well as registration are subject of chapters 1.5.6, 3.2.2 and 3.2.3.

1.5.5 Automated analysis of tracking data

Single particle tracking is often used to probe the microscopic environment of a molecule or molecular assembly. One can assess the viscosity or permeability of the medium or, conversely, the molecular size of the particle of interest. Moreover, the study of visco-elastic properties often found in saturated protein solutions as well as in living cells has become the focus of intense research ([154, 155, 192, 56]). These properties which can be described in analogy to polymer solutions lead to the phenomenon of

anomalous diffusion, in which a fractional time-dependence of the mean square displacement is found. All tracking data on a microscopic scale is intrinsically noisy, because the process under study, Brownian motion ([31, 55, 163]), gives rise to random walks. In order to achieve meaningful results large numbers of particles need to be tracked. Thus, not only an automated single particle tracking scheme is needed (as described in chapter 1.5.4), but also an automation of subsequent analysis. Any heterogeneities in the medium or changes in its permeability would give rise to changes in particle dynamics.
One very important aspect of the nuclear environment in this work is the change in diffusive mobility, namely, the diffusion coefficient of PML NBs. These changes can be quantitatively predicted by a likelihood-based statistical approach presented by Montiel et al. ([123, 189]). This approach obliterates the laborious and potentially biased visual inspection which would otherwise be necessary and facilitates the upscaling of data analysis to hundreds or thousands of trajectories (compare figure 1.13).

1.5.6 Image processing

The goal of image processing at large is to alter the properties of an image to enhance certain properties. In my case the goals are contrast enhancement, noise reduction, segmentation and registration. In the following the image processing steps used in this work will be explained.

Contrast enhancement

Contrast is the property of images which makes objects distinguishable from the rest (background) of the image. It can be defined according to Michelson ([119]) as

$$\frac{I_{max} - I_{min}}{I_{max} + I_{min}}$$

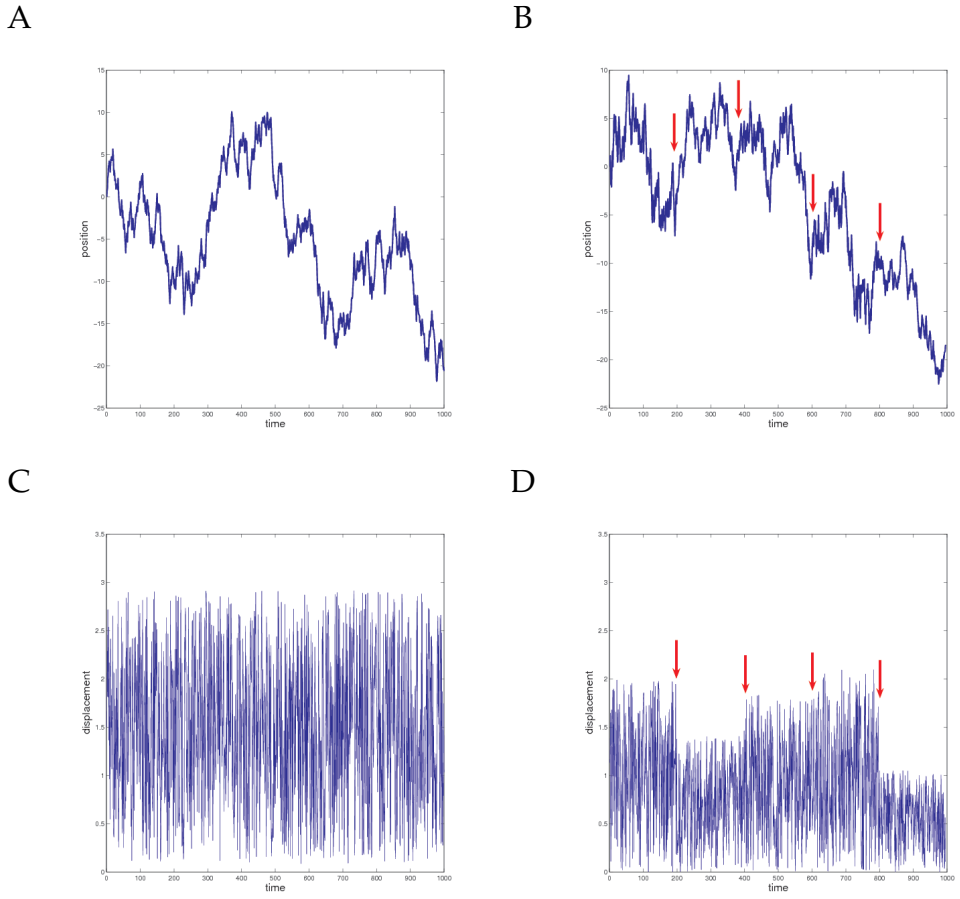

Figure 1.13: Changes in diffusive dynamics applied to simulated 1D-random walks over 1000 time steps. Random walk with constant diffusion coefficient (A) and corresponding displacement (C). Random walk where diffusion coefficient changes every 200 time steps (B, red arrows). Displacement of (B) reveals the underlying changes in diffusive dynamics (D, red arrows). These changes can be quantitatively predicted by a likelihood-based analysis scheme. Some of these changes are difficult to detect visually due to the random nature of the data.

where I_{max} is the maximum intensity and I_{min} the minimum intensity in the image. A high contrast facilitates object recognition and makes, e.g. gradients larger. Since derivatives are used in some of the following image processing steps below contrast is an important image property. To enhance image contrast both I_{min} and I_{max} can be decreased or increased, respectively.

- Background subtraction: Microscopic images tend to have a background intensity $I_{min} > 0$ due to detector dark noise as well as residual fluorescence (s.a. from unspecific staining or the distribution of fluorescence proteins). Usually, the mean or the minimum value of a defined background region is subtracted pixel-wise from the entire image. The background can be defined by the user or by means of an intensity histogram. To correct for non-uniform illumination the background can be defined using morphological filters. In this work a user-defined region was used to determine background, since non-uniform illumination usually does not affect typical fluorescence microscopy images very much.
- Normalization increases I_{max} after background subtraction by multiplying each pixel by $2^{depth} / I_{max}$where $depth$ is the color depth of the image.

An example of a microscopic image before and after contrast enhancement is given in figure 3.4. Other than this simple global contrast enhancement there are a number of adaptive and local contrast enhancement methods which are not described here.

Noise reduction

Microscopic images contain noise which is noticeable as “shot noise” or “speckle noise”. The largest contribution of noise stems from the photodetectors, such as photomultiplier tubes (PMT) in confocal microscopy or

charge-coupled devices (CCD) in wide-field systems. In image processing the noise level can be quantitated using the signal-to-noise ratio (SNR) given as

$$SNR = \frac{\bar{I}}{\sigma(I)}$$

meaning the mean pixel intensity $\bar{I}$ to the standard deviation of pixel intensities. The SNR scales with the square root of collected photons N, so $SNR \propto \sqrt{N}$. The N can not be increased arbitrarily in live cell experiments due to constraints on collection time and phototoxicity. Nevertheless, noise tends to produce artifacts in image segmentation and therefore image processing is required to reduce the influence of noise in the image. This is done by image filtering where typically a region around one pixel (filter kernel) is used to assign a new value to that pixel. This process is repeated for all pixels in the image. One can distinguish different classes of filters: linear filters, non-linear filters and edge-preserving filters (compare [17]). Typical representatives of each class will briefly be introduced here.

- The *Gaussian filter* belongs to the class of linear filters. It smoothes the image locally and behaves completely isotropic. Since gradients or edges in the image are not taken into account the Gaussian filter leads to a general blurring of the image. Because the Fourier transform of a Gaussian is another Gaussian it can be applied on a Fourier-transformed image and then transformed back. Since implementations of a fast Fourier transform (FFT) with low run-time complexity are available, the Gaussian filter is computationally cheap. Due to the unspecific nature of this filter towards any structures in the image further processing, in particular segmentation, is limited with this filter. An example of a microscopic image with Gaussian filtering is given in figure 1.14 B.

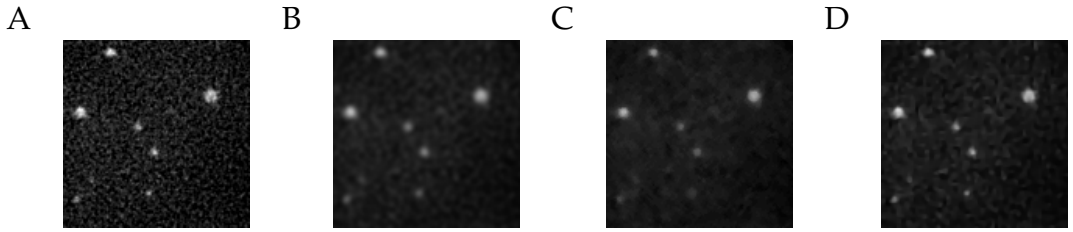

Figure 1.14: Noise reduction in microscopic images. An image of a cell nucleus transfected with PML protein-CFP is shown after contrast enhancement (A). Noise reduction on this image is performed using a Gaussian filter with kernel size 3 x 3 (B), median filter with kernel size 3 x 3 (C) and anisotropic diffusion filtering (D). Edge preservation increases visibly from B to D.

- The *Median filter* is a non-linear filter. It acts as a low-pass filter removing shot noise (high frequency noise) efficiently while preserving larger structures. Therefore edges are better defined in median filtered images. Due to its non-linear nature this filter has no equivalent in the Fourier domain and computation time is longer than with a Gaussian filter. An example of a microscopic image with median filtering is given in figure 1.14 C.

- As discussed above, Gaussian filtering and median filtering lead to a loss in edges and fine structure in an image. Therefore *edge-preserving* approaches have been devised. The most prominent example of an edge-preserving filter is the anisotropic diffusion filter. The idea behind the anisotropic diffusion filter is that the Gaussian filter is a single time-point in the solution of the diffusion equation. The initial condition is the unfiltered image. The anisotropic diffusion filter contains a term for a variable permeability (or "conductance" if the analogous heat equation is used). The permeability term depends on the differential structure of the image as measured by the gradient magnitude. Therefore, one can limit the extent of filtering to homogeneous image regions, while filtering across edges, where the gradient magnitude is large is minimized. The utility of the anisotropic diffusion filter has been demonstrated in previous works ([14, 66, 180]).

The implementation of the anisotropic diffusion filter used in this work was published in ([89]). An example is given in figure 1.14 D.

Image segmentation

The goal of image segmentation is to simplify an image or to extract objects which are subsequently more simple to analyse. The process of segmentation leads to a partitioning of the image into multiple regions (i.e. sets of pixels). Segmentation is needed in this work to define boundary conditions for reaction-diffusion modeling, extract nuclear bodies from 4D-image series and to find corresponding gray value information . There is a large number of different strategies being used in biomedical imaging. Some of those strategies used in this work will be outlined below:

- *Gradient-based* filters rely on the computation of local derivatives in the image. The gradients are large where image intensities change on short length scales in the space domain or high frequencies in the frequency domain. Therefore, gradient-based filters can be applied to Fourier-transformed images. Since high frequencies have large gradients, gradient filters can enhance fine structures like edges and small objects in an image. Since shot noise typically affects the high frequency components of an image gradient based filters are susceptible to it, meaning they produce noise artifacts. Common examples are Laplace, Sobel and Canny filters. An examples of the latter is given in figure 1.15 B. In this work an implementation of the Canny filter [35] was used as part of the IMAGEJ plug-in FEATUREJ ([118]).

- Related to gradient-based techniques is the *structure tensor*. Partial derivatives have information on the direction of gradients and can therefore be used in edge detection (figure 1.16 A). Edges of isotropic structures, however, can not be represented in this way, because the

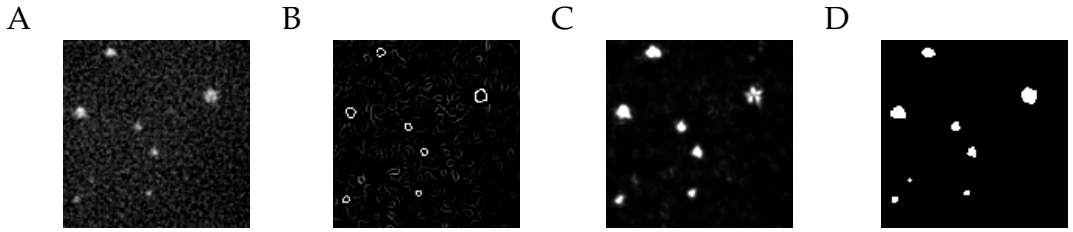

Figure 1.15: Segmentation in image processing leads to a partitioning of an image into different classes. Often an edge-detection step is succeeded by a thresholding step or the thresholding is carried out directly. An image of a cell nucleus transfected with PML-CFP after normalization and anisotropic diffusion filtering is shown in (A). A Canny edge-detection filter is shown in (B). Clearly, the susceptibility to noise of the Canny approach is evident. Application of the structure tensor is shown in (C). The eigen-image of the smallest eigenvalue is displayed. The entropy thresholding as an example for histogram-based methods is shown in (D) resulting directly in a binarized image.

directional component cancels out (figure 1.16 B). The structure tensor combines all partial derivatives of an image (figure 1.16 C). Its eigenvalue decomposition yields eigen-vectors representing the normals and tangents of an edge and the eigenvalues. The latter are a measure of the certainty of an edge (figure 1.16 D). This measure is also referred to as the coherence. This feature of the structure tensor is particularly useful in edge detection of corners or globular structures such as PML NBs. An example is given in figure 1.15 C. In this work the implementation of an edge detection filter based on the structure tensor realized in the FEATUREJ plug-in was used ([118], for more details see [140, 190]).

- *Histogram based* methods are common to global thresholding techniques. They have in common that a global threshold is determined based on statistical properties of the image histogram. Subsequently the image is partitioned into two classes according to their pixel gray values being larger or smaller than the threshold, respectively. Common examples of this strategy are Otsu's method or the entropy

A

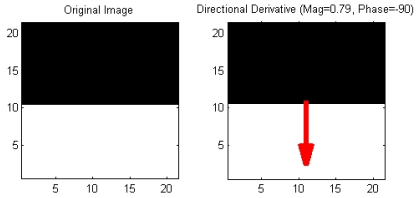

B

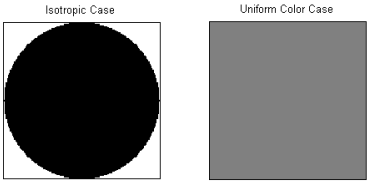

C

$$S = \begin{bmatrix} I_x^2 & I_{xy} \\ I_{xy} & I_y^2 \end{bmatrix}$$

D

$$c = \begin{cases} \left(\frac{\lambda_1 - \lambda_2}{\lambda_1 + \lambda_2}\right)^2 & if\ (\lambda_1 + \lambda_2) > 0 \\ 0 & otherwise \end{cases}$$

Figure 1.16: Principle of structure tensor. Gradient-based segmentation often makes use of the directional derivative (A) in which the direction of the gradient is expressed as a normal vector (A, red arrow). In case of isotropic gradients the directional derivative cancels out (B) yielding the same result as in a uniform case. The Structure tensor S is computed as the first-order and second-order image derivatives (C). Eigenvalue decomposition yields the eigen-vectors $\vec{e}_n$and the eigenvalues λ_n. A function of the latter is the coherence c which can distinguish between isotropic and uniform cases. Adapted from [8].

thresholding employed in this work. In both methods the underlying assumption is that there are two classes of pixels (e.g. foreground and background) and the optimal threshold is found automatically. In entropy thresholding the entropy statistic $S = -\sum p \cdot \log_2 p$ (with p standing for the probability of a gray value) is used to define the threshold. Both methods have been implemented in the IMAGEJ plug-in Multi-thresholder [16]. An example is given in figure 1.15 D.

- In *Region-growing* segmentation an arbitrarily chosen or user-defined seed pixel is taken as a starting point for a segmented image region. Based on a statistic s.a. mean value or standard deviation of surrounding pixel gray values, the similarity of the surrounding pixels is evaluated. Pixels that are classified as similar are added to the region, while pixels which aren't act as starting points for new regions. The process terminates if all image pixels belong to a region. A simple region-growing scheme was used in this work to find corresponding gray values in a chromatin channel to each nuclear body in a segmented image (see chapter 3.2.5).

Image registration

Imaging of biological processes with live cells is often affected by mechanical drift or instabilities in the imaging setup on the one hand and by movement or deformations of live cells on the other hand. Since the main goals of this work are related to extracting quantitative information about movement in live cells one important task of image pre-processing is to separate movement of cells or cell nuclei from the movement of subnuclear structures or protein populations which are to be analyzed. This separation can be realized by tracking the global movement of the cell or nucleus, registering the image series and performing motion analysis on the transformed image series. The underlying assumption of image registration is that there exists a geometric transformation which maps each

point at time t in an image series to homologous points in the subsequent image at time $t + 1$. Image registration is therefore the process of finding an optimal transformation which performs this mapping. In this process one image is defined as the reference, often the first image in the series. There are several types of registration of increasing complexity, i.e. with increasing degrees of freedom:

- Rigid registration is the most commonly applied form of registration. Possible transformations are translation, rotation and reflection. The advantage is that there are many implementations available and that it is the computationally most inexpensive registration scheme. It is also often the first step in a registration workflow before further transformations are applied.
- Affine registration allows all transformations of rigid registration plus shearing and uniform or non-uniform scaling.
- Elastic registration allows the most complex transformations including local and global deformations.

Image registration is very common in medical and clinical contexts, where there is a high pressure to achieve a large through-put with image analysis in diagnostics, such as PET, MRT and CT images as well as in radiotherapy where a localized radiation dosage must be applied. In contrast, in the context of biological imaging registration is still not a standard. Due to the large variability of cellular or subcellular morphology usually automated landmark-based approaches (compare [149, 150]) are not feasible in live cell studies. Instead, edge-based or gray value-based registration is necessary (see also [12, 14]). The former requires obligatory segmentation of cellular or nuclear morphology as described above.

Chapter 2

Objectives

Cell biological imaging is rapidly being transformed from a mainly phenomenological discipline into a science which is driven by the acquisition and analysis of quantitative data. The organizational complexity of living cells is becoming more and more understood as a complex interplay of protein ensembles and aggregations whose spatio-temporal organization is tightly regulated. Its striking dynamics follows cellular functions and the cell cycle to allow cells to adapt to a multitude of internal and environmental signals. In many cases the formation and dissolution of macromolecular complexes is only transient for as long as their physiological function is needed. One striking example of such adaptability is the cell nucleus. While its overall organization is dominated by chromatin structure, there exists a complex array of nuclear bodies and other substructures. The intricate structural and functional flexibility of the nucleus is a paradigm of the spatial and temporal orchestration of living cells. In this work I establish methods which allow a detailed and quantitative study of nuclear organization on the level of chromatin and nuclear bodies. I use histone H1° as an example of a protein which stabilizes chromatin secondary structures and PML bodies (PML NBs) as examples of nuclear bodies.

Linker histones are ubiquitously expressed and evolutionaryly conserved,

yet their function remains somewhat ambiguous between an overall stabilizer of heterochromatin and a modulator of chromatin remodeling as introduced in chapter 1.2. Point mutants in the globular domain of H1° were mutated and tested semi-quantitatively using FRAP experiments as reported in [28]. These amino acid residues represent potential candidates to confer binding of linker histone to the nucleosome dyad. Seven of these mutants along with the wild-type were available as GFP-fusions in stable cell lines. These fusion proteins represent molecules of almost equal molecular weight and size. They can safely be expected not to differ in their diffusive mobility. Since they are tightly bound to chromatin their diffusion is slowed down. The question of this part of the work was therefore to establish a scheme using FRAP analysis in conjunction with numerical modeling of a reaction-diffusion system which would allow one to differentiate between the diffusive contribution to the ensemble mobility and the binding. At the beginning of this work a comprehensive implementation of such a reaction-diffusion model suitable to this goal was not available. Also, the above mentioned H1°-GFP mutants had not been fully developed and the respective semi-quantitative FRAP analysis was published during this work by my collaborators. An additional goal was to derive a more detailed quantitative description of the binding H1°-GFP which relates to the binding equlibrium rather than an arbitrary recovery time which has no counterpart in chemical reaction kinetics. A suitable model which correclty describes the macroscopic diffusion of H1°-GFP and its mutants in the cell nucleus needed to be established. The software Tropical which implements the reaction-diffusion model needed as well as numerical parameter estimation was tailored to the analysis of FRAP experiments. It was designed and produced in collaboration with Markus Ulrich at the group of Prof. Dr. Roland Eils.

Nuclear bodies represent a diverse group of multiprotein complexes visible inside the nucleus. They serve a multitude of different physiological functions and are often related to diseases. In particular, PML bodies have been named after an acute form of leukimia (as outlined in 1.4). Most nuclear bodies disassemble during mitosis and reform at the end of

it. Because of this a quantitative analysis of their dynamics during mitosis was lacking at the beginning of this work, while data was available on their movement during interphase ([70]). So, one challenge to overcome was to find conditions for microscopy and image processing which allowed to perform single particle tracking until they aggregate to form MAPPs and eventually dissolve. MAPP formation was to be quantitated. Due to the gross reorganization of the nucleus during early mitosis until NEBD I could expect dramatic differences between interphase and prophase. These changes were to be quantifyed. It had been completely elusive what mechanism might cause such changes in PML NB dynamics. Among possible candidates were dissociation from possible direct or indirect chromatin interaction, topological reorganzatin of the interchromatin domain or physical flow caused by morphological changes of the nucleus and eventually NEBD with concomittant release of material into the cytoplasm. It was therefore an important task to investigate such potential causative processes and ideally to differentiate between them. Because of their size around ~1 µm NBs are sutiable to probe not only their own dynamics but also the structure of chromatin domains and their permeability. So PML NBs represent an indirect reporter for gross reorganization of the nucleus during early mitosis and its effect on large macromolecular assemblies. It was therefore the goal of this part of the work to characterize and quantitatively describe PML NB dynamics and to relate it to chromatin condensation and other important events during mitosis such as NEBD and mitotic checkpoints.

Chapter 3

Materials & Methods

3.1 Histone H1° dynamics in the nucleus

3.1.1 Available GFP clones of H1°

A number of mutants in the globular domain of H1° were produced and published by Brown et al. [28]. The point mutations were modified in those residues which convey nucleosomal contacts. Mutations have been set within basic and charged residues of the globular protein domain. Next to the wild-type (WT), the following mutations were available (see table 3.1).

Basic residues, which are conserved between H1° and other variants (R47, R74, R97, K59), were substituted with alanine (A), whereas non-conserved residues (K82, H25, E62) were replaced with the residue most commonly found in other variants.

Mutant name	Amino acid substitution	FRAP recovery time $t_{1/2}$ [s]
TM069	R47A	5
TM109	K82V	63
TM150	H25G	12
TM152	K59A	37
TM158	E62H	76
TM159	R74A	14
TM160	K97A	20
WT	-	52

Table 3.1: Available mutations of H1° of amino acid residues in the globular domain. Cell lines stably expressing GPF-fusions of these mutants were a generous gift by T. Misteli. A previous study suggested differential binding behaviour for the different mutants as expressed in different FRAP recovery times to reach 50 % of the initial intensity in the bleached region [28].

3.1.2 Cell culture

Stable cell lines of 3T3 murine embryonic fibroblasts (generous gift by T. Misteli and described in [28]) containing the Histone H1° variants (i.e. their respective GFP-fusions) on plasmid MTH10GFPneo were available. The cells were thawed from -70 °C stocks and cultured in 25 cm² flasks with DMEM medium (Invitrogen, order# 31885-023) at 37°C. Depending on the mutation of H1°, some of the variant strains grew very slowly compared to others. The slow growing cells cultured with additional 10% (v/v) fetal calf serum (FCS) to increase the available growth factor concentration. For imaging cells were seeded on 4-well LabTek chambers (Nalgene / nunc, Neerijse, Belgium) with cover slip bottom.

3.1.3 Live cell imaging

Cells were washed twice with 1X PBS and cultured in phenol red-free DMEM containing 20 mM HEPES buffer immediately for imaging. Temperature was held constant close to 37° C by an air blower and an objective heating ring. Image recording was performed on both, the Leica TCS

SP2 and the Leica TCS SP5 (Leica Microsystems, Wetzlar, Germany) confocal microscopes. In order to achieve a more cylindrical bleach profile along the z-axis a 40x NA 1.0 objective lens was used and the pinhole was half-opened (set to 4 Airy units). The gain on the photomultiplier tubes (PMTs) was set to 700-750 V. In order to achieve a good time resolution the highest scan speed available was used. On the SP5 the scanner worked in resonance mode (8000 Hz line frequency) and on the SP2 the scanner worked in bidirectional mode at 2800 Hz. The higher scan speed of the SP5 allowed the use of two times line averaging as signal to noise is quite critical for modeling later-on. Scan format was 256x256 pixels at a scanner zoom between 10 and 14 resulting in a an x/y-dimension around 100 nm. Thus, the Nyquist condition was upheld with regard to optical resolution. GFP was imaged using the 488 laser line of the Ar/KrAr laser at 1-2 % transmission and 75 % tube current. Bleaching was achieved at 100 % transmission of the 488 laser line and by adding the lines 458, 476 and the 405 Diode laser (SP5) or reducing the beam expander (SP2) to underfill the back aperture of the objective lens. Each cell was visually inspected for "healthy" morphology immediately before imaging.

3.1.4 Fluorescence recovery after photobleaching (FRAP)

FRAP experiments were performed on bright nuclei focused on a middle section using the FRAP wizard provided by the microscope software. Two bleaching geometries were used: Either a 3 µm circular region of interest (ROI) was bleached (in the following called spot-bleaching) or a region comprising about 30-50% of the cell nucleus was bleached (in the following called half-bleaching). Each FRAP experiment followed the basic principle of recording 10 pre-bleach images, bleach images using the ROI-bleach function and three post-bleach steps of increasing time intervals. On the SP5 6-8 bleach iterations were used, equivalent to 300-400 ms bleaching time. On the SP2 only 2 iterations were needed due to a different setting for the beam expander, resulting in ~ 200 ms bleaching time.

The post-bleach intervals were set as to observe each nucleus for 10 - 15 min after bleaching depending on the H1° mutant under study.

3.1.5 Correction of undesired bleaching in FRAP image series

Bleaching larger geometries in FRAP experiments results in a net loss of total fluorescence in a cell or compartment such as the nucleus. As a result of this the fluorescence can not recover to its initial level fully. Moreover, as photobleaching also occurs during post-bleach acquisition, if at a slower rate, more fluorescence is lost, which can make it difficult to recognize the terminal fluorescence intensity. For the numerical simulation it is crucial to exclude any bleaching effects from the data as this would complicate the model and would require more unknown parameters to be estimated. Therefore, correction for undesired bleaching is performed on the FRAP image series, where the mean intensity in the nucleus at each time step i is related to the initial intensity of the entire cell nucleus ROI. A background subtraction is performed at the same time. The corrected image series $F_{xy,corr}\,(t)$ is computed as

$$F_{xy,corr}\,(t) = F_{xy}\,(t) \cdot \frac{ROI(0) - b(t)}{ROI\,(t) - b(t)}$$

with $F_{xy}\,(t)$.. time dependent FRAP image, $ROI(0)$..mean fluorescence intenstiy before bleaching in the whole nucleus, $ROI(t)$.. time dependent mean fluorescence intensity in whole nucleus, $b(t)$..time dependent background intensity.

An IMAGEJ macro was produced which expects two geometries, one for the cell nucleus and one for a background region-of-interest to be selected in IMAGEJ's mask tool. These IMAGEJ masks were generated by using the

magic wand tool on binary masks of the cell nucleus. The source code is provided on the enclosed CD-ROM. Installation instructions and documentation are given in the Appendix 6.2.6.

3.1.6 Image registration

Due to movement of the cells during post-bleach image acquisition a registration scheme is needed to remove it. A custom macro for IMAGEJ (ImageJ `http://rsb.info.nih.gov/ij/`) reconstructs the image series from exported microscopy images in Tiff format. Next, the images are registered to the first pre-bleach image using a rigid registration scheme as implemented in the IMAGEJ plug-in TURBOREG (TurboReg `http://bigwww.epfl.ch/thevenaz/turboreg/`). The latter is called by the macro using its command-line interface to enable scripting of the registration process. Since file names differ between the Leica SP2 and the Leica SP5 and because registration uses different parameters for half-bleached and spot-bleached nuclei the macro exists in three versions, respectively. The source code is found on the enclosed CD-ROM. Documentation is provided in the appendix (see chapters 6.2.2, 6.2.3).

3.1.7 Image segmentation

For an accurate read-out of intensity information the bleached and the non-bleached region as well as the overall morphology of the nucleus need to be well defined by masks. Three binary masks per cell were generated: One for the bleached region, one for the non-bleached region and one for the whole nucleus. The latter served as a boundary condition in numerical simulations, while the former served to define the area for parameter estimation and to read out average intensity over time. Mask generation was performed by an automated macro in IMAGEJ (ImageJ

http://rsb.info.nih.gov/ij/) performing noise reduction and subsequent edge detection. Since two different types of FRAP experiments were performed, namely spot bleaching and bleaching of half cell nuclei, two different macros were developed. The source code is found on the enclosed CD-ROM. Documentation is provided in the appendix (see chapters 6.2.4, 6.2.5).

Mask generation in spot-bleached cell nuclei

The macro reads in 3 values from the user, number of pre-bleach images, number of post-bleach images and smoothing scale for the egde detection filter. First the mean image is computed from the pre-bleach images (figure 3.1 A). This mean pre-bleach image is then used for generation of a mask comprising the entire nucleus. For this procedure seven steps are used: gradient magnitude implemented in the FeatureJ Edge detection plugin with smoothing scale = 4 and suppression of non-maximum gradients turned on (FeatureJ http://www.imagescience.org/meijering/software/featurej/, figure 3.1 B), logarithm (figure 3.1 C), Otsu thresholding, gaussian blur with kernel 2, Otsu thresholding, region growing fill and erosion. The logarithm is necessary to equalize inensity levels before thresholding (dynamic compression), the gaussian blur is needed to close "holes" in the edge which may occur after Otsu thresholding. Erosion decreases the size of the mask which has grown slightly due to Gaussian blur. The result is seen in figure 3.1 D. Next, the mask for the bleached region is created by deviding the pre-bleach image with the first post-bleach image (figure 3.1 E). This results in an image where, the bleached pixels light up (figure 3.1 F). This ratio image is then segmented using six steps: median filter (kernel size 7), squared twice (to increase contrast), entropy thresholding, region growing fill and despeckle. The result is seen in figure 3.1 G. Finally, the mask of the non-bleached region is created by subtracting the bleached region mask from the mask of the whole nucleus (figure 3.1 H). The source code of the macro is found in the enclosed CD-ROM. Documentation is

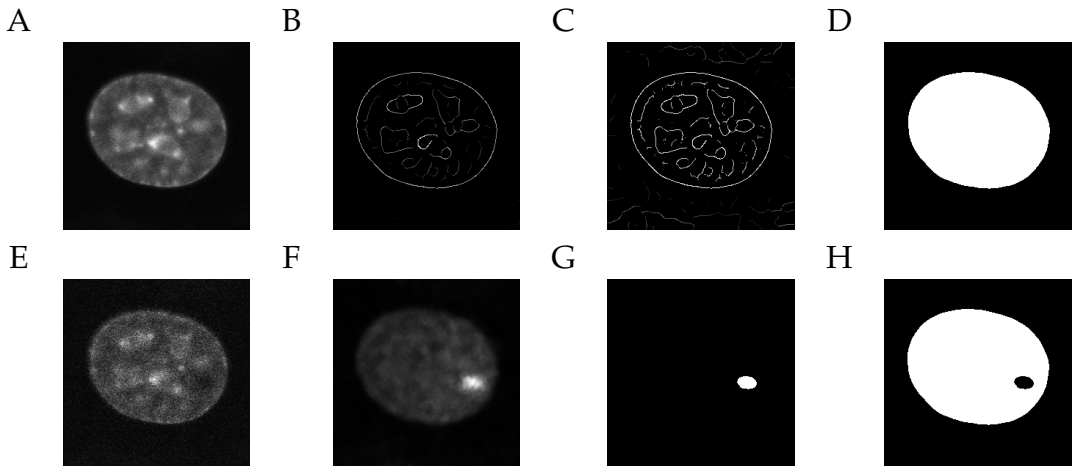

Figure 3.1: Mask generation workflow for spot bleached nuclei. Three binary masks (D, G, H) are generated from the mean pre-bleach image (A) and the post-bleach image (E). Segmentation of the pre-bleach image yields a mask of the entire nucleus (D) by gradient magnitude edge detection (B), logarithm (C), thresholding, smoothing and filling (D). A mask of the bleached (G) and non-bleached (H) regions is created by computing a ratio between pre-bleach and post-bleach (E) images (F), contrast enhancement and thresholding (G) and mask subtraction (H). For a detailed description see 3.1.7.

provided in the appendix (see chapter 6.2.4).

Mask generation in half-bleached cell nuclei

Creation of the mask for the entire nucleus is analogous to the case of spot-bleached nuclei with the only exception of the Otsu thresholding being replaced by Maximum Entropy thresholding (figure 3.2 A-D).
Generation of the mask for the bleached region differs, however. The above mentioned approach to use a ratio image of pre-bleach and post-bleach images works less well in this case, because the bleached region is larger and comprises a more heterogenous intensity distribution. Therefore, it is more practical to generate the mask of the non-bleached region first from the post-bleach image (figure 3.2 E). The post-bleach image is pre-processed by computation of the structure tensor as implemented in

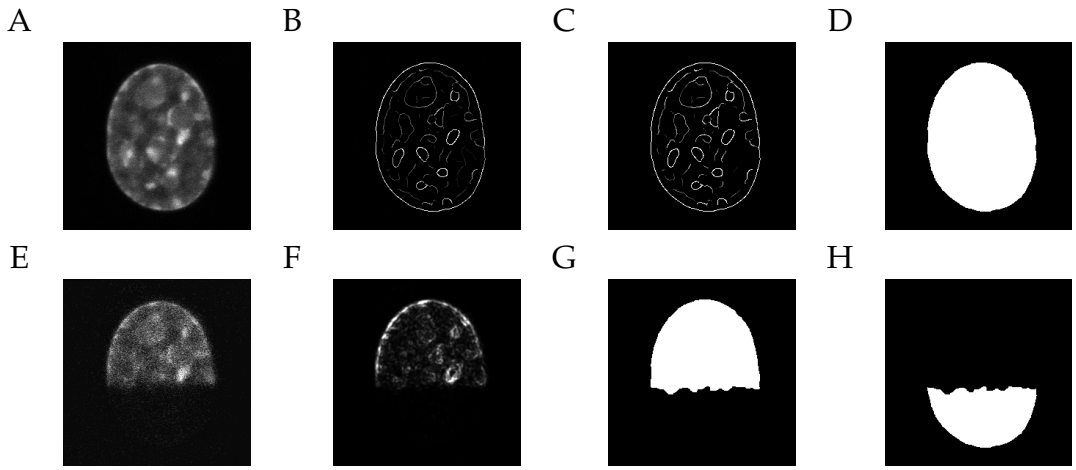

Figure 3.2: Mask generation workflow for half-bleached nuclei. Three binary masks (D, G, H) are generated from the mean pre-bleach image (A) and the post-bleach image (E). Segmentation of the pre-bleach image yields a mask of the entire nucleus (D) by gradient magnitude edge detection (B), logarithm (C), thresholding, smoothing and filling (D). A mask of the non-bleached (G) and bleached (H) regions is created by computing a the structure tensor of the post-bleach (E) image, mixture modeling thresholding, despeckle, whole filling, binary opening (G) and mask multiplication (H). For a detailed description see 3.1.7.

the FEATUREJ plug-in FJ Structure (FeatureJ `http://www.imagescience.org/meijering/software/featurej/`) with parameters largest eigenvector, smoothing=1, integration=1 (figure 3.2 F). The resulting image is segmented using the mixture modelling thresholding approach and post-processed by four iterations of despeckling, whole filling and two iterations of binary opening. The resulting mask for the non-bleached region is seen in figure 3.2 G. Finally, the mask for the bleached region is computed by multiplication of the mask for the whole nucleus and the non-bleached region (figure 3.2 H). The source code of the macro is found in the enclosed CD-ROM. Documentation is provided in the appendix (6.2.4).

3.1.8 Simulation and parameter estimation of reaction-diffusion systems

As stated in chapter 1.5.2 a reaction diffusion system can be described by a system of partial differential equations (PDE), in which state variables are a function of both time and space. The solution of this PDE system is achieved by integration to obtain, for example, the temporal development of its state variables, in my case fluorescence intensity, which in turn is proportional to the concentration of H1°-GFP. A direct solution of this PDE system is often non-trivial. Furthermore the computational cost can be higher than for systems of ordinary differential equations (ODE) for which a number of standard solvers exist. A common strategy therefore is discretization in the space domain. Hereby, the space is subdivided into small elements each of which can be treated as homogenous. Effectively, this removes the space dependence and transforms the model in to an ODE system for each space element. In this work a finite differences approach was chosen which subdivides the space into square elements. Since the FRAP data is available as digitized image series it is straightforward to use pixels with or without binning as finite elements. In order to use the real spatial domain of the nucleus a Neumann boundary condition was used. In the Neumann boundary condition material flux can only occur between grid elements which are nearest neighbours. No flux can occur across the boundaries of the domain. In terms of biology one assumes therefore that no H1°-GFP molecules can enter or leave the nucleus on the time scale of the experiment. The boundary is defined by a binary mask of the nucleus, which is generated as described in chapter 3.2.3. The solver was a the standard Runge-Kutta 4th order algorithm (see also [181]).

The observable quantity in the experiment is fluorescence intensity, which is proportional to the concentration. Therefore, the temporal development of the diffusion process (or reaction-diffusion process) is known from the experiment. What is missing are the parameters governing the pro-

cess. This parameter estimation problem is known as the inverse problem, where the process is known, but the parameters are missing. It is typical of data driven modeling. One therefore uses the strategy outlined in the following to estimate the parameters:

1. *Assume a set of start parameters*. A good choice of start parameters is important, since it may influence the outcome if local minima exist in the error function (see below).

2. *Simulate the first run* using the model, the start parameters and the boundary condition provided.

3. *Compute an error function* which quantifies the agreement of simulated and experiemental data. Memorize the error.

4. *Vary the parameters* and repeat step 3.

5. *Compare the errors from step 3 and step 4* and keep the paramters with the smaller errors as the new parameter set.

6. *Repeat steps 3 to 5 until a terminating criterion has been reached*. Such a criterion can be an error threshold or a maximum number of iterations.

As pointed out in step one picking the correct start parameters can be critical. One has to use all the knowledge available about the system to arrive at a good initial guess. One could, for example use the Stokes-Einstein relation to estimate the expected diffusion coefficient from the molecular mass. In my case the start parameter used was D = 0.1 $\mu m^2/s$ which is in the range of the diffusion coefficient found for H1°-GFP in previous studies [20]. Steps 4 and 5 contain the most of the intelligence needed in the parameters estimator. In my case a modified Levenberg-Marquard scheme was employed ([182, 181]). Quantitative analysis of FRAP experiments using Tropical was described in [182, 181] exhaustively.

3.1.9 Fluorescence correlation spectroscopy (FCS)

All FCS measurements were performed in the cytoplasm of the cell line expressing the respective H1°-GFP constructs. Measurements were performed on both, the Leica SP2 and SP5 confocal microscopes (Leica Microsystems, Mannheim) which both were outfitted with an FCS extension including avalanche photon diode detectors for single photon counting. A 63x NA 1.2 water immersion objective lens was used. Its correction ring was adjusted to maximal brightness of the cover glass reflection immediately before the measurement. This was done in xzy scan mode using the z-Galvo table. Every time the cover glass was replaced by a new one (e.g. in another sample vial) the cover glass adjustment was repeated. GFP was excited with the 488 nm line of the Ar/KrAr laser, the tube current of which was set to ~ 30%. The ideal laser power was adjusted during a test measurement in the cytoplasm to achieve a count rate of 10 - 20 kHz. This regime is a good compromise between achieving an acceptable signal-to-noise ratio while avoiding excessive photobleaching of GFP. A typical AOTF setting was ~ 25 %. The acquisition time was 50 s.
Curve fitting and parameter estimation were performed in MATLAB using a 3D-diffusion model which includes a term for the triplet state of GFP and an α parameter for anomalous diffusion (see figure 1.12 D). The estimated diffusion times τ_D were used to compute a diffusion coefficient according to $D = \omega^2/(4 \cdot \tau_D)$. Here ω signifies the beam waist. From calibration measurements with Alexa488 dye in water it was known to be $\omega = 210$nm.

3.2 Dynamics of PML nuclear bodies during mitosis

Experiments for single particle tracking of PML NBs were conducted using a double stable cell line expressing PML-ECFP and EYFP-Sp100 as de-

scribed in ([38]).

3.2.1 Microscopy and live cell imaging

Cells were seeded onto MatTek glass bottom micro-wells and grown for 2 days before imaging. Chromatin was visualized either by transient transfection of H2A-mCherry or by staining with Hoechst 33342 for 5 min at the final concentration of 0.2 $\mu g/ml$. Before imaging began, cells were changed into Leibovitz's L-15 medium (Gibco) supplemented with 30% FBS before being mounted onto the stage of a DeltaVision RT microscope (Applied Precision) with a PlanApo 60x 1.40 n.a. objective lens (Olympus America, Inc., Center Valley, PA). Temperature was maintained at 37°C using an environmental chamber. The images were collected in different channels with 35 ms to 50 ms exposure time and deconvolved by using SoftWoRx software.

3.2.2 Image registration

Image registration was performed on chromatin images. Chromatin was visualized either by transient transfection of H2A-mCherry or by staining with Hoechst 33342 for 5 min at the final concentration of 0.2 $\mu g/ml$. Rigid registration was performed on a a reference plane using ImageJ (ImageJ `http://rsb.info.nih.gov/ij/`) and the TurboReg plug-in (TurboReg `http://bigwww.epfl.ch/thevenaz/turboreg/`). In the case of Hoechst staining a single z-section mid-nucleus was recorded in case of H2A-mCherry a z-Projection of the cell nucleus was chosen as the reference plane. The resulting transformation matrix was stored and applied to all z-Slices in each z-Stack of PML NBs (see Figure 3.3).

This was done via a custom macro script for TurboReg (source code on the enclosed CD-ROM, documentation in the Appendix 6.2.1). The macro

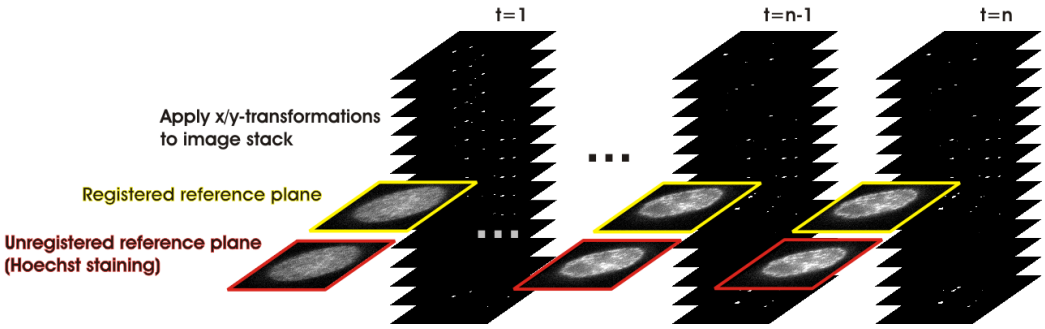

Figure 3.3: Registration with reference plane. Transformations from a z-projected reference plane in chromatin images are applied to image stacks containing PML NB images.

reads in paths to source images and transformed images, the z- and t-dimensions of the image series and the path to the landmark file containing the transformations from the user. The TurboReg macro interface is documented on its web site (TurboReg `http://bigwww.epfl.ch/thevenaz/turboreg/`).

3.2.3 Image segmentation

Images were segmented to define regions of the images as trackable particles. Eight steps were used for segmentation:

1. background subtraction
2. normalization
3. anisotropic diffusion filtering
4. structure tensor calculation
5. logarithm filtering

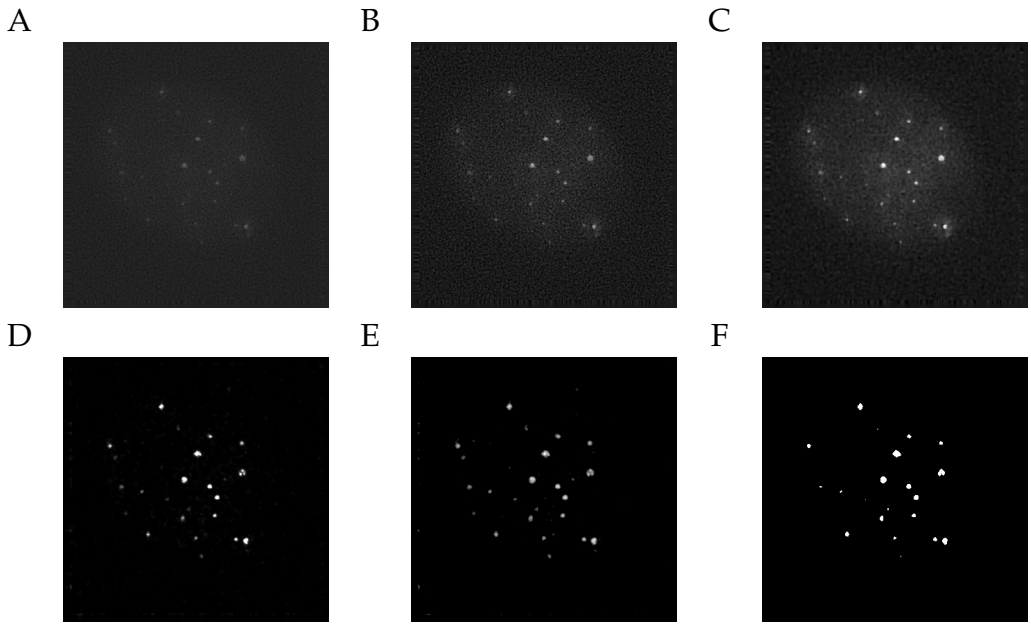

Figure 3.4: Image processing workflow for segmentation. Z-Projection of image stack (A), background subtraction and normalization (B), anisotropic diffusion filtering (C), structure tensor (D), logarithm filter (E), entropy thresholding and cleanup (F).

6. global maximum entropy thresholding
7. De-speckling
8. Hole filling

All these steps were performed in ImageJ using standard ImageJ functions (step 1, 2, 5, 7, and 8) or freeware plug-ins, including the edge preserving anisotropic diffusion (step 3), the FeatureJ (step 4), and the Multi-thresholder plug-in (step 6). Figure 3.4 shows steps 1-2 (A), 3 (C), 4 (D), 5 (E) and 6-8 (F) on an example stack. The anisotropic diffusion plug-in was implemented by Vladimir Pilny (Anisotropic diffusion `http://rsb.info.nih.gov/ij/plugins/anisotropic-diffusion-2d.html`). The FeatureJ plug-in was written by Erik Meijering (FeatureJ `http://www.imagescience.org/meijering/software/featurej/`). The multi-thresholder plug-in was written by Kevin Baler (MultiThresholder `http://rsb.info.nih.gov/ij/`

Filter:	anisotropic diffusion	structure tensor	multi-thresholder
iterations	20	-	-
a1 (minimal variations)	0.25	-	-
a2 (maximal variations)	0.45	-	-
time step	20	-	-
edge threshold	5	-	-
eigen-vector of structure tensor	-	smallest	-
smoothing scale	-	1	-
integration scale	-	1	-
Multi-thresholder type	-	-	Maximum Entropy

Table 3.2: Summary of segmentation parameters used on PML NB 4D image series.

`plugins/multi-thresholder.html`). It implements four different global thresholding schemes out of which the maximum entropy approach was used. A table summarizes the parameters used for the more complex filters used in steps 3, 4 and 6.

An custom ImageJ Macro was used to automate the entire workflow (source code on the enclosed CD-ROM, documentation in the Appendix 6.2.7).

3.2.4 4D-Single particle tracking

4D single particle tracking was performed using TIKAL ([13, 14, 104]). The segmented image series were imported into TIKAL via listfiles containing paths to each image. The listfiles were created using an ImageJ macro which reads in paths and dimensions of the image series from the user. (source code see enclosed CD-ROM, documentation is provided in the Appendix 6.2.8 on page 155). All tracks were manually verified and potential ambiguities were removed manually in TIKAL's interactive 4D

viewer. The length of each track and possible fusion events were counted and recorded. The 3D trajectories were exported in ASCII format for further analysis.

3.2.5 Extracting gray value information

All voxels belonging to all PML NBs are contained in the segmented image stacks. The position of each particle in time and space is known from 4D-particle tracking, but not in pixel coordinates. Both pieces of information were combined by using the position of the desired PML NB at a given time as the seed position for a region-growing filling procedure. The latter yields all voxels which belong to one PML NB at a given time. Most image stacks have a voxel size in the range of 100 nm. This resolution was chosen to achieve image oversampling. Since the optical resolution is worse than 200 nm (depending on the wavelength), one layer of voxels around those defined by segmentation was added to the set of voxels of one PML NB. The gray values in this set of voxels were read from the corresponding image stack in the chromatin channel visualized with Hoechst dye or H2A-mCherry and their mean was computed. This was repeated for each particle resulting in chromatin gray values at the position of this particle as a function of time. The entire workflow was implemented in MATLAB scripts (see Appendix 6.2.9 on page 155).

3.2.6 Movement classification

The mean square displacement (MSD) was calculated for each track in each phase, and the MSD plot was fitted using the anomalous diffusion equation, $\langle x^2 \rangle = 6D\Delta t^{\alpha}$ by non-linear regression. Where the MSD $\langle x^2 \rangle$ was plotted over time intervals Δt. The calculation was carried out as described in ([138]) and implemented in the MATLAB routine *msd.m* (see chapter 6.2.10). The anomalous diffusion coefficient (α) was estimated as

a fit parameter, and was used to classify 3 types of movement: α = 0.40 to 0.75, constrained motion. α = 0.75 to 1.25, diffusive motion. α = 1.25 to 2.00, directed motion. The percentage of tracks exhibiting a specific movement type in an image set was calculated. The distribution of different movement types from all of the image sets was summarized using a box plot. The entire workflow including curve fitting and classification was implemented in MATLAB routine *msdscript.m* (see 6.2.11). This classification of movement types was performed for both interphase control cells as well as prophase cells. The relative proportions of all three movement types for each experiment were pooled according to phase (i.e. interphase and prophase with subphases or PML prophase and Sp100 prophase). The populations where analysed both by a box-whisker-plot (e.g. figure 4.24) and by one-way analysis of variance (ANOVA) analysis. The notches in the box-whisker plot give the same information as the ANOVA analysis. For the plots the MATLAB function *boxplot.m* was used, for the ANOVA analysis the MATLAB function *anova1.m* was used.

3.2.7 Automatic detection of mobility changes

Simulation of random walks

Random walks were simulated in 1D according to the microscopic theory of diffusion ([21]). The root mean square displacement δ, i.e. the distance one particle traverses during a given time interval Δt is given as $\delta = \sqrt{2 \cdot D \cdot \Delta t^{\alpha}}$. A discrete algorithm to create one-dimensional random walks was implemented in MATLAB as *randomwalks1D.m* (see chapter 6.2.12). For the simulation of random walks having a sudden change in diffusive mobility ("break point") the last position of each simulated particle in sub-track s_n with $D_1$was used as the initial position of sub-track $s_{n+1}$with $D_2 \neq D_1$. All sub-tracks were then fused to result in a simulated series of tracks with one or more break points. This strategy was used in chapter 4.2.3.

Calculation of diffusion coefficient using a maximum likelihood estimator (MLE)

As derived in [123] the MLE for the diffusion coefficient maximises the equation

$$\hat{D} = \frac{1}{2N\delta} \sum_{i=1}^{N} \Delta_i^2$$

where N .. number of trajectories, δ.. time interval, Δ.. Euclidean distance between time t_i and t_{i+1}.
The detection of break points in trajectories is done via hypothesis testing, where the hypothesis $H_A$that there is a sudden change in diffusion coefficient at time i is tested against the null hypothesis H_0that the trajectory is uniformly random. To this end two times the log likelihood ratio (llr) is computed. The llr is a measure for the probability of a sudden change in diffusion coefficient within a given trajectory at a given index k. The log likelihood ratio can be expressed as a function of this index k which is a putative break point:

$$2 \times llr(k) = N \ln\left[\hat{D}_0\right] - k \ln\left[\hat{D}_1\right] - (N-k) \ln\left[\hat{D}_2\right]$$

where the MLEs are $\hat{D}_0 = (2N\delta)^{-1} \sum_{i=1}^{N} \Delta_i^2$, $\hat{D}_1 = (2N\delta)^{-1} \sum_{i=1}^{k} \Delta_i^2$,
$\hat{D}_2 = [2(N-k)\delta]^{-1} \sum_{i=k+1}^{N} \Delta_i^2$.
The llr results in a function with a maximum Z_N at the position of a potential break point. The trajectory under analysis can be partitioned at this break point and the llr can be computed again for the resulting subtrajectories. Due to statistical variations in displacement any random track produces a maximum in the $llr(k)$. The remaining problem therefore is how to determine the statistical significance of index k as a break point at a given confidence level. As pointed out by [123] this discrimination

A B

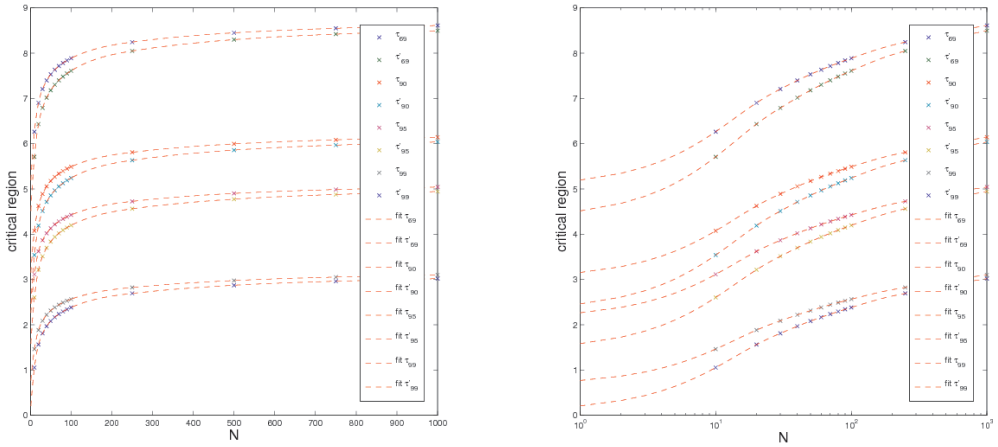

Figure 3.5: The critical region for testing the variance in a Gaussian distribution was solved numerically up to N = 1000 (e.g. time steps) and the values were tabulated in [189] for different levels of confidence, 69%, 90%, 95% and 99%. Each confidence level was calculated with a standard and a more conservative approach, labeled τ and τ', respectively. The tabulated values (colored "$\times$") were spline-interpolated (A). A semi-log plot reveals some interpolation artifacts for N < 10.

can be made by computing the critical region $C_{1-\alpha}$ where $1-\alpha$ is the confidence level and α the probability of a false-positive identification of a break point. Therefore, one tests

$$if \begin{cases} \sqrt{Z_N} \geq C_{1-\alpha}, & \text{there is a break point at index k} \\ \sqrt{Z_N} < C_{1-\alpha}, & \text{there is no break point} \end{cases}$$

The expression for the critical region for testing the variance in a Gaussian distribution was solved numerically and the values were tabulated in [189] were spline-interpolated (figure 3.5 A). The critical region was available for different discrete levels of confidence in the paper. The remaining confidence levels between 69% and 99% were again obtained by spline interpolation to cover all confidence levels in steps of 1%. Figure 3.5 B reveals interpolation artifacts for N < 10. Therefore, sub-tracks shorter than 10 time steps were not used.

The interpolated critical region was made accessible through a MATLAB

function *critical_region.m.* Other functions for computing the log likelihood ratio and a matrix containing probable break points were implemented in *logLikelihoodRatio.m* and *MLE_findDiffInterpolated.m*, respectively (see chapters 6.2.13, 6.2.14, 6.2.15). Computation of the log-likelihood ratio function and evaluation with the critical region was implemented in a recursive algorithm. The function *MLE_findDiffInterpolated.m* serves as an interface to the tracking data, performs linear interpolation (see chapter 3.2.9 and handles artifacts.

3.2.8 Validation of automatic detection scheme

Estimating the deviation of predicted break points

The deviation of predicted break points is estimated in relation to the known value t_{bp} in a simulated data set. It is calculated in analogy to the standard deviation. In contrast to the latter the reference is not the arithmetic mean of the distribution, but the known break point t_{bp}:

$$\frac{1}{N}\sqrt{\sum_{i}^{t_{max}} \left(B_i - t_{bp}\right)^2}$$

where N.. number of trajectories, B.. Matrix containing all break points in each trajectory i, t_{bp}.. known break point in simulated trajectory, t_{max}.. number of time steps per trajectory.

3.2.9 Interpolation of particle trajectories

A linear interpolation scheme was used to increase the number of data points in a trajectory. The interpolation was done by the inbuilt MATLAB function *interp1.m*. It was called from the custom script

MLE_findDiffInterpolated.m. Data on the critical region was only available for $N \leq 1000$. Interpolation typically leads to longer trajectories. Thus, an interpolated trajectory was evaluated piece-wise. The MLE approach leads to false-positive break points near the boundaries ($t = 0 \wedge t = N$). This is also true, when evaluated piece-wise. Also, there is a tendency of the MLE approach to identify several break points around the "true" break point, thereby complicating further analysis. Therefore, both the boundary artifacts as well as the latter problem are handled by introducing a parameter called "proximityTolerance". This is a user-defined minimum distance between predicted break points. Break points closer than the minimum distance are binned, i.e. replaced by their arithmetic mean. Break points closer than "proximityTolerance" to the boundaries are removed. The proximity tolerance parameter was set to 7 time steps in the analysis.

Chapter 4

Results

4.1 Histone H1° dynamics in the nucleus

The globular domain of H1 histones is highly conserved throughout evolution. A number of point mutants in the globular domain of H1° were mutated. These amino acid residues represent potential candidates to confer binding of H1 to the nucleosome dyad. They were tested semi-quantitatively using FRAP experiments as reported in [28]. Seven of these mutants along with the wild-type were analysed in this work using a combined approach of FRAP experiments and numerical modeling to study their apparent diffusion constants and binding affinity to chromatin.

4.1.1 Histone H1° diffusion can be monitored by FRAP

The H1°-GFP WT and all mutants have been shown to be functional, both biochemically and by fluorescence microscopy ([121, 28]). In particular, it was shown that in mouse 3T3 fibroblast cell lines H1°-GFP accumulates in heterochromatin foci where it colocalizes with chromatin markers Hoechst dye and HP1 ([121], [182]), while in euchromatin areas the colocalization is

not complete. A similar pattern is observed for H1°-GFP WT and the mutants used in this study (figure 4.2, left column). The linker histone H1 and many of its subtypes have been studied estensively using FRAP analysis. Many studies describe the recovery as purely reaction-controlled since H1 colocalizes with and binds to chromatin which is immobile on the time scale of typical FRAP experiments ([102, 33, 86]). Their reasoning is usually based on the trivial observation that GFP expressed in live cells, which is a *bona fide* inert molecule exhibiting pure diffusion, recovers within seconds. Since WT H1°-GFP has been reported to have a recovery half-time of ~52 s ([28]) many authors reasoned that diffusion could be neglegted since GFP recovery happens on a different time scale. This, however, is not generally the case as demonstrated by numerical modeling and experimental verification ([169, 167, 20]). In particular, in case the kinetic on-rate is large compared to the characteristic diffusion time ([169]) one can not distinguish diffusive from reactive components. In this case one can observe a recovery which can be described by a pure diffusion model ([169, 167, 20]), a regime termed effective diffusion. Such a behaviour can be experimentally verified by performing a bleaching experiment with varying sizes of the bleached area. If the recovery is at least partially governed by diffusion one should observe diffusion times which are a function of the size of the bleached area. It turns out that this is the case with H1°-GFP WT and the mutants used in this study (figure 4.1).

Another good indication for diffusive behaviour is the observation of a moving front (figure 4.2). This is in agreement with previously published works ([182, 20]). It turns out that all of the mutants used here display a fluorescence recovery which is influenced by diffusion in spite of their very different and overall long recovery times (3.1.1).
I have shown that all used mutants of H1°-GFP display a fluorescence recovery which is governed by diffusion as has been published for the wild-type previously. It has become apparent that the diffusive properties of the H1°-GFP mutants and the WT fall into the so-called “effective diffusion” regime, a concept established by Sprague et al. [169] and fur-

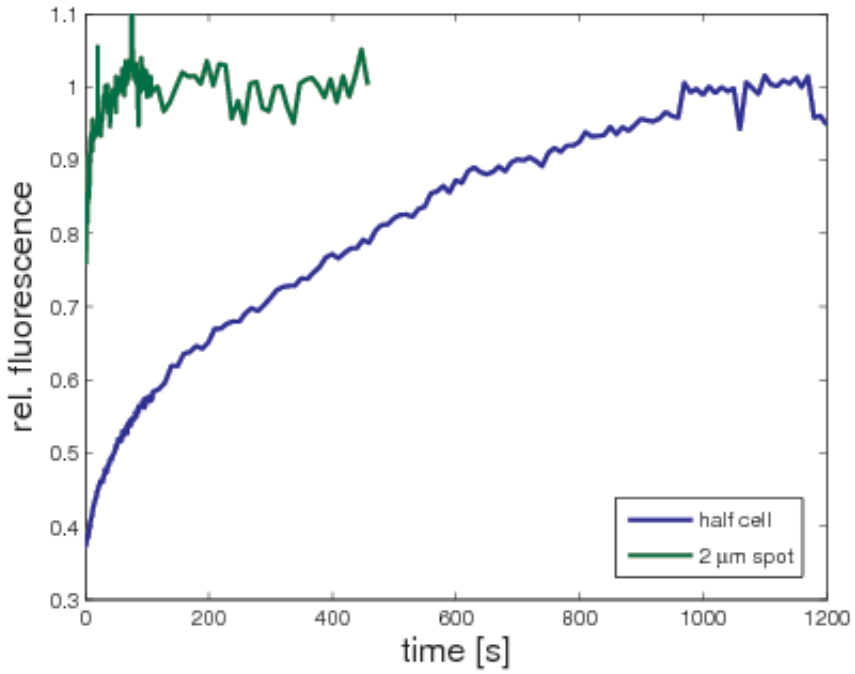

Figure 4.1: Comparison between recovery times after bleaching half the nucleus (blue line) and a 2 μm bleach spot in a euchromatin area. The strongly different recovery times suggest a recovery influenced by diffusion.

ther elaborated by Beaudouin et al. [20]. Judging from the former one can expect a fast pseudo-on-rate with $k^*_{on} > 10^3 mol \cdot s^{-1}$ (compare figure 6.1 in the Appendix), where $k^*_{on} = k_{on} \cdot S$ under the assumption of substrate S being present in excess and hence constant over time. From the latter publication one can expect to find an apparent diffusion coefficient and a constant ratio of k^*_{on}/k_{off}. In the next chapter I will explore if predictions are fulfilled and how well the pure diffusion model can fit my data.

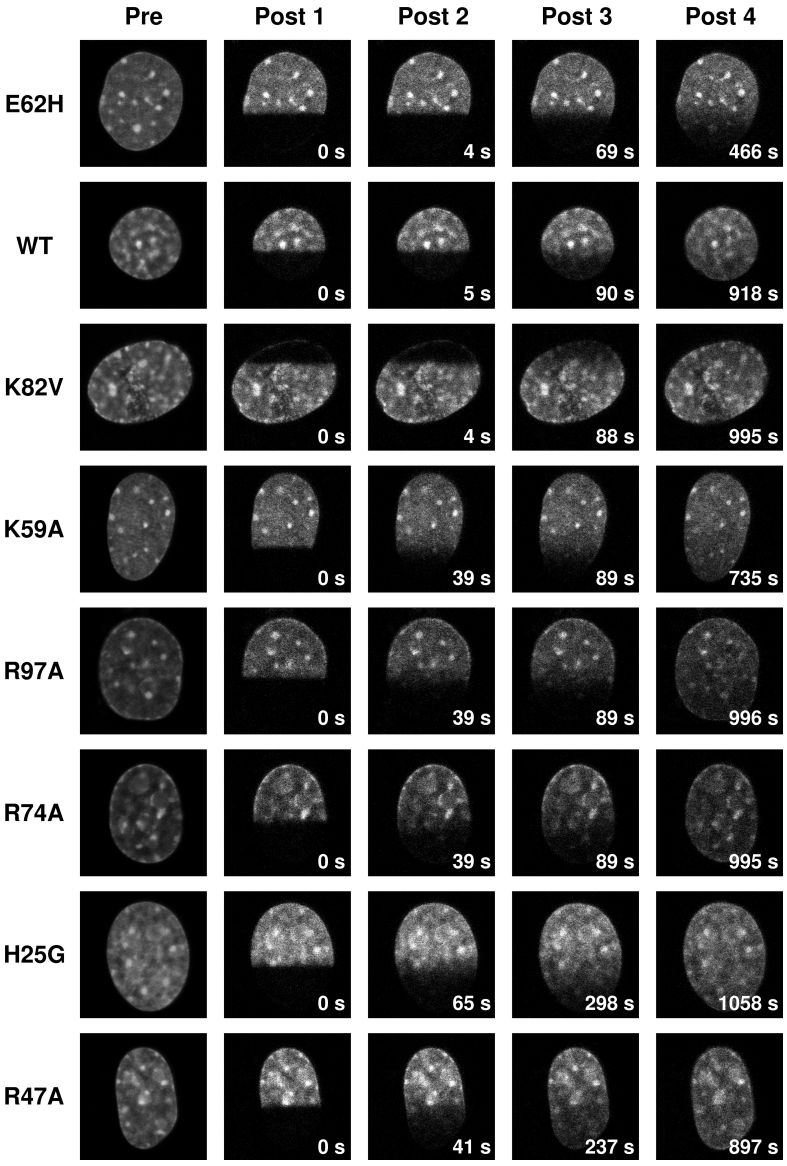

Figure 4.2: Representative time series of fluorescence recovery for all seven mutants and the wild-type (WT) used in this study. Each row represents a different point mutation as indicated on the left. The left column ("Pre") is equal to the equilibrium distribution of H1°-GFP in the nucleus before bleaching. Columns "Post 1" through "Post 4" represent consecutive time steps at different stages of the recovery. "Post 1" is equivalent to the situation immediately after bleaching, while "Post 4" shows the fluorescence distribution at the end of the recording. The elapsed time after the bleach is indicated in white. One can clearly observe a moving front in all mutants as well as in the WT indicative of a recovery which is influenced by diffusion.

4.1.2 Histone H1° mutants show differential binding behaviour

As suggested in the previous chapter the fluorescence recovery of the available mutants of H1° can be described as a pure diffusion model. The apparent or effective diffusion coefficient is then decreased depending on the binding affinity of the respective mutant compared to free diffusion of an inert protein of comparable size. In this chapter I shall perform a more detailed analysis of the reaction-diffusion system comprised of the respective H1°-GFP variant, its chromatin binding sites and the nucleoplasm. For the analysis a simulated image series was fitted to a recorded FRAP image series in the least squares sense (compare chapter 3.1.8). Model building, simulation and parameter estimation was performed using the self-developed software Tropical. Its working principles have been published in [181] and described in detail in [182].

The detailed FRAP analysis presented here involves several steps spanning conduction of the actual experiment up to parameter estimation. The entire workflow can be categorized into three groups: Wet lab, image processing and finally simulation and parameter estimation (figure 4.3). Cell culture and imaging conditions which comprise the wet lab part are described in chapters 3.1.2, 3.1.3 and 3.1.4. Of all seven mutants plus the wild-type 60 cell nuclei were bleached in half and analysed by numerical modeling. . Using different bleaching geometries enables me to utilize several fitting strategies as well as to test for diffusive behaviour of the recovery (see chapter 4.1.1).
The first step of image processing is compilation of image files and registration as described in chapter 3.1.6. This step ensures the separation of movement of the nucleus from the dynamics of the recovery. Masks are generated as Neumann boundary conditions of the whole nucleus as well as of the non-bleached and the bleached part of the nucleus. The latter region-of-interest (ROI) is used for parameter estimation in Tropical as well as for plotting mean intensities over time. Mask generation

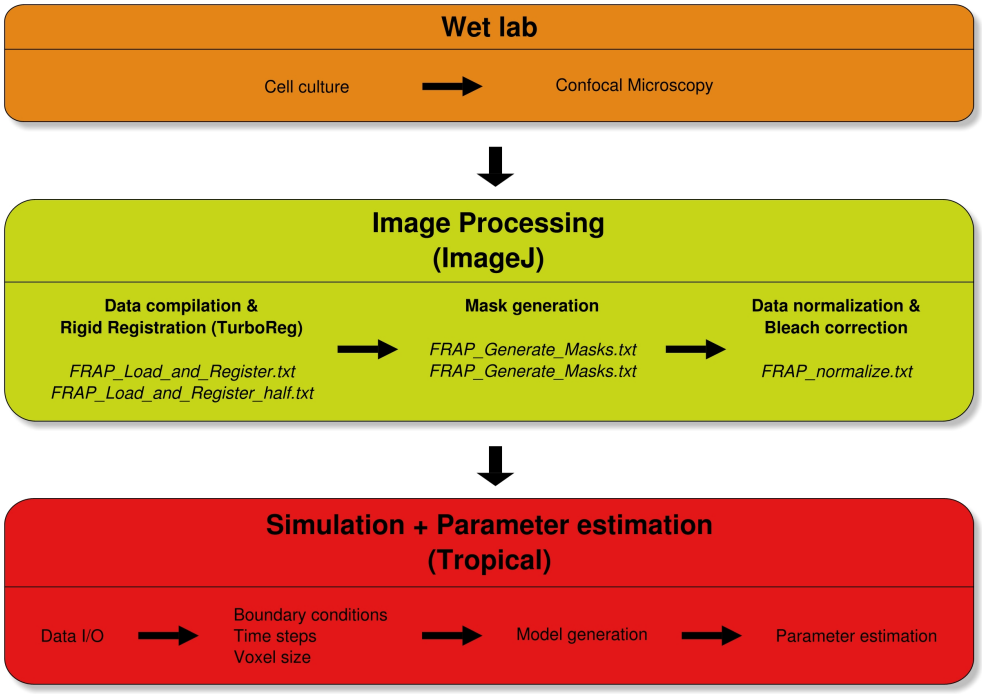

Figure 4.3: Workflow of the entire FRAP analysis of H1°-GFP. Cell lines containing GFP-labeled mutants (generous gift by Tom Misteli) were cultured as described in the methods section. Together with FRAP experiments this comprised the wet lab part of the analysis (orange box). Image processing was done in ImageJ using custom skript files as indicated (yellow box). Simulation and parameter estimation was performed in Tropical as indicated (red box).

is done by a custom IMAGEJ macro as described in 3.1.7. Image processing is completed by a normalization step in which the maximum intensity is scaled to 1 and minimum intensity to zero. Also, a correction for undesired photobleaching during post-bleach image acquisition is included as described in 3.1.5. The normalized images were read into Tropical together with image files for masks. The first post-bleach step also served as the initial condition for the simulation. Images were binned to 64x64 pixel format with each pixel representing a discrete space element on a regular grid. This finite differences discretization simplifies the model equations to ODEs (for details see chapter 3.1.8). The resulting voxel size was around 400 nm (with small deviations depending on the scanner zoom used). The standard deviation of gray values was about 1-5% for each image series and was set accordingly in Tropical. Time steps were exported from the data file in LCS or LAS AF softwares and imported into Tropical.
An image series of selected post-bleach time points of mutant R47A are given in figure 4.4, upper row. As typical of H1°-GFP one observes a drastically inhomogenous distribution of the protein. This situation is often found in live cells. In such images both the equilibrium distribution of the protein as well as the concentration changes due to diffusion are encoded as intensity values. Therefore using the post-bleach images as an initial condition for the simulation (with a simple diffusion model) leads to a smearing-out of structures. This effect is demonstrated in figure 4.4, middle row. Already after a few time steps diffusion has lead to a complete loss of structure (in fact it has the same effect as a Gaussian filter on the images). To avoid this artifact I employed an approach first suggested and described by [161]. This approach uses not the raw images, but images divided by the equilibrium distribution (i.e. the pre-bleach image). Data thus normalized does not possess the inherent structure anymore (save for some high-frequency noise in the first image). This is an attractive approach to apply a simple diffusion model to highly structured image series. It has halso been demonstrated by [20] an equivalent expression for the model works well with histone H1. The simulated images are transformed into real space after the simulation (for details see [182]). The

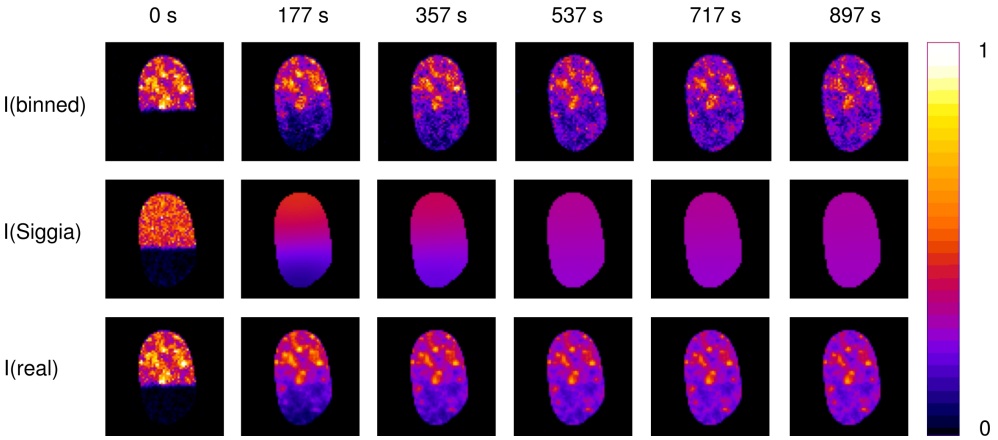

Figure 4.4: Simulation of FRAP recovery of mutant R47A. Images have been normalized to [0..1] and binned to 64x64 pixel format. Selected post-bleach time steps are shown (upper row). Simulation is carried out in Siggia normalized data space ([161], middle row). Note the initial condition also changes accordingly and becomes homogenous (save for high-frequency noise which is quickly smoothed away). The simulated images are denormalized to real data space (bottom row). The simulated images

resulting image series fits very well with the data (figure 4.4, bottom row).

Simulation and parameter estimation were carried out with seven mutants and the wild-type. Example image series are found in figures 4.5 and 4.6.

As suggested by different recovery half-times observed (also found by [28, 182]) the different mutants showed a dramatically different diffusivity. Wild-type H1°-GFP served as a reference. For this construct an apparent diffusion coefficient of $D_{eff} = 0.017 \pm 0.002 \mu m^2/s$ was observed. This value is close to the one found in [182] which is $D_{eff} = 0.022 \pm 0.008 \mu m^2/s$. All but one of the mutations lead to an increased apparent diffusion coefficient compared to the wild-type. All of those mutations which lead to an increased diffusion were ones which replaced basic residues (Lys, Arg) by neutral ones, thereby reducing positive charge. The fastest diffusing mutant displayed a diffusion coefficient of $D_{eff} = 0.094 \pm 0.030 \mu m^2/s$ which is ~ 6-times higher than the wild-type. The one mutant with a longer recovery and smaller diffusion coefficent was E62H

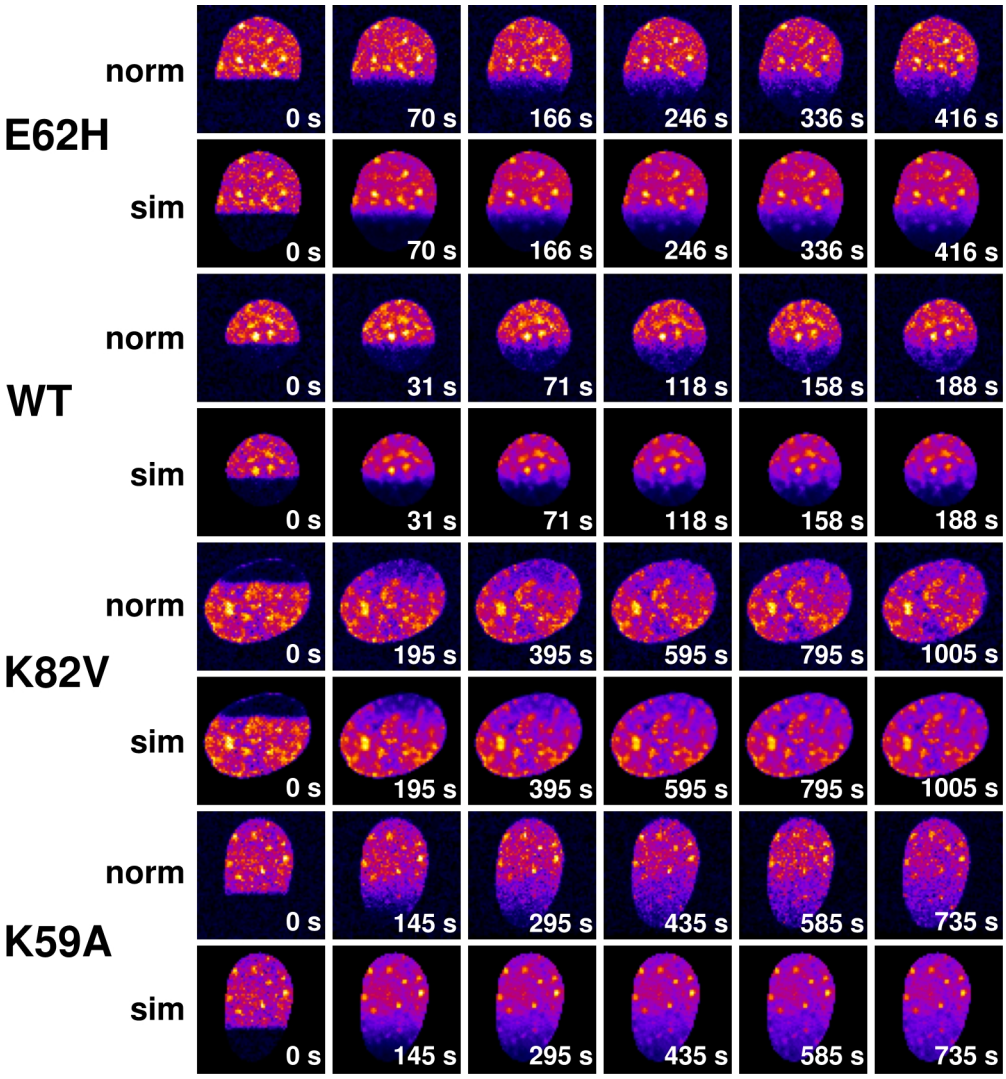

Figure 4.5: Data and image series of representative experiments with all mutants (continued in figure 4.6). Point mutations are indicated in the left column. The upper row of each mutant (norm) represents normalised and binned raw images, while the lower row of each mutants represents the simulated image series with Siggia normalisation.

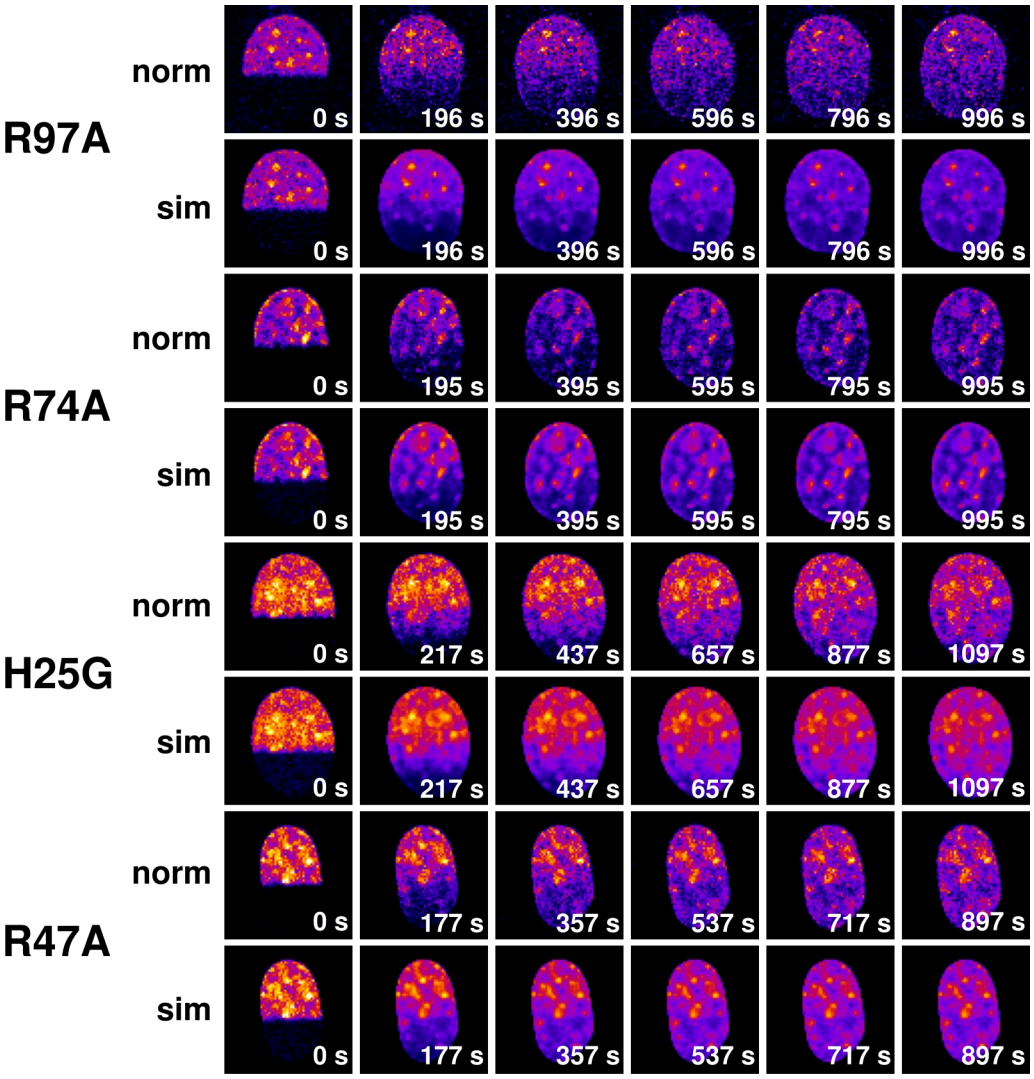

Figure 4.6: Data and image series of representative experiments with all mutants (contintuation of figure 4.5). Point mutations are indicated in the left column. The upper row of each mutant (norm) represents normalised and binned raw images, while the lower row of each mutants represents the simulated image series with Siggia normalisation.

H1° variant	D_{eff} $[\mu m^2/s]$	relative to WT [%]
E62H	0.012 ± 0.006	0.7
WT	0.017 ± 0.002	1.0
K82V	0.034 ± 0.010	2.0
K59A	0.037 ± 0.015	2.2
K97A	0.074 ± 0.005	4.5
R74A	0.076 ± 0.019	4.6
H25G	0.072 ± 0.040	4.3
R47A	0.094 ± 0.030	5.7

Table 4.1: Summary of observed effective diffusion coefficients. Diffusion coefficients are given including the standard deviation. The right column gives the relative magnitude of diffusion coefficients relative to the wild-type. Except for H25G all mutants follow the order of recovery times published by [28].

which replaces the acidic amino acid Glu by basic histidine. Its observed diffusion coefficient was $D_{eff} = 0.012 \pm 0.006 \mu m^2/s$. Table 4.1 summarizes the observed average diffusion coefficients. Evidently, the order of observed diffusion coefficients mostly matches the order of recovery times published by Brown et al. [28]. The one exception to this is mutant H25G, which appears to have a slightly slower diffusion than even K97A. However, the D_{eff} of H25G also has the largest standard deviation. Its placement with regard to observed diffusion coefficient is therefore not entirely clear. The full range of estimated parameters is shown in figure 4.7.

I have estimated effective diffusion coefficients for all seven point mutations and the wild-type of H1°-GFP. Their order correlates well with previously published data. The observed differences can only stem from differential binding, because the point mutations do not significantly influence the hydrodynamic radius of the mutants. In the next chapter I will therefore dissect the contributions to effective diffusion coefficients into a purely diffusive component and the contribution from binding.

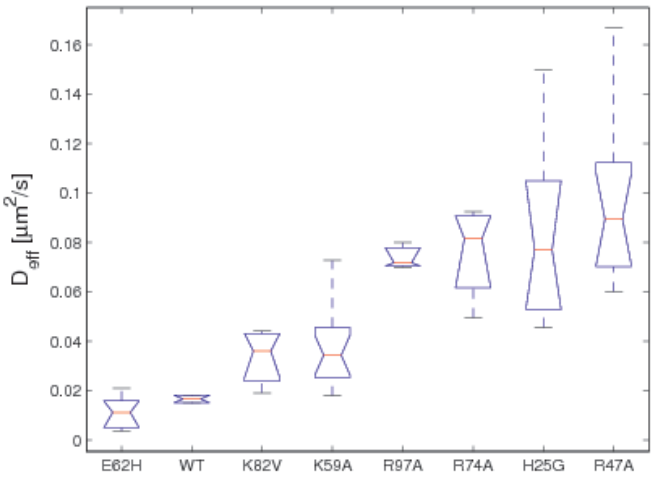

Figure 4.7: Box-whisker plot of estimated diffusion coefficients for each mutant and the wild-type (WT). Point mutations are given along the x-axis. Boxes comprise 50% of all data, medians are indicated by a red line. The notches represent an estimate of the uncertainty about the medians for box-to-box comparison. If the notch area overlaps between the two sets, the mean values of the two sets differ with 5% confidence level, in other words they do not differ significantly.

4.1.3 Estimation of bound fraction of H1°

I have so far quantitatively described the observable diffusion of each available mutant and the wild-type. This diffusive behaviour is both influenced by pure diffusion and by binding ([169, 167, 168, 20]). The original derivation was made by J. Crank ([44]). The most practical form of the expression for my purposes is

$$D_{eff} = D \cdot Free \tag{4.1}$$

with D_{eff}.. effective diffusion, D.. diffusion coefficient, $Free$.. free fraction of H1°. With the pure diffusion coefficient known one can therefore estimate the ratio of free vs. bound fraction of H1°-GFP. Previous works have relied on an estimation of D by using the Stokes-Einstein relation and assuming a viscosity about 3-times that of water [20, 182]. In this work I shall introduce a different approach using FCS measurements to determine the diffusion coefficient. Ectopically expressed H1°-GFP is very much enriched in the nucleus where it binds specifically to chromatin. By eye and by normal intensity imaging no fluorescence from H1°-GFP is observed in the cytoplasm. Nevertheless, there is a small fraction of H1°-GFP also found in the cytoplasm at concentrations in the nanomolar range. This concentration is ideal for FCS where one observes intensity flucutations in a femtolitre volume caused by individual molecules. Since H1°-GFP is not known to have any specific binding partners in the cytoplasm one can treat it as a *bona fide* inert particle exhibiting Brownian motion only. The diffusion coefficient measured in the cytoplasm can safely be expected to be comparable to pure diffusion of the same molecule in the nucleus. Previous studies have demonstrated that the viscosity in the nucleoplasm exhibited by small molecules < 200 kD is similar to that in the cytoplasm. Therefore, I can use the D measured with FCS in the cytoplasm to estimate the free/bound ratio from D_{eff} estimated by FRAP analysis.

Histone H1° diffusive properties measured by FCS

FCS measurements were performed on H1°-GFP WT as well as mutants R47A and E62H. The two mutants mark the to extrema on the scale of effective diffusion coefficients observed with FRAP. Since all mutants have a single point mutation their molecular weight does not differ significantly from that of the WT. One can not expect to find any notable differences in their diffusion coefficients as far as free diffusion is concerned. Nevertheless, the two mutants were also tested in order to find any differences, which might possibly arise due to non-specific interactions of H1°-GFP with unknown components of the cytoplasm. My observations indicate, that is is not the case. On the scale of experimental precision no differences between WT, R47A and E62H were observed. The total number of FCS measurements performed was N=74. Among these were N=8 measurements with mutant R47A and N=16 with E62H. From the resulting average diffusion time I computed a diffusion coefficient as described in chapter 3.1.9. The average diffusion coefficient is $D = 30 \pm 1 \mu m^2/s$. Figure 4.8 shows the distribution in a box-plot. The measured value is close to the prediction using the Stokes-Einstein equation for a 48 kD construct and about three times higher viscosity of the cytoplasm compared to buffer.

Using this number to characterize free diffusion I can now estimate the *Free* fraction introduced in equation 4.1, which is the inverse of $k_{on} \cdot [binding\,sites]/k_{off} = k^*_{on}/k_{off}$ (compare also [169, 20]). The latter quantity is a good measure for the affinity of H1°-GFP to its binding sites on chromatin. Table 4.2 summarizes the findings. Evidently, the slowest diffusing mutant E62H has an affinity to chromatin of about 140% compared to wild-type. The affinity of the next two slower diffusing mutants, K82V and K59A, is roughly 50 % to that of WT, while the remaining mutants have binding affinities around 20 % of the WT.
I have successfully demonstrated that the binding behaviour of H1°-GFP and seven mutants in its globular binding domain can be analysed by FRAP. Moreover, the effective diffusion resulting from binding to chro-

A B

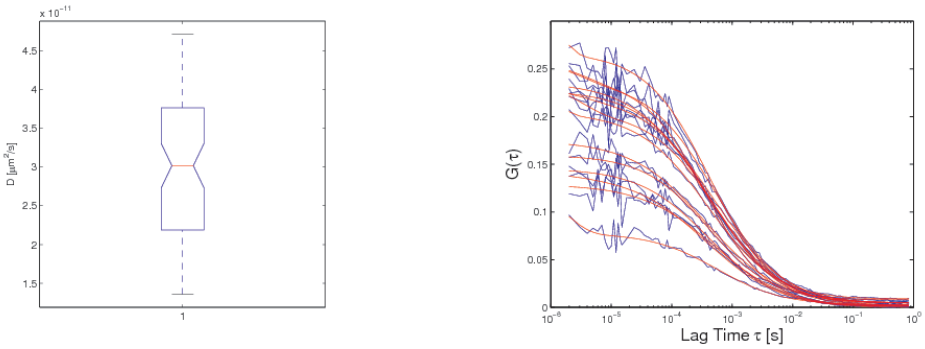

Figure 4.8: (A) Diffusion coefficient of H1°-GFP in the cytoplasm measured with FCS. The total number of measurements is N=74. They were made on three different days in independent experiments on two different confocal microscopes to reduce any systematic bias. (B) Representative FCS autocorrelation curves (N=15) of wild-type H1°-GFP (blue) with fitted with an extended 3D-Gaussian-Triplet model (red).

matin could be used to estimate free fractions as well as binding affinities. The implications will be discussed in chapter 5.1.

4.1.4 Estimation of residuals and the error function

In chapter 4.1.2 I have provided an estimation of the effective diffusion coefficient of each H1° mutant. Here it shall be assessed how reliable this estimation is. Normalized error residuals were computed and time-averaged for the same representative data sets used in chapter 4.1. The resulting residual maps represent the spatial error distribution (figure 4.9). The median residuals are very similar between all mutants and the wild-type with all being around 5% of the maximal intensity in each data set. Thus, one can expect the error in the diffusion parameters estimated to be $\geq$5%. There appears to be a tendency towards larger error residuals in the upper (non-bleached) halves of the nuclei. This is particularly apparent in mutants E62H or K97A. A possible explanation is that Tropical uses a mask for parameter estimation. In my case a mask comprising the

H1° variant	*Free* fraction [ppm]	k^*_{on}/k_{off}	k^*_{on}/k_{off} rel. to WT [%]	t_{50} [s] found in [28]
E62H	407 ± 184	2560 ± 1110	141	76
WT	553 ± 71	1810 ± 230	100	52
K82V	1120 ± 345	890 ± 270	49	63
K59A	1220 ± 500	820 ± 340	45	37
K97A	2460 ± 1780	410 ± 29	23	20
R74A	2540 ± 650	390 ± 100	22	14
H25G	2400 ± 1360	420 ± 240	23	12
R47A	3140 ± 1010	320 ± 100	18	5

Table 4.2: Summary of free fraction and affinities of WT H1°-GFP and its mutants. Effective diffusion coefficients obtained in the previous chapter are transformed into the fraction of free fraction (free/total) and the ratio k^*_{on}/k_{off}, which is a measure for the affinity of H1°-GFP to its binding sites. This affinity is expressed relative to the wild-type.

bleached half of each nucleus was used. There also appears to be a mismatch at the very edge of each nucleus in some cases (e.g. R47A). This could be due to small deviations in the masks generated for each nucleus. Overall, however, the residuals appear to be small and relatively envenly distributed. The variance of the parameters is much higher than 5% as seen from the box plot in figure 4.7. Therefore, the numerical parameter estimation appears to be a minor contributor to the overall error (compare discussion in chapter 5.1.2).

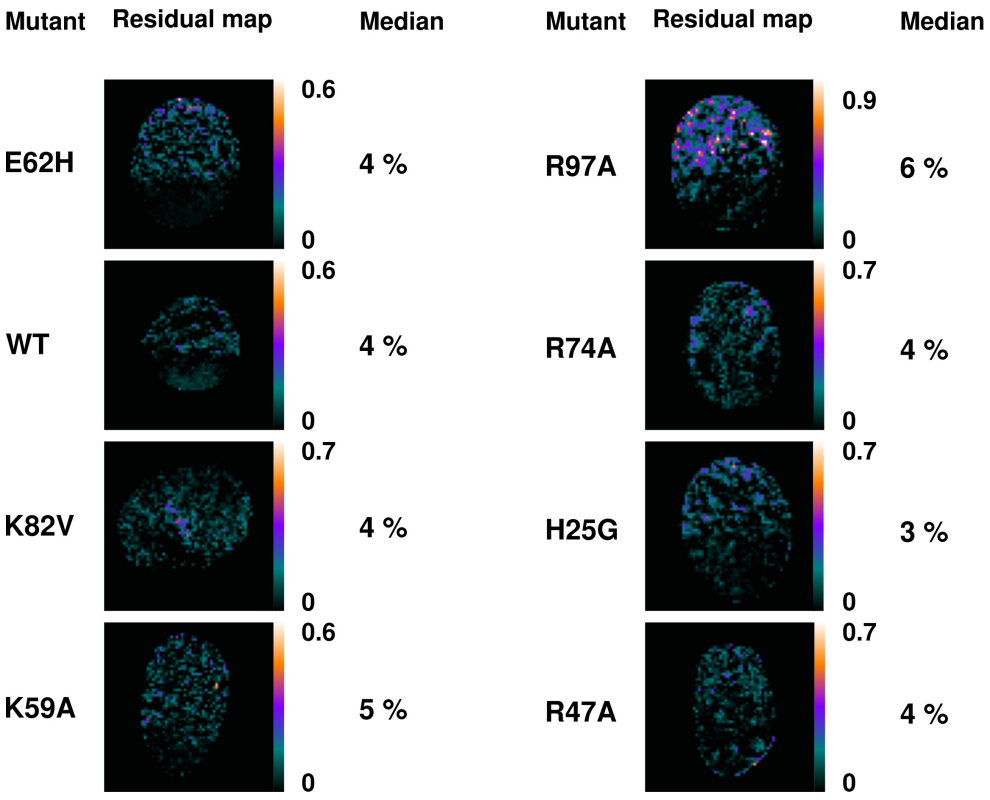

Figure 4.9: Residual maps of seven representative mutants and the WT. The residual magnitude was normalized to the maximum post-bleach value in each experimental image series. This was done for each time step individually. The residuals were averaged over time and represented as false-color images to give a spatially resolved representation of the error distribution. The median normalized residual is shown.

4.2 Dynamics of PML nuclear bodies during mitosis

Many multiprotein complexes are visible inside the nucleus as nuclear bodies. Most of these nuclear bodies tend to disassemble during mitosis and reform at the end of it. The dynamics of PML NBs has been extensively studied in interphase nuclei, where the dominant behaviour is Brownian motion and confined diffusion ([125]). Because of their size around ~1 µm NBs are a useful tool to probe not only their own dynamics but also the structure of chromatin domains and their permeability for large macromolecular assemblies. To characterize and quantitatively describe PML NB dynamics in relation to condensing chromatin during prophase through prometaphase is the subject of this section.

4.2.1 Development of an image processing workflow for quantitative motion analysis

Live cells are moving on the timescale of minutes to hours which is the timescale of interest in this study. The superposition of cell movement with movement of subnuclear particles results in a complex pattern. These two contributions need to be disentangled to facilitate motion analysis. Movement of PML NBs within cell nuclei was therefore separated from overall movement of cell nuclei by applying a rigid registration scheme. Registration was applied to the 2D maximally projected chromatin images. The resulting transformations were then applied to all z-Slices with PML NB images (for details see chapter 3.2.2 on page 60). The net result was a correction for rotational and translation movement of cell nuclei in x- and y-direction. For the first data sets counter-stained with Hoechst the chromatin channel was only available in the central plane of the nucleus. With the H2A-mCherry transfectants chromatin images were available in 3D. The same registration scheme was applied as above. Due to the wide-field

nature of the images the information on movement in axial (z-) direction was very limited which justifies the approach used.
In order to track movement of single particles with TIKAL binary image stacks are needed. A number of by-products of the imaging process and experimental artifacts need to be treated in order to achieve sufficiently high data quality. The microscopic raw data shows a considerable degree of noise from the digital camera. It was not possible to use high illumination intensities, because live cells can be damaged due to phototoxic effects. Phototoxicity was of particular importance, because of each cell up to 3000 single images were recorded to generate the necessary 4D data sets. Therefore an anisotropic diffusion filter (see chapter 3.2.3) was applied to suppress high-frequency pixel noise which would otherwise interfere with the segmentation process later on. Anisotropic diffusion filters are known to result in good noise suppression while preserving object edges and have been applied successfully to live cell imaging before (e.g. [14]). The particles are visible as an elliptical intensity distribution of roughly 3D Gaussian shape. This continuous intensity information has to be segmented to yield binary images containing only non-zero entries for each object. The geometry and size of each object should be preserved. For segmentation a global thresholding strategy was employed. The particles, however, vary considerably in size and shape, and most importantly their intensity varies roughly 10-fold. This problem is compounded by the anisotropy of wide-field microscopic images, which results in an apparent elongation of roughly spherical particles along the z-axis. As a result of this anisotropy the 3D Gaussian light distribution appears in several image planes with different brightness (figure 4.10 A shows xzy view).

Therefore, simple global thresholding with a high threshold leads to a bias towards larger particles, because smaller ones are lost. Conversely, a too low threshold would include too many noise artifacts (compare stronger noise at top and bottom z-Slices in figure 4.10 A). Noise artifacts in the outer layers are detrimental to the success of global thresholding as exemplified in 4.11 (B). Noise filtering alone can not cope with this problem

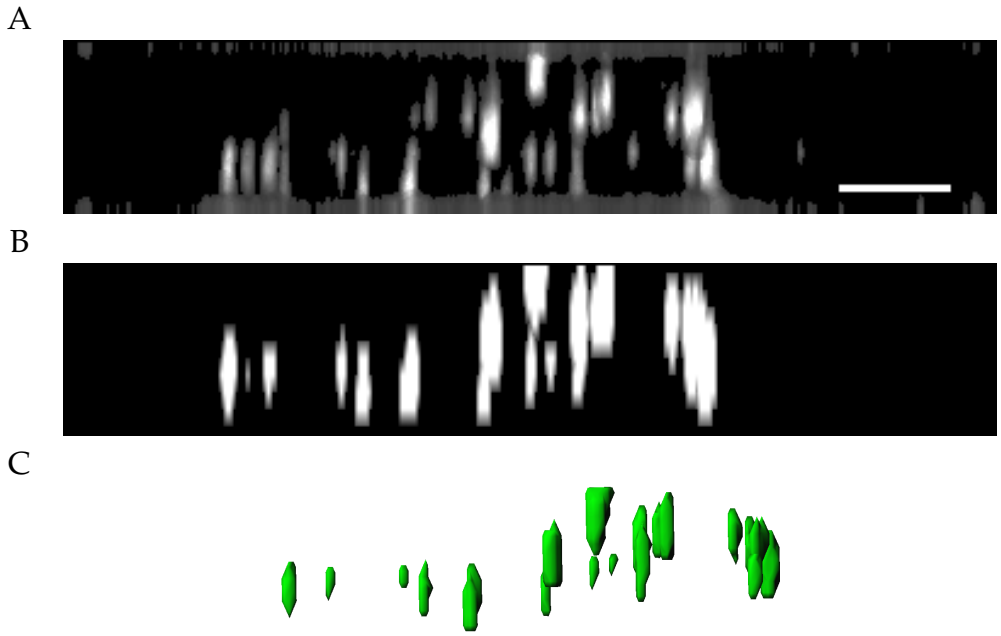

Figure 4.10: Elongation of spherical particles along the z-axis due to anisotropy of image resolution in xzy-view. Each object appears in several image planes at different intensity. A segementation scheme was developed which tolerates pixel noise, variable brightness of objects and the anisotropic point spread function of the imaging apparatus. Projection of a PML NB image stack along the x-axis (A), projection of binarized image (B), 3D-rendering in TIKAL's image viewer (C). Scale bar: 5 μm.

4.11 (C). A better result can be obtained by using entropy thresholding 4.11 (D). However, still too many artifacts remain for tracking. The solution employed here was to amplify the object edges using a filter based on the structure tensor (for details see chapter 3.2.3 on page 61). Evidently, by combining computation of the structure tensor with entropy thresholding a good result can be achieved 4.11 (E). The only drawback of this approach is, that some very small particles are lost. In the original image 4.11 (A) 25 PML NBs are visible, while the segmented image (E) contains 20 objects. The situation can be improved by compressing the particle intensities, which vary strongly after structure tensor filtering (compare figure 3.4 D and E). This was done by computing the logarithm of each pixel and applying thresholding afterward. The resulting binary image stacks were cleaned to remove remaining (rare) artifacts (for details see chapter 3.2.3 on page 61). The result contains 21 objects equivalent to 84 % of the original in good quality for tracking 4.11 (F). The example stack is also shown projected along the x-axis in figure 4.10 B. After 4D-single particle tracking (see chapter 3.2.4 on page 63), the binary images of PML NBs were further employed to read gray value information from the 3D chromatin channel visualized with H2A-mCherry. To this end, all voxels belonging to each respective PML NB were used as a mask to find the corresponding voxels in the chromatin channel. Their mean was computed and stored in time-resolved fashion (for details see chapter 3.2.5 on page 64).
An image processing workflow for registration, segmentation and extraction of gray value information was thus established making tracking data available for further analysis as discussed in the following chapters.

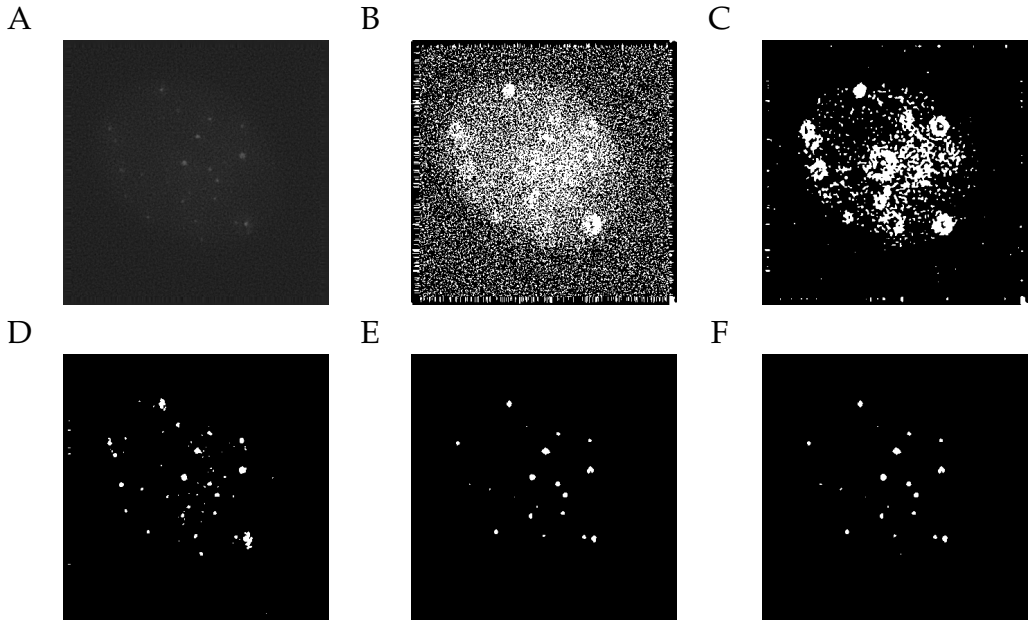

Figure 4.11: Development of segmentation workflow. Z-projections of deconvolved image stack (A), simple global thresholding (B), anisotropic diffusion filtering and simple thresholding (C), anisotropic diffusion filtering and entropy thresholding (D), anisotropic diffusion filtering, structure tensor and entropy thresholding (E), like E but with logarithm filtering. Note: For clarity the top and bottom layers in (B) and (C) were removed previous to z-projection.

4.2.2 PML NBs increase their dynamics in early mitosis

PML NBs increase their mobility and frequency of MAPP formation during early mitosis

The movement of PML NBs during prophase was quantitatively characterized by single particle tracking. All of the PML NBs were visualized by 4D imaging with wide-field optical resolution. Image stacks were acquired in the CFP and YFP channels to visualize PML NBs that were labeled by both PML-ECFP and EYFP-Sp100 proteins (see figure 4.12).

The cells were counter-stained with Hoechst dye to obtain the nuclear geometry for image registration. A single z section mid-nucleus was acquired in the Hoechst channel as a reference image to register cell movement and to follow the progression of prophase by DNA staining (compare chapter 3.2.2). During the course of imaging, multiple fusion events were observed. These fusion events were quantified by single particle tracking of PML NBs to occur in ~85% of the cells. NB fusion resulted in the formation of MAPPs and a reduction of PML NB number from 16 ± 5 bodies/ cell to 7 ± 5 bodies/cell (as counted in 21 tracking experiments), which is comparable to a previous report ([47]). The frequency of MAPP formation per cell is therefore 50% ± 25%.
EYFP-Sp100 remained co-localized with the PML-ECFP protein in MAPPs when cells went into prometaphase and did not leave MAPPs until cells entered metaphase (figure 4.12). In addition, the tracking of PML NBs using the PML-ECFP or EYFP-Sp100 signals showed no statistically significant difference (figure 4.13).

Therefore, the following 4D live cell data was only acquired in the EYFP-Sp100 channel to avoid using the shorter wavelength fluorophore, ECFP, the excitation of which could lead to stronger phototoxicity. I found that the movement of nuclear bodies is classifiable into three types, i.e. simple diffusion, constrained diffusion, and directed movement ([54, 138]). I used the coefficient of anomalous diffusion (α) for this classification. Each PML

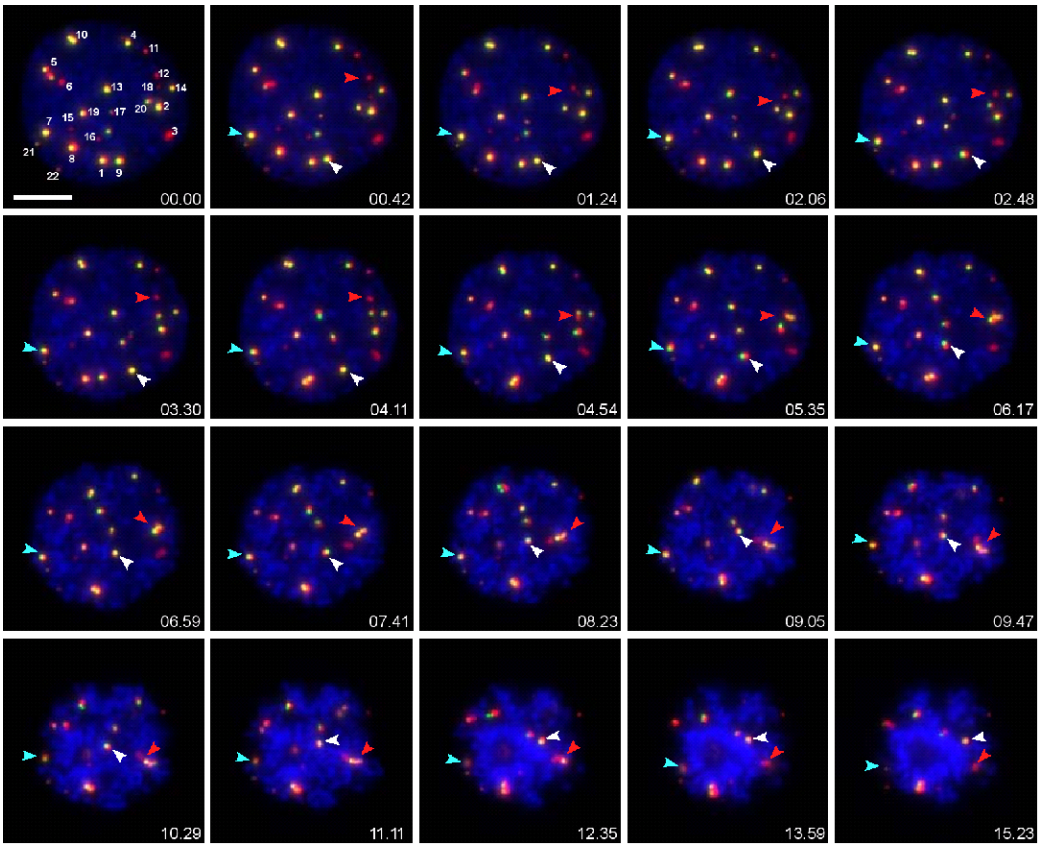

Figure 4.12: 4D tracking of PML NBs from prophase to prometaphase in living cells. Double stable cells, CpYs68, stably expressing PML-ECFP and EYFP-Sp100. Chromatin was visualized by Hoechst 33342 staining. A 7 μm z-stack of 0.5 μm steps was collected in the CFP and YFP channels every 8 sec for 26 min. One mid-nuclear z-section was recorded in the Hoechst channel per time point as the reference image for chromatin. The 3D projected still images of selected time points are shown here. Each PML NB was manually assigned a number and tracked in Tikal. Particle displacement and dynamics were analyzed. Examples of PML NBs with different motion types are indicated by colored arrowheads: Directed motion (red arrowhead), diffusive motion (white arrowhead), constrained motion (blue arrowhead). Red, pseudocolored PML-ECFP. Green, EYFP-Sp100. Blue, DNA stained by Hoechst 33342. Scale bar, 10 μm.

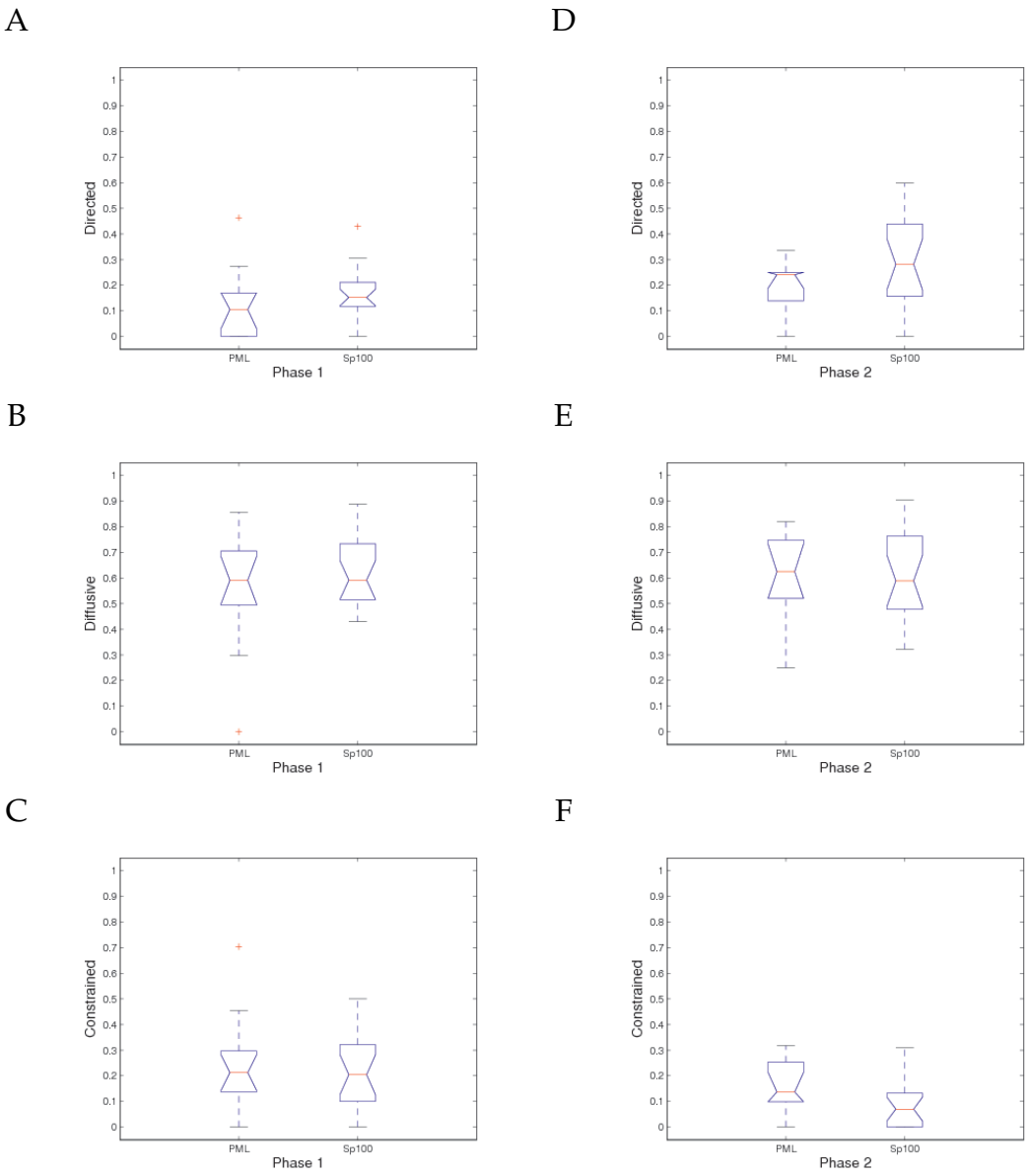

Figure 4.13: Comparison of PML NB movement types from PML-ECFP tracks and EYFP-Sp100 tracks using two-phase classification. Box-whisker plots highlight the fraction of a given population in the respective movement type. The x-axis indicates data from two different sets of cells (PML set: N =12 and Sp100 set: N = 20). The PML NBs in set 1 were tracked using the ECFP signal, while set 2 was tracked using EYFP. The red line indicates the median of each data set. The box comprises 50% of the data points. The notches represent an estimate of the uncertainty about the medians for box-to-box comparison. If the notch area overlaps between the two sets, the mean values of the two sets differ with 5% confidence level, in other words they do not differ significantly. (A) Directed movement, phase 1. (B) Diffusive movement, phase 1. (C) Constrained movement, phase 1. (D) Directed movement, phase2. (E) Diffusive movement, phase 2. (F) Constrained movement, phase 2. Although there is a low level of cell to cell variation between data sets, particularly in (F), the global distribution of each movement type is similar in both phases.

NB was assigned a unique number. A larger extent of rapid movement was observed in prophase cells compared to interphase cells. This leads to a high frequency of crossing trajectories, which poses difficulties for their continuity. Moreover, frequent fusion events (MAPP formation) often have a similar effect on object tracking. Therefore, each trajectory had to be checked and corrected manually using the inbuilt 4D image viewer in TIKAL ([14]). The mean square displacement for each track was then calculated in MATLAB and fitted to the power law $\langle x^2 \rangle = 6D\Delta t^{\alpha}$ as described in 3.2.6. The α parameter was determined using non-linear regression analysis and was used to classify movement types. Examples of each movement type are shown in figure 4.14.

An overview of the trajectory of each PML NB in a 4D image data set is shown as ball-and-stick representations, and the initial position of each PML NB is indicated by a green volume (figure 4.15). Overall, 40% of PML NBs showed directed movement in prophase as compared to 10% in interphase, and notably, often the fast moving PML NBs fused with each other to form MAPPs (figure 4.12, red arrowhead).
So far, the data demonstrates that PML NB dynamics increases during prophase. MAPP formation also increases during prophase, most likely because NBs collide more often as a result of their higher mobility.

Individual PML NBs switch their movement types during early mitosis

While tracking of PML NBs, I noticed that many of these bodies changed their movement type over time as indicated by the α coefficient. This results in a multi-phasic pattern, which is not usually observed in an interphase cell. Examples of the complexity of NB dynamics during early mitosis are given in figure 4.16.

The displacement is directly proportional to velocity. Particles increasing their displacement, particles maintaining their displacement as well

A

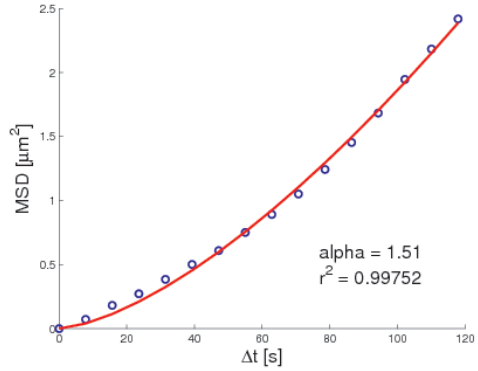

B

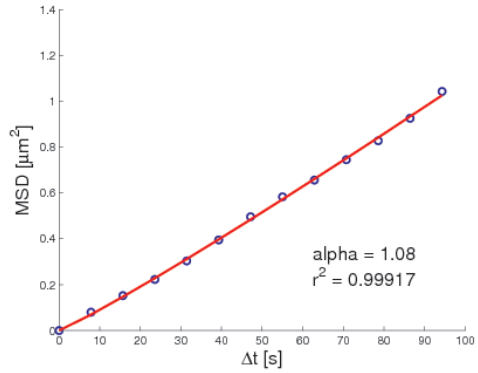

C

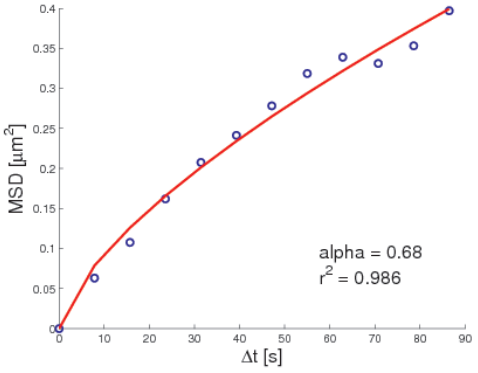

Figure 4.14: Three different movement types plotted over the first 25% of all time intervals in each data set. Movement types are directed motion (A), normal diffusion (B) and confined diffusion (C). Fitted alpha values are given as well as the Pearson correlation coefficient of the fit (r^2). Blue circles: Experimental data, red lines: fit

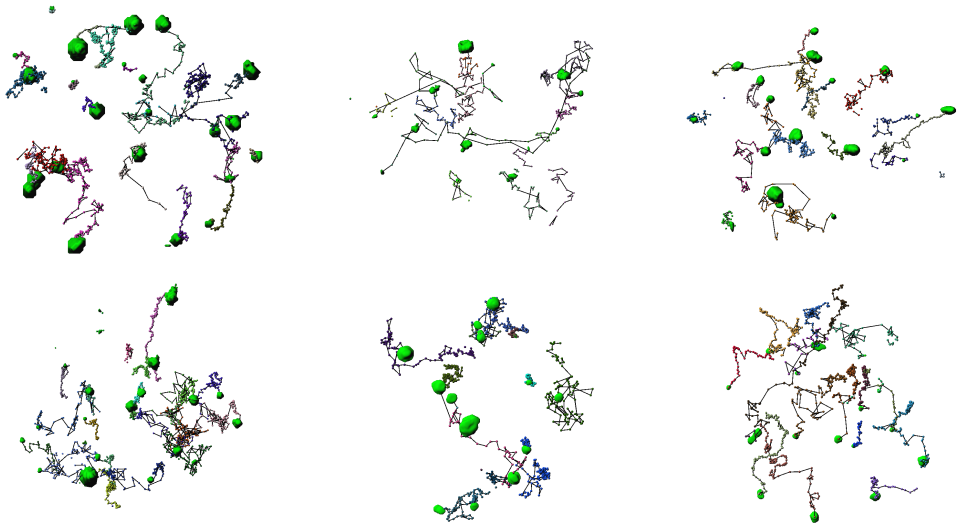

Figure 4.15: Six typical prophase tracking experiments. PML NBs are visualized as isosurface renderings in green, particle trajectories are shown as ball-and-stick representations. Clearly a large proportion of directed and diffusive motion is visible (extended tracks and random walk-like tracks, respectively). Confined motion (localized motion, compact tracks) on the other hand is much more rare in prophase.

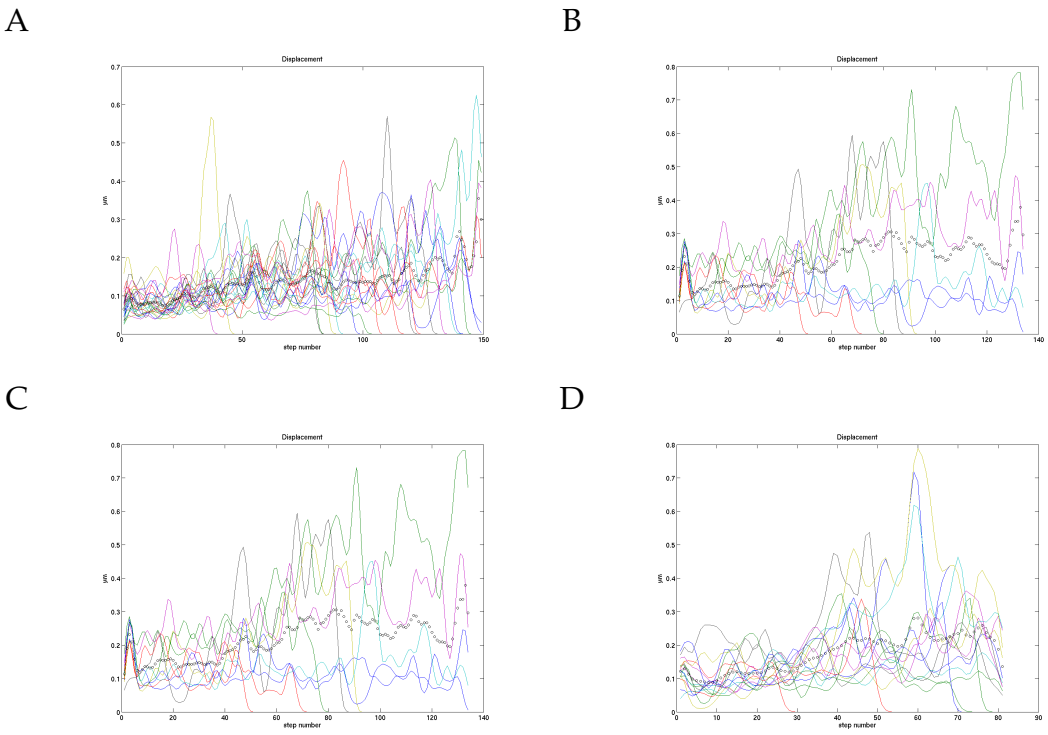

Figure 4.16: Four selected displacement plots reveal the increase of particle mobility during early mitosis. Particle displacement is directly proportional to their velocity. In all four examples there are at least three different behaviours: NBs increasing their displacements and staying on a high level until the end of the observation period, NBs maintaining their velocity on the initial level and NBs switching between fast and slow movement.

as those particles switching between different displacements become evident. If the MSD is calculated for such complex trajectories, the displacements become averaged resulting in a wrong classification of the corresponding particle. In order to obtain a better classification of movement types, I sub-divided the trajectories into two phases at the transition of prophase to prometaphase when nuclear envelope breakdown (NEBD) occurred. A diffuse pool of soluble EYFP-Sp100 can be observed in interphase nuclei. This EYFP-Sp100 fractionl dissipates from the nucleoplasm into the cytoplasm during NEBD. I determined the time point of NEBD visually based on the dissipation of EYFP signal from the nucleus. With this bi-phasic model I was now able to further dissect the global change of PML NB dynamics. Phase 1 begins from time zero (during early prophase), the beginning of data collection, to the time I observed the release of Sp100 into the cytoplasm. Phase 2 starts from the time of Sp100 dissipation to the end of data collection. Typically, this was during late prophase. The Hoechst chromatin counter stain which was first used for defining nuclear geometry and registration was not suitable to obtain full z-stacks at each time step. As an alternative to Hoechst which is excited at the more phototoxic 405 nm I used an H2A-mCherry label excitable at a wavelength of 587 nm. In subsequent live cell experiments, I transiently expressed an H2A-mCherry fusion protein to visualize chromatin and to follow the progress of prophase during the course of imaging. 4D live cell data sets were then acquired in both the YFP and mCherry channels from early prophase to late prometaphase with 8 second time intervals and 0.5 μm z steps. The motion of PML NBs in 10 interphase cells and 20 prophase cells were thus tracked and categorized into three types: diffusive movement (Brownian motion), directed movement, and constrained diffusion.

As summarized in figure 4.17, the proportions represent the PML NB population exhibiting the respective movement type in each cell. For this analysis 10 interphase control cells were compared to 20 prophase experiments[1]. The population of PML NBs exhibiting diffusive motion re-

[1]The actual number of analysed prophase cells was 38. However, the earliest data sets

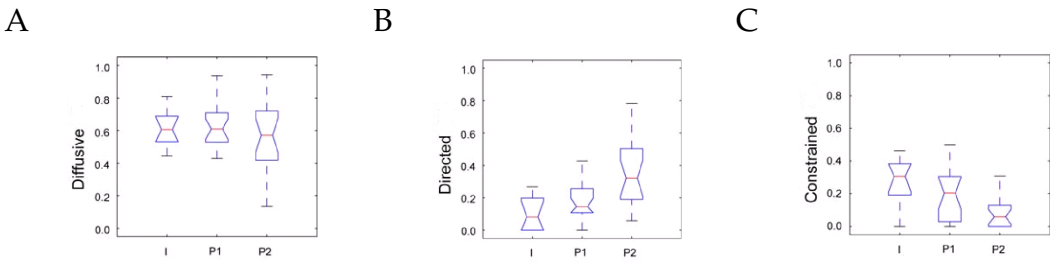

Figure 4.17: Comparison of PML NB movement types in interphase and prophase. The box-whisker plots summarize the movement types of PML NBs from interphase cells (N = 10) and prophase cells (N = 20). The y-axis indicates the proportion of PML NB population that exhibits the respective certain movement types and the x-axis indicates the data from different phases, interphase (I), phase 1 of prophase (P1), phase 2 of prophase (P2). The red line indicates the median of each data set. The box represents 50% of the data points in each data set. The notches represent an estimate of the uncertainty about the medians for box-to-box comparison. If the notched area overlaps between the two sets, the mean values of the two sets differ with 5% confidence level, in other words they do not differ significantly. (A) Diffusive movement, (B) Directed motion, (C) Constrained diffusion.

mained constant and had medians about 60% during both interphase and prophase. In the interphase cells, a median of 10% of the PML NBs exhibited directed movement, which is in agreement with a previous study ([125]). In contrast to interphase, in phase 1 of prophase, the directed movement of PML NBs increased to a median of 18%. During phase 2, the median percentage of directed 12 PML NBs further increased from 18% to 30%, while the median of the PML NB population showing constrained movement decreased from 20% to 10%. These movement type shifts of the PML NB population are significant as demonstrated graphically by a box-whisker plot as well as by ANOVA analysis with $p < 0.01$ (see chapter 3.2.6). The increase of directed PML NBs in phase 2 was contributed to mostly by the constrained PML NBs. By using this bi-phasic model, I

had been imaged in 2D time series and the following ones in 3D time series, but with chromatin only in 2D (Hoechst staining). A 3D chromatin channel was used later on for extraction of chromatin density. Therefore, 18 cells were not included in this figure. PML NBs showed a comparable global increase of mobility in phase 2 of prophase in those experiments.

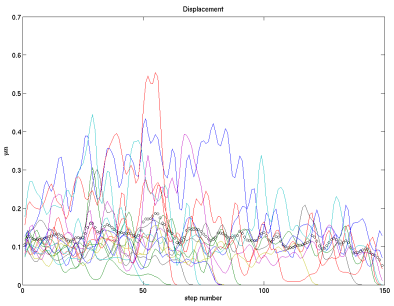

Figure 4.18: Displacement plot of prophase cell. Some NBs go through an transitional phase of fast movement and return to a slower movement later on, while others maintain their state of mobility as exemplified by this figure. This lends an additional complexity to quantitative analysis of single particle trajectories. Both, an average MSD per track as well as the bi-phasic model may represent an oversimplification. Therefore, a more detailed analysis scheme was devised which takes arbitrary movement type changes of individual particles into account.

demonstrated that PML NBs exhibited a global increase in directed movement and a global decrease of constrained movement during early mitosis.

4.2.3 Implementation and validation of an automatic detection scheme for changes in particle mobility

I have provided evidence that PML NBs increase their mobility a lot during early mitosis. I also were able to show, that this increase was statistically significant. Nevertheless, the inherent variance of the bi-phasic classification scheme is considerable. The reason for this is, that the the bi-phasic model fits well in some cases (as demonstrated for the accelerating particles in the displacement plots in figure 4.16) while it is a rather poor approximation of other cells (figure 4.18). Evidently, the notion of a global increase in particle mobility taking place for all particles synchronously may be an oversimplification.

Moreover, estimating the diffusion coefficient over the entire trajectory renders only an average value. Clearly, a more detailed description of movement type switching on a per-particle basis would help to elucidate NB's dynamic behaviour. Particularly, a time-resolved D and α parameter would be of interest. However, finding such mobility transitions manually in hundreds of trajectories is both time-consuming and potentially biased. Thus, an automated algorithm is needed to detect mobility transitions in 3D trajectories. Since NB mobility was described as different types of diffusion the use of the diffusion constant D to find mobility changes seems like an obvious choice. A model-free approach based on a maximum-likelihood estimator of D was published ([189, 123]). Its implementation and adaptation to my needs shall be described in this section.

The MLE approach reliably predicts sudden changes in diffusive mobility

In order to validate the utility of this approach 500 random walks were simulated with 500 time steps each (for details see chapter 3.2.7). A plot of these random trajectories is given in figure 4.19 A. The diffusion coefficient was set to 1, likewise the coefficient of anomalous diffusion.

The displacement of their trajectories shows no statistical bias indicating that they are indeed random walks (figure 4.19 B). To test the applicability of the MLE to the estimation of the diffusion coefficient the MLE of the simulated displacements was calculated as described in chapter 3.2.7. The histogram (figure 4.20, red) shows a narrow distribution with a peak at D=1, while the histogram based on the MSD curve fitting approach is both wide and its maximum far off. As has been shown by Montiel et al. ([123]) D values estimated by curve fitting to the MSD depend on the time lag used for calculation of the MSD. The longer the time lag the more inaccurate estimated D's are due to noise intrinsic to the data. This underlines that the MLE approach is superior to use of the MSD. Since the

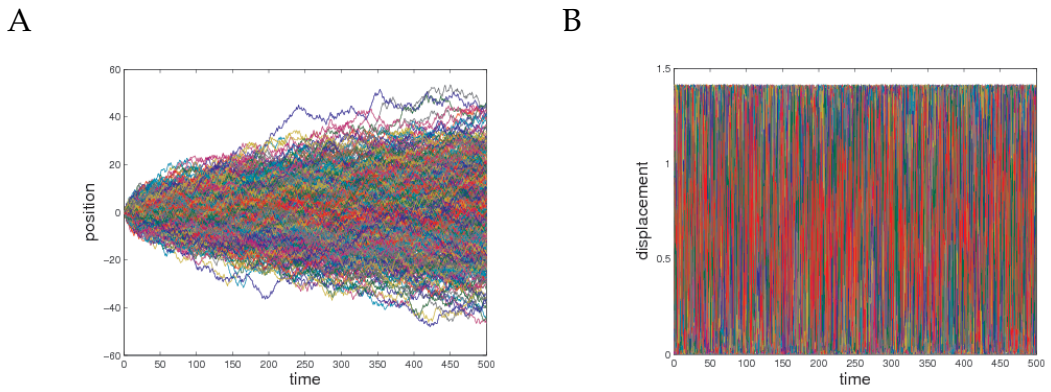

Figure 4.19: Simulated random walks (N=500) with D = 1, alpha = 1. (A) Position vs. time. The spreading of positions appears normally distributed as expected for free diffusion. (B) Displacements vs. time reveal that the displacement of the overall population is unbiased and equal to $\sqrt{2}$. Thus, the simulation produces true random walks in the sense of Brownian motion. Such simulations are used in the following as raw material for the prediction of abrupt changes in D.

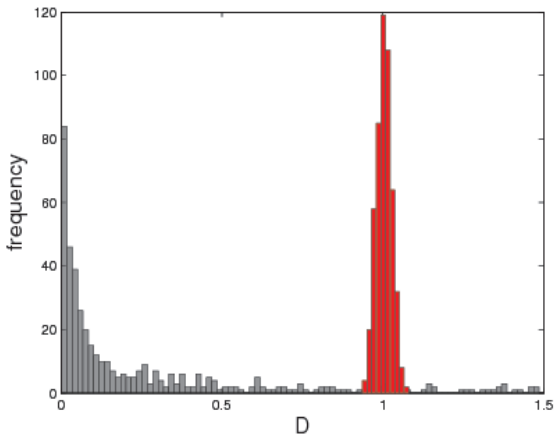

Figure 4.20: Histogram of estimated values for the diffusion coefficient D obtained using curve fitting to the MSD (gray) or the MLE approach (red). The distribution of estimated D's using the MLE approach is narrow and normally distributed. In contrast, the D's estimated using curve fitting to MSD plots is strongly biased. This demonstrates the utility of the MLE approach.

MLE approach seems to be reliable for the estimation of D I have investigated its applicability to detect fluctuations of D in a random trajectory. To this end two random walks were calculated, one with D=1 the other with D=10. The start position of each trajectory in the latter was set to the end position of the corresponding track in the former. Thus, the first half of each trajectory represents a random walk with D=1 and the second half one with D=10. This data is now used to detect mobility changes using the MLE approach. The strategy is outlined here (for details see 3.2.7 and 3.2.7):

- The point in time when the mobility of a particle has changed will be referred to as a "break point" in the following. The break point is found in a trajectory by computing its log-likelihood ratio function. The maximum of this function marks a potential break point.
- A statistical test is used to determine false-positive break points with a predetermined confidence level. If a break point has been identified, the trajectory is partitioned into two sub-trajectories and the process is repeated recursively until the sub-trajectories become too short or no new break point is detected and the algorithm terminates.

Diffusive transitions are found in the bi-phasic example reliably as is shown in fig. 4.2.3. Out of 500 break points 466 have been predicted correctly, equivalent to 93% at a confidence level of 95%. A diffusive transition of $D_2/D_1 = 10$ is therefore identifiable. The prediction works equally well with the same data at a confidence level of 69% (data not shown).

The prediction power and precision of the MLE approach

As was shown by [123] there are three parameters, which strongly influence the prediction power of the MLE approach. These are the ratio of the diffusion coefficients D_2/D_1, the length of the (sub-)trajectories and the desired confidence level. The implications can be summarized as follows:

A B

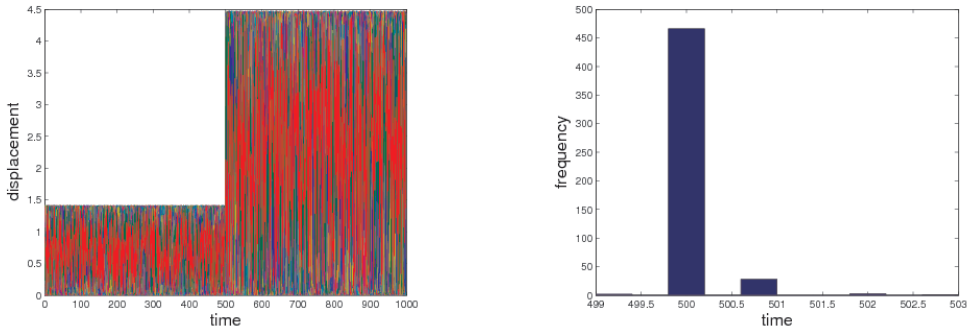

The MLE approach allows the automated detection of break points in a trajectory. A simulated bi-phasic random walk was analysed for break points. 93 % of all break points in the simulated data were predicted correctly at 95% confidence. (A) Displacement plot over time of mixed trajectory with D = 1 (time steps 1-500) and D = 10 (time steps 501-999). (B) Diffusive transitions ("break points") detected by the MLE approach at 95% confidence level. The number of detected break points is plotted over the time point of the transition.

- For tracks of length 200 a D_2/D_1ratio < 1.3 is not feasible, a D_2/D_1 ratio ~2 is possible, but difficult at confidence levels > 69% and a D_2/D_1ratio > 4 works well at all confidence levels (s. a. 6.2).
- At a track length of 100 a D_2/D_1 ratio of ~ 4 is possible, while tracks shorter than 60 seem not feasible (s. a. 6.3).

As is suggested by above conditions, a D_2/D_1 ratio ~2 poses a case which can be difficult to predict reliably with high confidence. To test the influence of the confidence level on the prediction power 200 random trajectories of length 400 time points have been calculated with a jump from D=2 to D=1 at time 200. The length of the resulting sub-tracks can be expected to be sufficient. The confidence levels tested were 69%, 80%, 90%, 95% and 99%. The higher the confidence level the more break points are false-negative and the more precise the estimate is. False-negative break points are expressed as the percentage of trajectories whose break point was missed. The precision of the prediction is derived as the deviation from the known break point at t=200 (see chapter 3.2.8). The results are

confidence level [%]	69	80	90	95	99	95 (interpolated)
false-negative break points [%]	0	2.5	44	96	100	5
deviation from known break point at t=200	43.4	11.3	7.7	2.1	0	14.0161

Table 4.3: Prediction power of the MLE approach as a function of confidence level. Increasing confidence levels lead to a higher number of false-negative break points and a higher precision. A good compromise was achieved by setting the confidence level to 95 % and using linear interpolation of trajectories.

summarized in table 4.2.3. At confidence levels of 69% as well as 80% the percentage of false-negatives is low, but the prediction is rather imprecise (e.g. at confidence of 69% the statistical deviation from 200 is 43.4). On the other hand, already at confidence level 90% break points were missed in about 44% of all tracks. At 95% and 100% confidence almost all of the break points are not detected. This would greatly impede the utility of the MLE approach, since a high temporal precision of the prediction was desirable, in particular, because the temporal order of event during mitosis was to be addressed (see chapter 4.2.8).
Another parameter with strong influence on the prediction power is the length of the trajectory. The length of a given trajectory can be increased by interpolating between consecutive time points (see chapter 3.2.9). In this example, a moderate interpolation to 3 times the original length of the trajectory helped to reduce the number of false-negatives from 96% to 5% (see table 4.2.3 rightmost column). This was, however, achieved at the expense of precision. Thus, the prediction power at 95% confidence with moderate interpolation is comparable to that at 80% confidence. .

There was no *ab initio* knowledge about the D_2/D_1ratio in trajectories of PML NBs. It can not be assumed that the ratio is always larger than 2 or even 4. Their length varied from 80 - 200, typically lying around 150 time points. Moreover, as particles change their mobility during prophase the resulting sub-tracks would be even shorter. As outlined above, these

are difficult conditions, in particular with regard to track length. It seems therefore necessary to increase the number of points in order to achieve a satisfactory prediction power. To test the effect of interpolation on short trajectories a further test scenario was developed for a detailed assessment. This time 5 sub-tracks were combined with D = 2, 1, 1.7, 2.21, 0.5525, respectively. This results in a $D_2/D_1$of 2, 1, 1.7, 1.3 and 4. These values represent both challenging (1.3, 1.7) as well as simple (4) break points according to the criteria discussed above.

Figure 4.2.3 (A) shows such a trajectory and sub-tracks with length 50 time points. This time a rather poor prediction is expected if no interpolation is applied. The corresponding displacements are given in figure 4.2.3 (B). The transitions in diffusion coefficient have been chosen as to give a reasonable scaling of the graph. Figures 4.2.3 C-E then show histograms of the predicted break points of the same trajectory as in (A). The interpolation depth was 10x, 15x and 20x of the original length, respectively. The prediction was carried out at a confidence level of 95%. It must be noted, that the MLE approach was not capable of predicting any break points without interpolation. This is in agreement with the results obtained for sub-tracks of length 200 time steps (table 4.2.3). In the example using length 200 for the sub-tracks a moderate interpolation reduced the number of false negatives to 5%. In the example with sub-tracks of length 50 the improvement achievable by interpolation was assessed qualitatively. At 10x interpolation a transition ratio of 2 (at time 50) as well as a ratio of 4 (at time 200) were detected reliably while the smaller transition ratios of 1.7 and 1.3 were below background. At 15x interpolation the transition ratio 1.7 was detected. At 20x interpolation the smallest transition ratio 1.3 is visible as a small, but wide peak. At this level of interpolation the width of neighboring peaks leads to considerable overlap, which limits the prediction of small transition ratios <= 1.3. At 50x interpolation and above this overlap becomes dominant (data not shown) and represents the upper limit to interpolation. Taken together, it is possible to predict transition ratios down to 1.7 at confidence level 95% in trajectories with sub-tracks of length 50.

This length which was typically encountered in PML NB single particle tracking in this work. A D_2/D_1 transition ratio of 1.7 is to be considered the practical limit to the MLE approach with data similar to what was available from the PML NB tracking.

The MLE approach was now applied to a real data set obtained from one cell. PML NBs were labelled using EYFP-Sp100 and chromatin was visualized by H2A-mCherry. 17 PML NBs were identified and tracked. The trajectories were interpolated to 20x their original length and break points were predicted at 95% confidence level. In total 50 break points were identified and a histogram is shown in figure 4.22. The histogram shows 3 peaks corresponding to time points where many NBs change their diffusivity. The concept of multiple (sub-)phases during prophase through prometaphase can thus be studied by PML NB mobility.

The information gained by predicting break points can be utilized for further data analysis. In particular, data between two consecutive break points can be considered a sub-trajectory. A sub-trajectory comprises such a part of a trajectory whose changes in diffusive mobility are below the detection limit of the MLE approach. In my case, as shown above, the ratio of diffusion coefficients D_1/D_2 is larger than 1.7 and smaller than $1/1.7 \sim 0.6$. Therefore, a sub-trajectory represents a time interval during which its respective PML NB maintains its current mobility. It is now possible to compute quantitative parameters describing a particle's mobility during this time interval resulting in a "pseudo-average" parameter over this time interval. Next to the diffusion coefficient itself, the α parameter indicating deviations from free diffusion is of interest. The diffusive state of an NB in a sub-trajectory can be related to particle velocity and chromatin density. The former can be computed directly from the particle displacement. Chromatin density is obtained by computing the mean intensity of all voxels in the chromatin channel at the position of a PML NB (for details see chapter 3.2.5). Time-resolved chromatin density allows conclusions about the state of an NB with regard to attachment/detachment to/from chromatin. It has been previously described ([125, 14, 71]) that

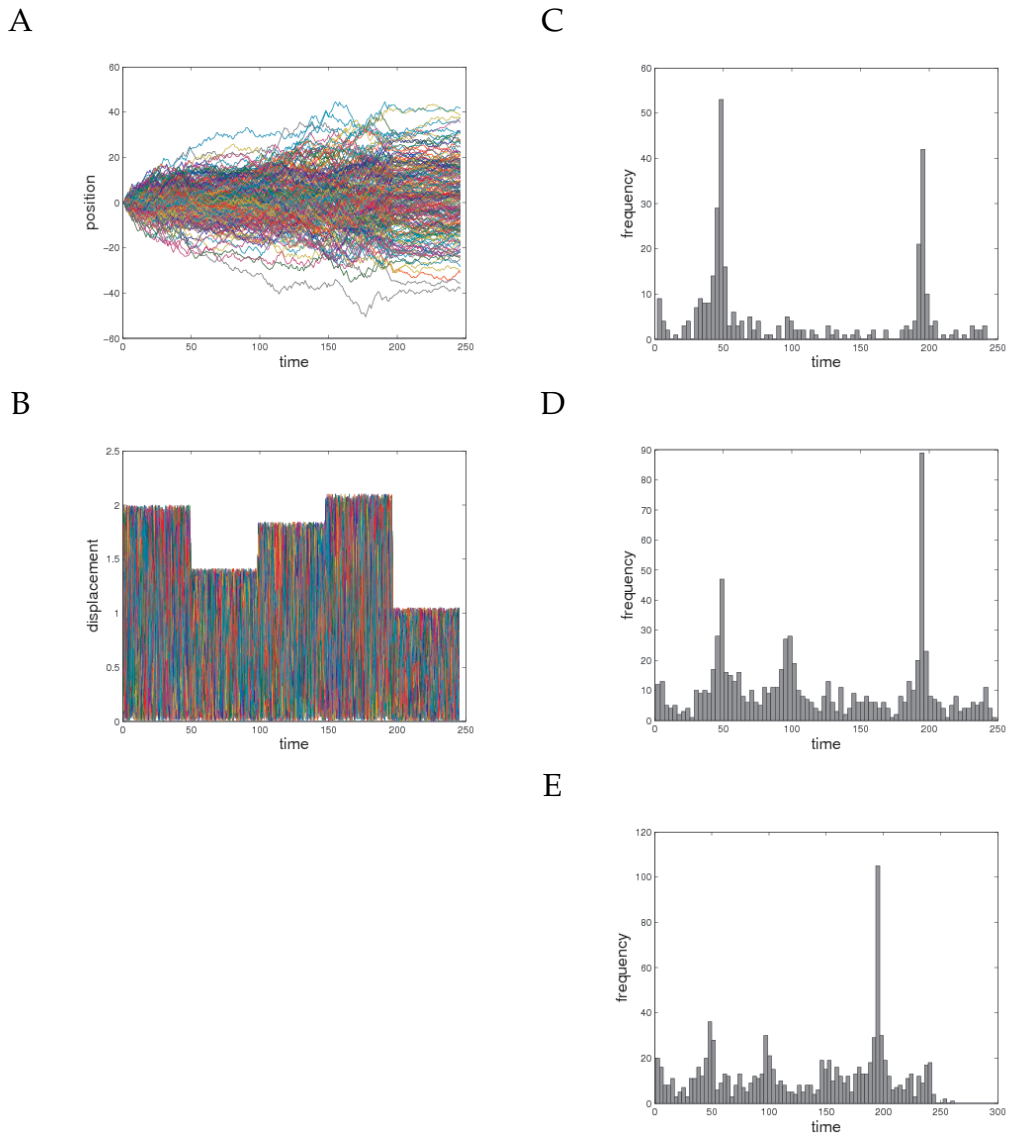

Figure 4.21: Test scenario consisting of 5 simulated sub-trajectories of 50 time steps each with D=2, 1, 1.7, 2.21, 0.5525, respectively. Different levels of interpolation (10x, 15x, 20x) were compared to find the right balance between increasing the prediction power versus the accuracy of the MLE approach. The maximum interpolation of 20x allows detection of the smaller transitions. A D_2/D_1 ratio appears to be the practical limit of the automated break point detection. (A) Plot of 200 simulated trajectories. (B) Displacement of 200 trajectories. The ratio $D_2/D_1$is equivalent to 2, 1, 1.7, 1.3 and 4. (C) Histogram of all predicted break points using interpolation to 10x the original length. (D) Histogram of all predicted break points using interpolation to 15x the original length. (E) Histogram of all predicted break points using interpolation to 20x the original length.

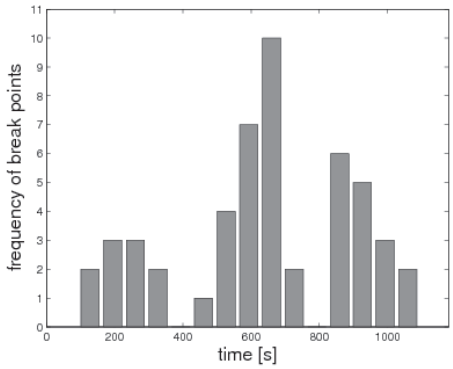

Figure 4.22: Application of the automated prediction of break points by the MLE approach. Break points were predicted for trajectories in a cell nucleus for 17 PML NBs. Histogram over break points shows 3 peaks where many NBs change their diffusive mobility.

nuclear particles can be found in states of obstructed diffusion, free diffusion or directed motion. The power of combining the time-resolved α parameter with chromatin density is that there are now two pieces of evidence allowing to dissect the state of a particle. For example a particle with a high α parameter (i.e. directed motion) and high chromatin density is likely to be pulled by condensing chromatin, while a particle with low alpha and low chromatin density appears to be confined to a chromatin corral ([71]). Table 4.4summarizes some of the possible biological interpretations. It must be noted, that the available parameters do not allow the analysis of mechanistic details behind attachment/detachment or flow on a molecular level.

It should also be noted, that a lot of information of considerable complexity is extracted from the image data. Effectively, a multi-dimensional image data set with 5 dimensions (i.e. 3 spacial coordinates, time and channel information) is processed to obtain another multi-dimensional data set with another 5 dimensions (D, α, velocity, chromatin density, break points) each of which is a function of time. Figure 4.23 exemplifies such a multi-dimensional data set by showing D, α, velocity and chromatin density over time for a selected cell. The biological implications will be discussed in the

	PARAMETER COMBINATION	BIOLOGICAL INTERPRETATION
1	αhigh, chromatin density high	particle attached to and pulled by condensing chromatin
2	αhigh, chromatin density low	particle moved by flow in the nuclear matrix
3	αmedium, chromatin density high	particle attached to chromatin domain which moves diffusively
4	αmedium, chromatin density low	free diffusion
5	αlow, chromatin density high	particle attached to immobile chromatin
6	αlow, chromatin density low	particle confined in chromatin corral

Table 4.4: Exemplary biological interpretation of alpha parameter and chromatin density. Parameter combinations on the left represent a simple classification scheme. Classification into high/medium/low for alpha conceptually follows the classification used in chapter 4.2.2. The classification of chromatin density is less straightforward and serves here only to illustrate the concept.

following chapters.

4.2.4 Increased PML NB dynamics is revealed by a shift from obstructed diffusion towards directed motion

I applied the MLE approach to predict break points as described in chapter 4.2.3 to 10 interphase cells 20 prophase cells double-labeled with Sp100-YFP and H2A-mCherry. According to the predicted break points the diffusion coefficient D and the coefficient of anomalous diffusion α were estimated for each trajectory. Additionally, the particle velocities over time were computed directly from the displacement (Euclidean distance between consecutive time points). In total 160 interphase trajectories and 533 prophase trajectories were processed in this way. For a global analysis these time-resolved values were histogrammed as summarized in figure 4.24. This allows a quantitative comparison between PML NB mobility during interphase and prophase, respectively. Clearly in all three histograms, the peak of prophase tracks (blue) expanded to the right from the peak of interphase tracks (red). This indicates that prophase cells have more PML NBs showing an increased diffusion coefficient and high α value as compared to interphase cells. In addition, prophase cells have more PML NBs exhibiting larger velocities than interphase cells. The maximum of the distribution of D shifts from 0.001 $\mu m/s$ to 0.005 $\mu m/s$, the maximum of the velocity distribution shifts from 0.7 $\mu m/min$ to 1.4 $\mu m/min$ in prophase. I can conclude that PML NBs change their dynamics during prophase dramatically. The α parameter reveals that the increase does not only occur due to large scale displacements, but that PML NB mobility changes qualitatively. During interphase PML NB mobility is dominated by obstructed diffusion as shown in figure 4.24 B (red) with a median at $\alpha \sim 0.6$ indicative of subdiffusion. In the corresponding histogram for prophase mobility, figure 4.24 B (blue), I observed 2 peaks indicative of a slow population of NBs dominated by diffusive mobility $\alpha \sim 1$ and a fast population $\alpha \sim 2$ dominated by directed motion. The change in PML

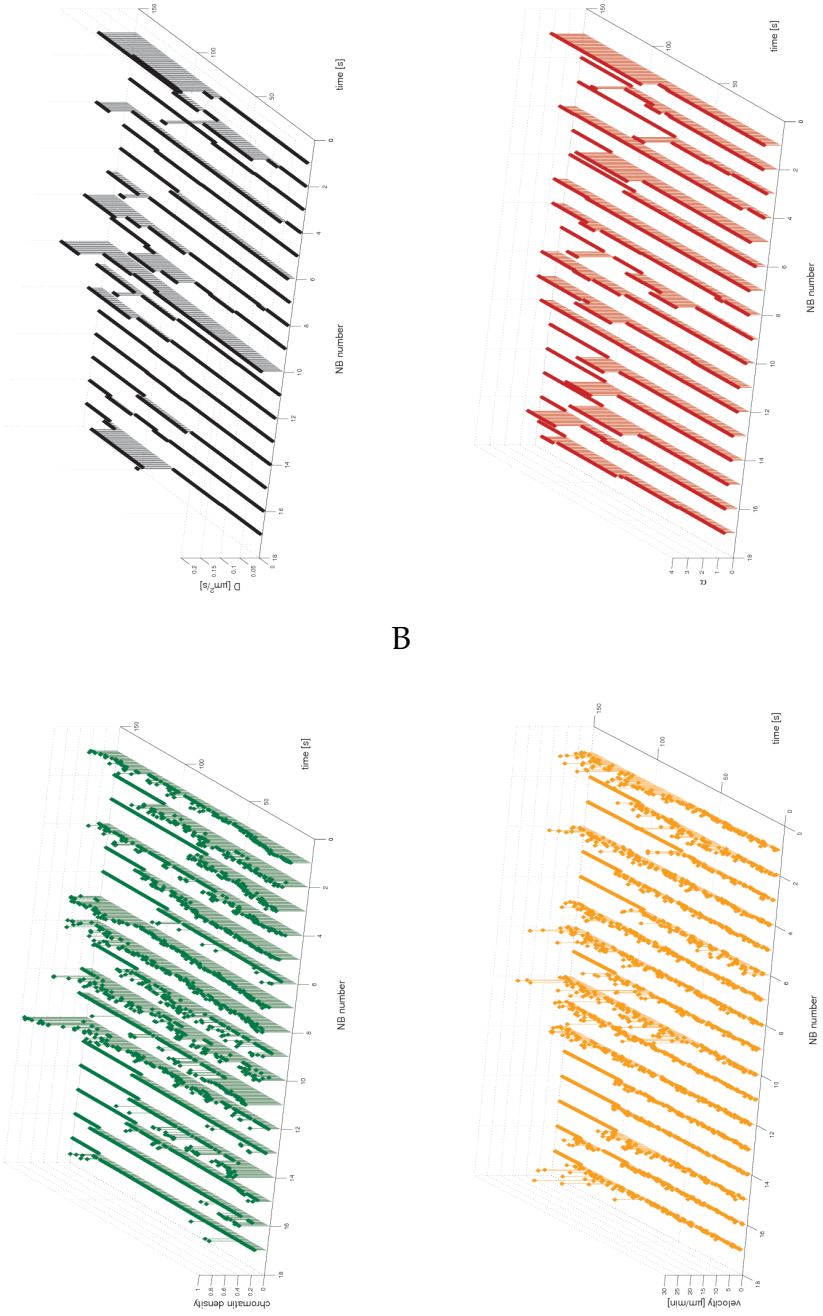

Figure 4.23: Break points were calculated in a cell for 17 PML NBs. Based on these break points each trajectory was subdivided into sub-trajectories (time points between two break points). For each sub-trajectory 4 parameters were computed: The diffusion coefficient (A), the coefficient of anomalous diffusion (B). For reference, the relative chromatin density based on image gray values (C) and particle velocity (D) are given.

NB movement types may be explained by one or more of the following possibilities, which are a subset of the possible interpretations suggested in table 4.4. First, PML NBs may initially be constrained in the crowded nuclear environment. Chromatin condensation creates additional interchromatin space in phase 2, such that the confinement by chromatin is reduced. Therfore, PML NB mobility increases. The second possibility is that material exchange between the nucleoplasm and the cytoplasm during NEBD may generate a physical flow that may force PML NBs to move passively. Lastly, PML NBs may lose their constraints by detaching from chromatin during prophase, and therefore increase their overall dynamics. Thus, experiments were designed to distinguish between these three possibilities.

4.2.5 PML NB mobility increase is not caused by chromatin condensation

As outlined in chapter 4.2.4 there are several possible mechanisms behind the increase in PML NB mobility that were found. These possibilities are tested here. First, I wanted to determine if the increase of interchromatin space can result in increased dynamic movement of PML NBs. Premature chromosome condensation (PCC) can be induced by using chemical inhibitors of type 1 and type 2A protein phosphatases (PP1 and PP2A), such as calyculin A (CA) and okadaic acid (OA), to mimic mitotic condensation of chromosomes ([9]). It has been previously shown that CA and OA treatments efficiently induce PCC, usually within an hour of treatment, in over 20% of the cells tested ([51]). CA induced PCC in the CpYs68 double stable cell line ought to help in determining if PML NB dynamics is affected by an increase of interchromatin space. CpYs68 cells, transiently transfected with H2A-mCherry (green LUT), were imaged 30 min after 40 nM CA treatment. 4D live cell image stacks with 0.5 μm steps were collected in the mCherry and CFP channels every 10 sec for 8 min. As a result of CA treatment, PML NBs did not change their relative position, and PML

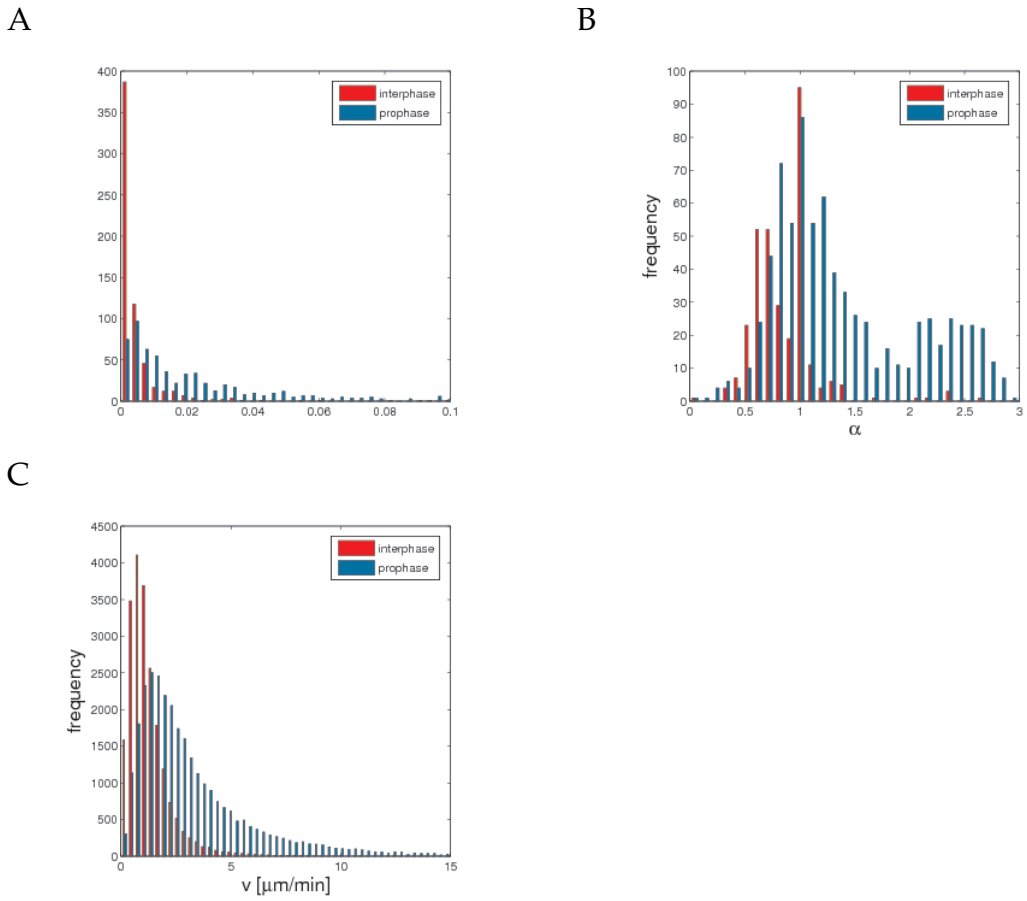

Figure 4.24: Comparison between PML NB mobility during interphase and prophase. Trajectories from 10 interphase (red) and 20 prophase cells (blue) were analysed using the MLE approach for a prediction of changes in diffusive mobility. Histograms of the diffusion coefficient (A), alpha coefficient (B) and velocity (C) were plotted.

NBs displayed limited movement upon chromosome condensation (figure 4.25, arrowheads).

When applying the MLE approach to calyculin A data no break points where detected, as shown in the plots of α and D in figure 4.26 A-D. Velocities remained mostly constant throughout the imaging period despite statistical fluctuation (figure 4.26).

It is clear that the dynamic behavior of PML NBs in CA treated cells is dramatically different from that in normal prophase cells. Few PML NB fusion events were observed, and no high velocity of PML NBs occurred. Therefore, increased interchromatin space does not appear to be the driving force of increased PML NB movement. This notion further supports the possibility that formation of MAPPs requires the increased dynamics of PML NBs. In addition, PML NBs remained closely associated with chromatin after CA treatment, and their limited movement was concurrent with the movement of condensed chromatin. Therefore, PML NBs do not move freely within the increased interchromatin space upon the induction of PCC by CA.

4.2.6 The increase of PML NB dynamics during prophase correlates with molecular events

An alternative explanation for the increase of directed PML NB movement during prophase is the physical flow between the nucleoplasm and the cytoplasm. Such changes upon nuclear envelope breakdown (NEBD) may be the driving force of PML NB movement in prometaphase. As previously mentioned, the time of Sp100 dissipation from the nuclei corresponds to the time of NEBD, and was therefore used to roughly divide the prophase data sets in the bi-phasic analysis. A more precise timing of NEBD and its temporal relationship with the increase of PML NB dynamics was provided by introducing a DNA construct of 2 copies of HcRed

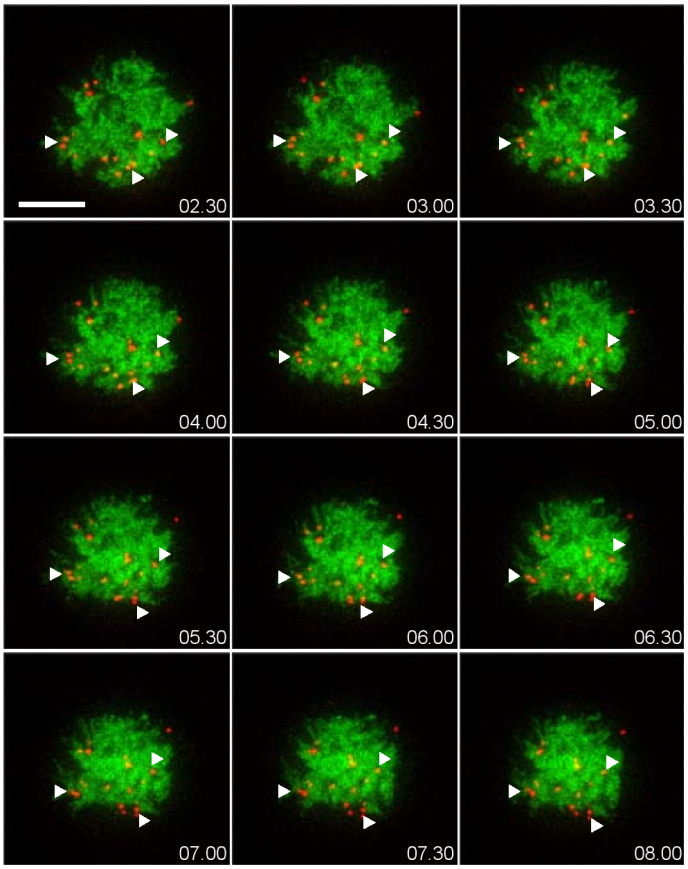

Figure 4.25: PML NB dynamics upon calyculin A induced premature chromosome condensation (PCC). A double stable cell line, CpYs68, was transiently transfected with H2A-mCherry construct. Cells were then treated with 40 μM Calyculin A for 30 min to induce premature chromatin condensation before 4D live cell imaging by the DeltaVision RT microscope (N = 10). A 24 μm z-stack of 1.5 μm steps was taken in the CFP and mCherry channels every 10 sec for 33 min. The 3D projected still images from selected time points are shown here. Condensed chromosomes can be visualized by the H2A-mCherry fluorescent signal (pseudo-colored in green). PML NBs (pseudo-colored in red, the white arrowheads) do not exhibit dynamic movement within the increased interchromatin space. Bar, 10 μm.

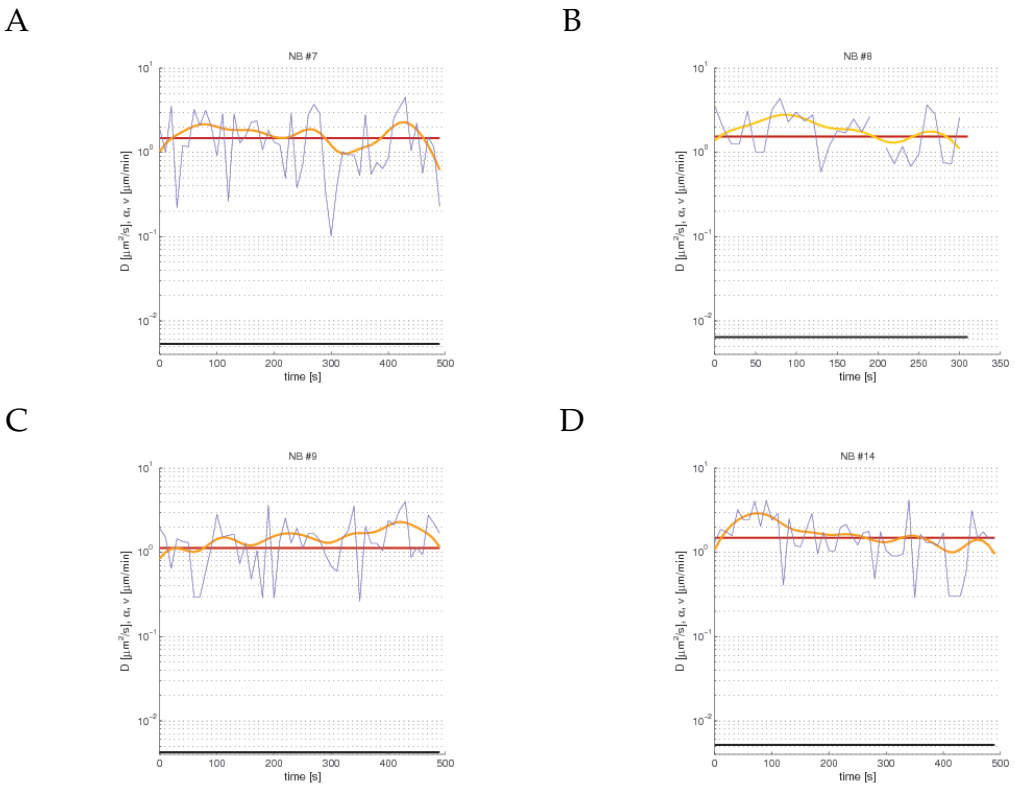

Figure 4.26: Calyculin A treated cells do not mimic prophase cells. Selected correlations between diffusion coefficient D (black solid line), α coefficient (red solid line), velocity raw data (dashed blue line) and smoothed velocity (orange solid line) plotted over time. No break points were found, velocity remains mainly constant (except for random fluctuations) and seems not influenced by the calyculin A treatment. A similar behaviour was found with all other PML NBs in the same experiment.

fused to importin-β binding domain (IBB) of importin-β ([105, 32]). Effective partictioning of nucleoplasm and cytoplasm by an intact nuclear envelope is a prerequisite for active import of the IBB fusion. The equilibrium of this import is sucht that the IBB-HcRed signal is restricted within the nucleus during interphase. IBB-HcRed appeared in the cytoplasm during the transition from prophase to prometaphase, thereby marking the initiation of NEBD ([105]). Therefore a triple stable cell line, CpYsRi89, stably expressing PML-ECFP, EYFP-Sp100, and IBB-HcRed was created. Cells at the G2/prophase transition were identified by partially condensed chromatin, as visualized by Hoechst DNA staining (4.27A).

4D live cell image stacks with 0.5 μm steps were collected in the HcRed and YFP channels every 8 sec for 20 min. As shown in the still images (figure 4.27 A), chromosome condensation was observed during early prophase whit IBB-HcRed being restricted to the nuclei before NEBD. The timing of IBB-HcRed release from the nuclei coincided with the dissipation of Sp100 (data not shown). I extracted the time point of PML NB mobility change to assess its temporal relation to NEBD. Live cell data sets were synchronized by shifting the time zero for each trajectory to the time point of the onset of NEBD, which is indicated by the appearance of the IBB-HcRed signal in the cytoplasm. The number of break points that occurred at each time interval relative to NEBD was counted histogrammed (figure 4.27 B). Clearly, the majority of PML NBs changed their mobility before NEBD as the peak number of break points appeared before time zero. Therefore, the physical flow between the nucleoplasm and the cytoplasm is unlikely to be the driving force to change PML NB movement types in early mitosis.

4.2.7 PML NBs increase their dynamics due to loss of tethering to chromatin

In my search for the driving force behind the increase in PML NB mobility during prophase so far, I have ruled out the increase of interchro-

A

EYFP-Sp100, IBB-HcRed,
Hoechst

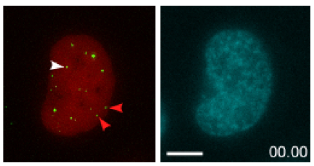

B

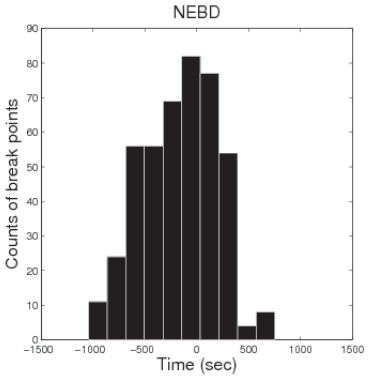

Figure 4.27: PML NBs dynamics upon nuclear membrane breakdown. (A) Triple stable cell line, CpYsRi89, stably expressing PML-ECFP, EYFP-Sp100, and IBB-HcRed. An 8 μm z-stack of 0.6 μm steps is collected every 8 sec for 20 min in the YFP and the HcRed channels. A single z section at the middle of the cell was taken at every time point in the Hoechst channel as the reference image for DNA. Nuclear membrane breakdown was visualized by the release of the HcRed signal from the nucleus into the cytoplasm. Bar, 10 μm. (B) Histogram of breakpoints calculated by the MLE approach. 6 live cell data sets were collected from the CpYsRi89 triple stable cell line. By visualizing the release of the HcRed signal from the nucleus into the cytoplasm, the time point of NEBD for each data set was defined as time = 0 in order to synchronize and compare timing between the data sets. The majority of the break points occurred before NEBD.

matin space due to chromatin condensation and the mechanical flow due to material release into the cytoplasm at NEBD. I shall now examine if the constrained PML NB mobility during interphase was caused by the attachment of the PML NBs to chromatin. If this hypothesis was correct, a drop in chromatin association should coincide with the change of PML NB velocity. To assess this possibility, I examined the live cell data sets containing H2A-mCherry and EYFP-Sp100 signals in more detail with regard to the interactions between PML NBs and chromatin. The chromatin intensity (I) surrounding each PML NB was computed as the mean intensity of all voxels in the chromatin channel occupied by voxels in the segmented PML channel. The segmented PML NB images therefore served as masks defining the space occupied by the NBs plus one layer of voxels around them corresponding to approximately 200 nm. Any contacts within this space are visible (see chapter 3.2.5) as an increase in the mean chromatin intensity. Diffusion coefficient (D), coefficient of anomalous diffusion (α), and velocity (v) were again calculated from the same track in order to follow the change in PML NB mobility. Plots of all four parameters in each individual track were plotted as a function of time as pointed out in figure 4.23. At least three types of correlations between PML NB mobility and chromatin localization can be observed quantitatively in a typical prophase cell (4.28). The first type of PML NBs increased their mobility while maintaining their colocalization with chromatin (figure 4.28 A). Interestingly, they often show a moderate increase of velocity but exhibit a much elevated coefficient of anomalous diffusion. This type is likely to remain associated with chromatin following the movement caused by chromosome condensation. The second type's increased mobility coincided with lost colocalization with chromatin (figure 4.28 B). In contrast to type one, type two PML NBs show much higher velocity but a somewhat smaller α coefficient of $\sim$ 1.5. The implication is that type 1 PML NBs (attached) are constrained by chromatin movement whereas type 2 PML NBs (detached) move freely only after detaching from chromatin. Since α is significantly larger than 1 in type 2 there appears to be a superdiffusive component in the mobility of this type. This suggests that type 2 particles

show characteristics of both free diffusion and directed motion. . In addition, I also found a third type of PML NBs fluctuating between the two states (figure 4.28 C).

This type of PML NB was first pulled by the contracting motion of chromosome condensation as they remained attached to chromatin, and the PML NB was then released from chromatin and moved freely. At a later time point, the free-moving PML NB was trapped by chromatin again. Taken together, PML NBs occur both in an attached and detached state and they can readily switch between the two. In my observation the attached state was more abundant during entry into mitosis while the detached state became more prevalent later. This makes detachment from chromatin the likely mechanism behind the observed increase in PML NB dynamics during prophase.

4.2.8 Timing of increased PML NB dynamics during prophase

Next, I was interested in determining when PML NBs detach from chromatin and in identifying the trigger for the global increase of PML NB dynamics during prophase. As mentioned in chapter 1.3.2 the MPF complex commits the cell to mitosis and promotes metaphase progression by phosphorylating a variety of substrates, including nuclear lamins and condensins ([114]). Cytoplasmic MPF is translocated from the cytoplasm into the nucleus during late prophase ([90]). At this time a global increase of directed PML NB movement was observed in this work. Therefore, I investigated whether the translocation of cyclin B1 correlated with the increase of PML NB dynamics. Another double stable cell line, CpYcb165, was created. It stably expresses PML-ECFP and EYFP-cyclin B1. A transient transfection with H2A-mCherry was added for chromatin visualization. This helped to identify early prophase cells. Z-stacks with 0.5 μm step size and an extension along z of total 8 μm were collected with time intervals 8 seconds over 30 minutes in both CFP and YFP channels. Of H2A-mCherry

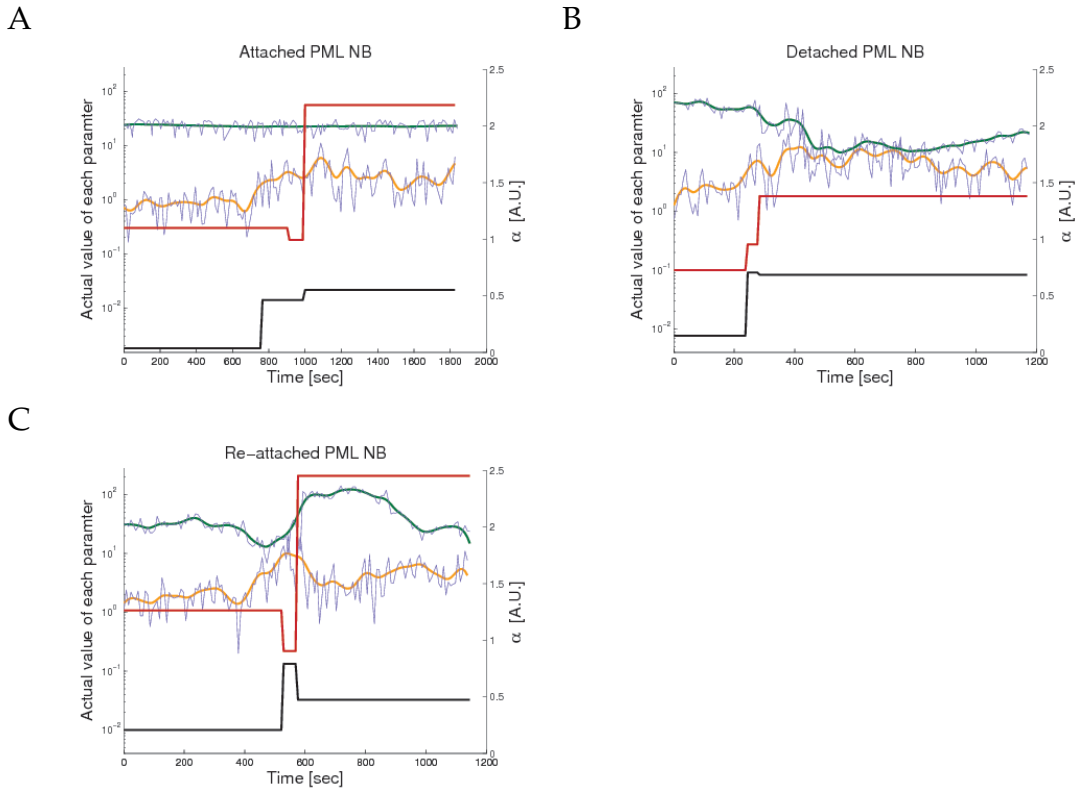

Figure 4.28: Selected correlations between PML NB mobility and chromatin colocalization. Four parameters were obtained for each particle track and plotted over time. The change of chromatin intensity (I) indicates the change of proximity between PML NBs and chromatin, and the variation of velocity (v), diffusion coefficient (D), and coefficient of anomalous diffusion (α) indicate the change of PML NB mobility and movement type. Three types of correlations can be typically observed in a prophase cell. One example track of each type is shown here. The ordinate on the left is the actual value of I, v, and D (log scale). The Y-axis on the right represents α using a linear scale. (A) Attached: a PML NB was attached to chromatin and moved along with chromatin. (B) Detached: a PML NB was released from chromatin and showed increase mobility. (C) Switching: a PML NB was released from chromatin but then re-attached to chromatin at a later time point.

only one reference z-slice was recorded. Upon reaching the G2/prophase transition, EYFP-cyclin B1 was mainly diffusely distributed throughout the cytoplasm and was excluded from the nucleus. I found it to be concentrated as well at the duplicated centrosomes as reported previously ([90]) (figure 4.2.8 A, t = 0 min).

Those centrosomes labeled with EYFP-cyclin B1 mark the end of G2 phase when migrating to the opposite poles of the nucleus, a time after which cells typically enter mitosis within 30 minutes. Image acquisition was started when the centrosomes started to separate even before chromatin condensation became apparent. Nuclear envelope breakdown was visualized by release of cyclin B1 from the nucleus and its distribution throughout the mitotic cell within 6 minutes. My observations suggest that the EYFP-cyclin B1 fusion protein behaved as previously described ([80]). Intrigueingly, PML NBs did not exhibit significantly increase mobility at the beginning of prophase. This increase rather occured upon cyclin B1 translocation into the nucleus, where I observed fast movement and MAPP formation (Figure 4.2.8 A, t = 20). Cyclin B1 dissipation indicated NEBD near the 30 min after the beginning of data acquisition. In order to quantify the change of PML NB mobility in relation to cyclin B1 nuclear entry, I also determined the break points of each track by using the same MLE approach described previously. As summarized in figure 4.2.8 B, the time zero was shifted to the time point when the appearance of the EYFP-cyclin B1 signal was observed in the nucleus to make experiments comparable. This time around, most break points were observed after time zero. Thus, the change in PML NB dynamics coincided the nuclear entry of cyclin B1 or occured shortly thereafter. In numbers, 84% were seen after cyclin B1 entry, while 16% of the break points appeared 3 min before time zero. The trigger of cyclin B1 entry may thus also trigger the increase of PML NB dynamics during prophase. Taken together with the previous results, these data indicate that the increase of PML NB dynamics and the formation of MAPPs occur, for the most part, between cyclin B1 nuclear entry and NEBD.

A PML-ECFP, EYFP-cyclin B1 B

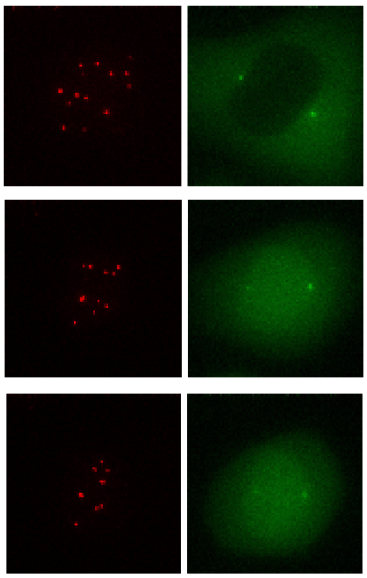

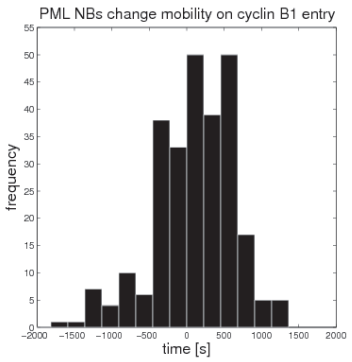

PML NB dynamics upon nuclear entry of cyclin B1. (A) Double stable cell line, CpYcb165, stably expresses PML-ECFP and EYFP-cyclin B1. Cells were transiently transfected with an H2A-mCherry construct to visualize chromatin. An 11 μm z-stack of 1 μm steps was collected every 15 sec for 35 min in the CFP and YFP channels. The 3D projected images show that PML NBs exhibited limited movement before cyclin B1 entered the nucleus. After the nuclear entry of cyclin B1, PML NBs became dynamic, and long distance displacement and fusion of PML NBs were observed (A, t = 20 min). Bar, 10 μm. (B) Histogram of breakpoints calculated by the MLE algorithm. 8 live cell data sets were collected from the CpYcb165 double stable cell line. By visualizing the entry of cyclin B1 into the nucleus, the time point of cyclin B1 entry for each data set was defined as time = 0 in order to synchronize and compare timing between the data sets. The majority of the break points occurred after cyclin B1 entry.

Chapter 5

Discussion

5.1 Histone H1° dynamics in the nucleus

I have presented a solid, quantitative description of the dynamics of wild-type H1°-GFP and seven mutants with differential binding activity. This was possible by combining *in vivo* fluorescence photobleaching with a numerical diffusion model. With my approach I have been able to estimate an effective diffusion coefficient for each mutant which has allowed me in turn to estimate the free fraction of H1°-GFP, including the WT and all mutants. Therefore, I have obtained a quantitative measure for the binding affinity of GFP-labeled proteins to their immobile intracellular target, in this case the chromatin scaffold. By combining FRAP and modeling with FCS measurements I could dissect the binding contributions from the diffusive component of protein mobility.

5.1.1 H1° binding and diffusion - an emerging picture

Some earlier works made quantitative statements while neglecting the diffusive component. For example the first study to quantitatively describe

chromatin binding of H1°-GFP successfully established the existence of a binding component in its diffusion [121]. The authors also analysed differences between H1 variants H1° and H1^c. Interestingly, they observed a marked decrease of the recovery time in FRAP experiments upon hyperacetylation caused by the histone deacetylase inhibitor trichostatin A. They interpreted this as an enlargement of the mobile fraction of H1. The same authors also used the recovery time, after which a plateau could be observed as an estimate for the residence time of H1° on its chromatin binding sites. It has been shown that in cases with a large bound pool and very fast or instantaneous reactions only a lower limit of an off-rate can be derived (this work as well as [20, 182]). One can rather expect to be able to estimate the ratio of the kinetic on- and off-rates. Their estimate of 220 s for WT H1°-GFP should therefore be interpreted as the maximal residence time on chromatin. Besides that, the exact time of the plateau in a FRAP recovery is somewhat difficult to read from the experimental data, since the plateau can be strongly influenced by undesired photo-bleaching during post-bleach acquisition. Due to the relatively small, but non-zero, curvature of the recovery function in this area noise has can have a detrimental effect as well. The ratio of kinetic on- and off-rates is equivalent to the free fraction. When comparing the free fractions estimated in this work with those of others I note that the $0.06 \pm 0.01\%$ found here for WT H1°-GFP are in a similar range to the 0.08% found in [182] within the error range inherent in such work. The values of $0.03 \pm 0.01\%$ to $0.09 \pm 0.04\%$ found by [20] for different subtypes of H1-GFP is also in good agreement with my work.

Another work which analyzed an H1 histone variant, H1.1, by fluorescence photobleaching is [102]. Strikingly, they also photobleached ROIs of varying sizes, but they did not find any differences in the recovery. This is in stark contrast to this work and also to [20]. Consequently, Lele et al. drew the conclusion that a FRAP recovery of H1.1-GFP was not diffusion limited and therefore could be modeled by a simple first-order kinetic rate law of the type $F(t) = 1 - \exp(-t \cdot k_{off})$ allowing them to estimate k_{off} directly from the recovery. The authors even used NIH 3T3 fibroblasts for

expression, like I did. It is not clear how such opposite behaviour of a very comparable system could be observed. However, there are some details in their methodology which may cast doubts on their findings. For example, in order to estimate the ratio of free to bound H1.1 the authors used Triton extraction to remove all unbound protein and quantified the fluorescence before and after treatment. This method appears somewhat questionable since, as the authors mention themselves, it is not clear how much of the bound fraction gets removed nor if all free protein gets removed completely. Therefore, they employed a pre-bleaching step for 3s to remove freely diffusing protein. Their reasoning was that freely diffusing protein would be removed within that time. However, this was only true if the timing of the diffusion process would be equivalent to free GFP. This assumption may or may not be correct for any given protein under study and therefore it may be violated. As I have shown here diffusive processes can be dramatically slowed down by a fast on-kinetics. This could mean they did remove all free protein by prebleaching. Likewise, it is also not clear if bound protein comes off its binding sites as well during the bleaching step. Thus, one can not expect a very reliable free/bound ratio from such an approach, where too many competing processes may be occuring that can not be quantitated. Lastly, it appears to be a conceptual weakness to use a k_{on}/k_{off} ratio in this way, where, as the authors admid to themselves, the observable on-rate is in reality a pseudo-on rate with the number of binding sites in excess, i.e. a $k^*_{on} = k_{on} \cdot [binding\,sites]$. I conclude, that in light of so many question marks their approach presented and the estimated parameters must be doubted. It appears that the authors falsely missed the diffusive component due to the bleaching protocol they used for FRAP including a very long 3 s bleaching pulse which consequently led them to the wrong conclusions about the underlying mechanism.

A more detailed analysis of linker histone diffusion and binding was presented by ([23]). Like in my work a combined approach of FRAP, FCS and numerical modeling was employed. They were able to establish that H1.1

GFP-fusion protein has two diffusion times on different orders of magnitude. This behaviour was only observed inside the nucleus, while in the cytoplasm only one diffusion time similar to the faster diffusion time was found. Their assumption that the slower diffusion time arises from binding was further supported by numerical simulations of FCS curves using a similar model as in [193]. Since the slow component is interpreted as arising due to binding I conclude that also on the size and time scales of FCS the binding of linker histones gives rise to an observable slowed diffusion process. This was also observed using FRAP in this work. Interestingly, they too observed subdiffusion both in the cytoplasm as well as in the nucleus. This is consistent with my FCS results with H1°-GFP in the cytoplasm. Anomality is typically not seen on the spatial scale and time scale of FRAP experiments because it is a transient phenomenon. It occurs only locally as a local confinement of the diffusing particle. Therefore FRAP only yields diffusion coefficients describing normal diffusion while diffusion coefficients derived by live cell FCS tend be of subdiffusive nature. This complication of the interpretation and comparability of such diffusion coefficients is typically not much regarded in the literature and represents an unsolved problem in this field.
The emerging view of linker histones is that they are higly dynamic, rapidly diffusing inside the nucleus. Despite their rapid, partially subdiffusive motion linker histones experience a strong affinity to chromatin which is why at any given time only a small fraction is diffusing while a large fraction is chromatin-bound.

5.1.2 Influence of amino acid replacements on H1° binding affinity

The recovery half-times published by [28] allow a preliminary assessment of the binding affinity of the H1° mutants under study. Sorting the mutants according to recovery half-times overall matches the sequence of binding affinity found in this study (Brown et al.: E62H > K82V > WT

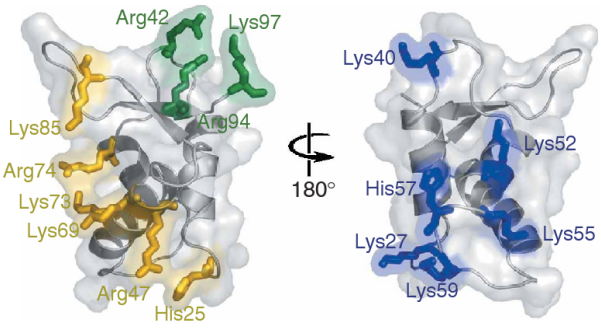

Figure 5.1: Structural map of binding and non-binding amino acid residues based on homology modeling of the avian H5 globular domain. Residues positioned in putative binding sites are shown in yellow and green, residues on the opposite face in blue. Adapted from [28].

> K59A > K97A > R74A > H25G > R47A; this study: E62H > WT > K82V > K59A > K97A ~ R74A ~ H25G > R47A). Table 5.1 gives a side-by-side comparison between the two works. There are a few noteworthy differences which shall be discussed in this chapter. The three mutants K97A, R74A and H25G have been characterized here with very comparable binding affinities of about one fifth compared to WT. I note that they all are part of putative binding sites in the 3D structure of H1° which was modeled into the crystal structure of avian H5 (5.1). This suggests that the contribution of the respective basic amino acid residues contribute similarly to DNA binding, both among each other as for binding site 1 (mutants H25G and R74A) and between both binding sites. R47A being part of binding site 1 has the strongest effect in both studies. All these moieties are in close contact with one another and appear structurally ideally suited to confer DNA binding. Also in good agreement with the recovery time previously published is the mutant K59A. With 45% binding affinity compared to WT it represents an intermediate influence of its residue, where 37 s recovery time also is an intermediate result in Brown et al. Structurally it faces away from the putative interaction area. It is not clear if this represents an artifact of the structural model used or if the moeity stretches out far enough to still make contact to the DNA backbone. The only acidic amino

acid residue mutated in my set of seven mutants, in contrast to the basic lysines or arginines, apparently strongly reduces DNA binding. This is evident from both the longest recovery time as well as the highest binding affinity measured in each study. Consequently, the electrostatic repulsion between the glutamate and the DNA backbone may be responsible. In the mutant E62H I even find a stronger binding affinity than WT H1°. The only mutant which does not fit in with regard to its position in the sequence of binding affinities or recovery times, respectively, is K82V. With regard to the binding affinity measured here it is comparable to the intermediate K82V. However, the recovery time published rather suggests an increase of binding affinity upon mutation of K82. The K82V example underlines, together with figure 4.7, that there is considerable uncertainty in the precision of the parameters. The binding affinities were calculated from the estimated diffusion coefficients. Since the diffusion coefficient is inversely proportional to the diffusion time (though strictly this is true only for cicular bleach geometries) one would expect the order of the mutants to be the same. The uncertainty in the parameters may either be inherent to the method relying on recovery times in [28] as these may vary with the exact size of the bleached spot. The uncertainty may also represent a considerable variation in the analysed cell populations. The fact that such variability exists is underlined by my observation of different expression levels as well as diffusion times in FCS. Such biological variance in the data is likely to be inherent both to my estimated binding affinities as well as to the recovery times published previously. As shown in chapter 4.1.4 the actual simulation and parameter estimation is self-consistent to a much higher extent rendering its contribution to the overall error mostly negligible. Overall, the box plot of the observed diffusion coefficients in figure (4.7) shows that the parameters vary considerably. Judging from the plot they fall into three different groups with 95% confidence: [E62H, WT], [K82V, K59A] and [K97A, R74A, H25G, R47A]. The first group correspond to the strong binders wild-type and lacking repulsive glutamate. The second group are those of intermediate binding strength, possibly not as close structurally as the strong binders. The last group of strong binders

H1° variant	k^*_{on}/k_{off} rel. to WT [%]	t_{50} [s] found in [28]
E62H	141	76
WT	100	52
K82V	49	63
K59A	45	37
K97A	23	20
R74A	22	14
H25G	23	12
R47A	18	5

Table 5.1: Comparison between binding affinities estimated in this work and recovery half-times published by Brown et al. ([28]). The rightmost column re-iterates the half-times t_{50} of recovery found previously.

are all from the amino acids which are part of the predicted binding sites to DNA. Therefore, FRAP in combination with FCS and numerical modeling is suitable to differentiate the binding behaviour of point mutations quantitatively and to relate that information to structural detail.

5.2 Dynamics of PML nuclear bodies during early mitosis

5.2.1 PML NB mobility increases with commitment to mitosis

PML NB dynamics has been studied extensively in interphase nuclei ([70, 125]). I have shown that PML NBs display obstructed movement to a relatively large extent (30 %) during interphase and only a small fraction with directed movement (10 %) which is in agreement with these previous works. In contrast to interphase the dynamics of PML NBs during early mitosis has only recently come into the focus of research ([47]). According to my study the proportions of directed movement and obstructed motion are approximately reversed by the end of the observation period. This

was demonstrated by classification of MSD plots of single particle trajectories. I have correlated the timing of the increase of PML NB dynamics to molecular events, specifically entry of cyclin B1 into the nucleus and to NEBD. Classically, the stages of mitosis are defined according to morphological changes observable by light microscopy. According to this classification and my observations, the mobility of PML NBs during prophase shows a larger fraction of directed motion than interphase and a smaller fraction of obstructed mobility. During prometaphase the distribution of mobility types shifts further towards directed motion as stated above. An alternative model for classification of mitotic sub-stages based on the activity of cell cycle regulators has been suggested by [136] (see also chapter 1.3.3). Interestingly, the authors stressed a point-of-no-return which inevitably commits the cell to mitosis. This coincides with increased cyclin B1 / CDK1 activity, termed "transition 2". My observations indicate that the increase in PML NB mobility occurs during this stage. Thus, my studies indicate that the increase of PML NB mobility takes place only after the cell has passed the irreversible mitotic check point.

5.2.2 Dissecting the chronological order of changes in PML NBs

Transition 2 begins with cyclin B1 entry into the nucleus and ends with NEBD. A global increase of PML NB mobility could be shown by classifying early mitosis into two phases using MSD plots and estimation of the α parameter. This global increase falls into the time frame of late prophase and early prometaphase. However, the precision of the MSD-based classification is not sufficient to discriminate the precise sequence of events. Therefore, I employed for the first time in a cell biological context the model-free MLE-based approach introduced by [123] to automatically detect sudden changes in PML NB mobility. Using this strategy in combination with molecular markers for cyclin B1 entry and for NEBD, respectively, I was able to demonstrate that the increase of PML NB mobility

occurs between both these events and therefore during transition 2. This observation re-inforces my view that physical flow created by NEBD is not the driving force for the increase in PML NB mobility, since a substantial fraction of NBs displays this increase before NEBD. Previous works have demonstrated that the MPF promotes the phosphorylation of several nuclear targets, such as lamins and cdc25 thereby committing the cell to mitosis ([175]). It seems plausible that the MPF is also responsible for removal of constraints on PML NBs, although the temporal resolution with which I have determined the increase in PML NB mobility does not allow me to prove this hypothesis conclusively. Moreover, the exact mechanism of the increase remains to be elucidated in the future.

5.2.3 PML NBs and chromatin interaction

Since the increase in PML NB mobility goes along with chromatin condensation one potential candidate for the mechanism behind this is the opening up of interchromatin space and concomitant release of PML NBs from chromatin corrals. Therefore, premature chromatin condensation was induced by CA. The CA treated cell nuclei did not show increased dynamics of PML NBs as observed in prophase cells, but rather PML NBs remained tethered to chromatin and appeared to be pulled along due to its condensation. This was seen in aster-like trajectories revealing that PML NBs are pulled towards the center in CA treated cells. The same result was obtained by high salt treatment of the cells (data not shown). I can conclude, that there must be a different mechanism which links PML NBs to chromatin other than pure spatial constraints. My view is reinforced by the analysis of chromatin density around PML NBs. This colocalization on a size scale of light optical resolution (~250 nm) reveals detachment from chromatin. While remaining attached to chromatin in CA treated cells, a large proportion of PML NBs detached from chromatin upon increasing their mobility.
In a previous study ([70]) the authors found PML NBs to move in a subd-

iffusive manner as well and interpreted this as a spatial confinement, the corrals. Opening up of these corrals, according to their view, facilitates PML NB movement and leads to an increase in their velocity. Their observation is consistent with mine during early mitosis, where many particles appear to loose contact with chromatin upon speeding up. However, it remains unclear, which or if molecular interactions are involved in tethering PML NBs to chromatin. In light of the results obtained in CA treated cells it appears unlikely that chromatin condensation and therefore loss of spatial constraints is the main mechanism responsible for increased PML NB dynamics.

5.2.4 Anomalous diffusion on the scale of subnuclear particles

The property which I have used to determine mobility changes of PML NBs in the nucleus was the coefficient of anomalous diffusion, α. I have not yet discussed its absolute value, however. It has been shown, that anomalous diffusion, in particular obstructed diffusion[1], is a general property of both the cytoplasm and the nucleoplasm on the scale of nanoparticles ([76, 75, 194, 193, 156]). It appears that obstructed diffusion occurs more generally in crowded solutions, which are typically found intracellularly. Attempts have been made to visualize this crowded nature of the cytoplasm (see figure 5.2).

Since a large part of the cytoplasm (and nucleoplasm) is comprised of protein (about 40%, see [64]), a diffusing particle experiences anomalous diffusion. It has been shown using 5 nm gold beads that the coefficient of anomalous diffusion is about $\alpha \sim 0.52$ in the cytoplasm and $\alpha \sim 0.58$ in the nucleoplasm [76], or more generally about $\alpha \sim 0.55$ ([75]). The median value found using labelled PML bodies in the nucleoplasm of interphase

[1]The diffusive regime with $\alpha < 1$ is often referred to as subdiffusion in the biophysical literature, while "obstructed diffusion" is more common in cell biological publications.

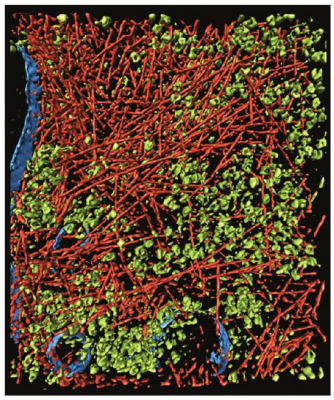

Figure 5.2: Cryo-electronmicroscopic image of the cytoplasm. The crowdedness of the cytoplasm is highlighted by rendering just two very abundant protein complexes, namely actin fibers (red) and ribosomes (green). The cell membrane is shown in blue. Adapted from [117] .

cells in this study is similar at $\alpha \sim 0.6$, if somewhat higher. It appears therefore, that the visco-elastic properties reported for the nucleus for 5 nm beads are also relevant on the size scale of a PML NB, which is a globule with a diameter of about 0.5 μm. It was also demonstrated that osmotic stress with high sucrose concentrations can lead to a decrease in anomality in the nucleoplasm with $\alpha \leq 0.7$, allegedly due to a loss in molecular crowdedness ([75]). In my study during early mitosis a strong increase of α was found with one peak around 1 and another near 2. The latter can be attributed to directed motion in those PML NBs which are tethered to chromatin and are dragged by it. An interpretation of the former, however, remains somewhat elusive, as the observed value suggests a loss of anomality in the nucleus before NEBD. What process could cause such a dramatic change is not known. It can only be hypothesized that chromatin condensation and / or the break down of a putative nucleoskeleton ([74, 176]) might change the visco-elastic properties of the nucleoplasm. Some support of this hypothesis may be drawn from the observation that the hydrodynamic properties of the nucleoplasm can be described by the Zimm model for polymer solutions ([75]). According to that model (as verified experimentally by osmotic stress), a change in solvent properties

can lead to a loss in anomality and elasticity of the fluid. The latter reflects a reduction in longer range restoring forces due to the emergence of more aqueous cavities. As a result of this the degree of entanglement among proteins and DNA would decrease which leads to a loss of anomalous subdiffusion. Anomalous subdiffusion has been shown to facilitate sampling of a three-dimensional environment, thereby increasing the probability of molecular interactions ([77]). On the other hand a large degree of subdiffusion hampers the mobility of cellular constituents. Since large-scale morphological changes including migration of chromosomes have to take place during mitosis, a loss in anomalous subdiffusion may facilitate these processes.

5.3 Outlook

I have provided a detailed quantitative analysis of the mobilities and dynamics of H1°-GFP, exemplifying a small DNA-binding protein, as well as of PML NBs representing large macromolecular aggregates inside the nucleus. I have employed a methodology which combines time-resolved fluorescence microscopy with computational modeling and classification approaches to gain new insights. My understanding of processes inside living cells is increasingly shaped by such techniques which allow a highly informative view on the spatio-temporal interrelations.

Here, I have presented an analysis of the binding interactions of H1°-GFP wild-type and seven point mutants with substitutions in the globular binding domain. I was able to differentiate between strong and weak binding quantitatively by using FRAP analysis and numerical modeling. In combination with FCS I could dissect the diffusive proportion of H1°-GFP mobility from its binding affinity. This allowed me to relate binding affinities gained from *in vivo* data to molecular detail based on structural knowledge about the H1° protein.

I have demonstrated that PML NBs exhibit a global increase in mobility

during early mitosis. I also have provided evidence that this increase occurs due to loss of tethering to chromatin. However, my methodology is not ideally suited to provide a formal proof of a molecular interaction. Therefore, in future works my data would benefit from being complemented by methods which can provide such information. In terms of fluorescence microscopy a well established and widely applied method would be FÖRSTER resonance energy transfer (FRET). With this technique it could be tested if a constituent protein of PML NBs is in close contact with chromatin on an Angstrom scale relevant for biochemical interactions.
Further developments in image processing and registration may facilitate particle tracking and interpretation of tracks. The rigid registration scheme employed in this work is capable of compensating for overall translational movement and rotation of the cell nucleus. However, during prophase the global morphology of the nucleus changes rapidly and dramatically. These changes may affect the trajectories obtained. In this work I used a combination of the estimated α parameter in conjunction with chromatin density data to dissect the fraction which is bound to chromatin from the one which is not. Nevertheless, the overall morphology change may account for a considerable part of the fast moving directed fraction of PML NBs. As an alternative to rigid body registration there are types of deformable registration such as the Demons registration. The latter represents a family of registration algorithms which apply a transformation vector field to each image to compensate morphological changes. The complexity here is that one obtains a transformation component in the particle trajectories which is non-trivial to interpret (unpublished results based on personal communication). Therefore, this advanced registration technique was omitted from this work. A prerequisite for the routine application of such flexible registration schemes may be the definition of a standard geometry to register cells or cell nuclei to. Future improvements in the application of deformable registration to biological samples may improve this situation and lead to a more detailed understanding of particle movement inside rapidly deforming (sub-)cellular structures.
As pointed out in the results section of PML NB tracking (chapter 4.2.3)

a complex multi-dimensional data set (3D + time + channel) was transformed into another complex multidimensional data set (4D trajectories, time-resolved local chromatin density, D(t), α(t), v(t)). This has allowed me to correlate each parameter and therefore to draw conclusions about a complex behaviour. Others have pointed out ([100]) how different biophysical techniques available on current commercial confocal microscope systems, such as time-resolved FCS, FLIM, fluorescence anisotropy decay, excitation and emission spectra, quantum yield and FRET, can be utilized to dissect complex biological problems and allow interpretations where each single technique would not yield enough information to allow a stringent data interpretation (see also [196, 188, 122]). These techniques allow researchers to probe molecular volumes, shapes, distances, crowding, photophysics, to name a few, on sub-optical scales. Thus, in the future this trend towards multiparameter fluorescence microscopy may become more prominent and help to open a window into nanoscale cellular machinery.

Interestingly, the anomalous diffusion coefficient allowed an insight into, both, the type of mobility of individual particles as well as the degree of molecular crowding experienced by PML NBs. The latter property might be combined with information on visco-elastic properties of the nucleoplasm. These properties can be estimated from the MSD as the complex shear modulus (see [75]). This might allow future researchers to assess the temporal changes of visco-elasticity in the nucleoplasm during mitosis, which has been alluded to in this work by the observation of an increasing α parameter.

The labeling technology used in this work was based on fluorescent proteins. Since the first cloning of GFP from *A. victoria* FP-technology is nowadays heavily relied on by cell biology and biomedical imaging. Advances in this technology have been made so as to yield new spectral variants with increased photostability ([159, 68, 4]). This process is still an active field of research. However, all FPs have the drawback of being relatively bulky. In the context of my work for example, GFP with its 26 kD has about the same molecular weight as H1° histone making it as large as its

target. The inherent question is always weather or not such a large FP moiety might influence the biological function. In particular, in this context of quantitative measurements regarding binding constants one has to bear this criticism in mind. Even though normal biological function has been demonstrated biochemically, one can never be sure that the biochemical equilibria remain the same. Therefore, other smaller protein tags have been developed which are genetically encodable and lead to a much smaller tag, such as chromobodies (15 kD, [151]), FAP ([174]) and FlaSH in the size range of 1 kD [73, 2]. All these labelling techniques have been designed to be less interfering with protein interactions *in vivo*. Even though increasingly used the high cost of commercially available kits and practical drawbacks of the staining procedure have, as in the case of FlaSH, so far hampered the breakthrough into routine research. No matter how small, any fluorescent label intrinsically represents an interference with the target protein and entails ectopic overexpression. Therefore, approaches which do not require any fluorescent labeling appear extremely attractive. Such endeavours have been undertaken by using coherent anti-Stokes Raman spectroscopy (CARS) for microscopy to establish a chemically selective detection regime ([199, 148, 147]). The field is rapidly growing and the universal applicability of CARS remains to be proven in the future.

PML NBs are relatively large entities which can be readily detected using light microscopy. Many protein machineries (e.g. snRNPs, ribosomes, nuclear pore complexes and many more) cover, however, a size range around a few tens of nanometers, which is not readily accessible by standard fluorescence microscopy. Superresolution techniques circumventing the classical Abbé resolution limit may help to further my knowledge in this very interesting size range. One very successful approach in this area is based on stimulated emission depletion (STED) which is currently greatly expanding the scope of biological imaging ([85, 84]).

A general observation made in this work was that standard deviations on the estimated parameters were large, which limits the precision of data interpretation. Both, the binding analysis of H1°-GFP as well as tracking of PML bodies have been somewhat hampered by the relatively low cell

number which could be addressed in the scope of this work. Both were in the range of $10^1 - 10^2$ cells. This order of magnitude is typical of current *in vivo* studies on the single cell level. This fact is due to the relatively laborious manual implementation of the cell transfection and mounting as well as finding suitable cells based on subjective experience. An upscaling of the experimental procedures using high content screening techniques may be crucial in generating a larger amount of data. Data analysis was already automated to a large degree in terms of image pre-processing and computation of biophysical parameters. Among the main bottle-necks was for example the tracking procedure, which works well in interphase cells, where particles move only locally ([14, 70]). However, in prophase cells, due to the increase in particle mobility and MAPP formation crossing trajectories as well as splitting and merging events are frequent. The automated tracking routine therefore tends to loose the current particle quite often and to follow a different particle. Manual correction of particle tracks is therefore necessary, which is time-consuming. Another bottle-neck currently is the available speed of data acquisition. With several channels and multiple z-Slices the data was recorded at an average time interval of 8 s per image. However, with rapidly moving particles this may lead to aliasing problems. A higher acquisition speed would therefore result in less manual corrections and a more precise estimate of velocities. Even with the fastest confocal scanning available today the time interval would not be much smaller than 1 s with three channels. Novel imaging techniques in the future may improve the time resolution of 5D microscopy. Likewise, the mobility of protein ensembles in FRAP experiments is often much higher than observed in the example of H1°-GFP. In such cases where the diffusion coefficient of the FP-construct approaches that of free GFP one misses the most informative first part of a recovery. This part has the largest curvature and contains most information. Moreover, this part may be crucial to distinguish between effective diffusion and such regimes, where binding and diffusion occur on different time scales ([167]). In the context of this work high content screening techniques might help to increase the confidence intervals of the parameter estimation or detection of break points.

Therefore mapping the timing of the events under study to other cellular events or the determination of kinetic parameters needed for building predictive models may become possible with higher precision. This would on the long term help to build a spatio-temporal interaction map of a cell's biological functions.

Chapter 6

Appendix

6.1 Supplementary figures

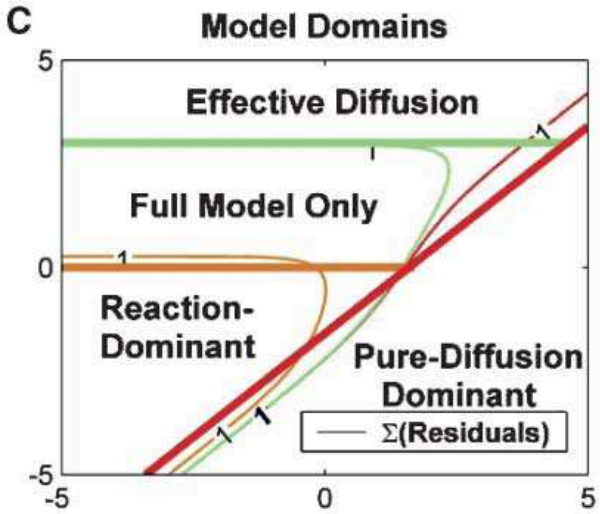

Figure 6.1: Practical considerations for evaluation of a reaction-diffusion system analyzed by FRAP. A double-log plot of reaction rates k^*_{on} and k_{off} on the y-axis and x-axis, respectively, explores the parameter space for binding rates. Simulated data sets with D = 30 $\mu m^2 \cdot s^{-1}$ and bleach diameter 0.5 μm were fitted with different limiting-case models as described in [169]. Each parameter pair results in a different sum of residuals indicating the goodness of fit. The boundaries equivalent to sum-of-residuals-equals-1 are superimposed. Thereby different regimes become appearent which can be fitted with simplified models. In the case of effective diffusion (green) one can fit the recovery with a pure diffusion model and obtain an appearent diffusion coefficient which may be slowed down by binding interactions. In this regime k_{on} is very large while k_{off} can be varied over a wide range. This figure appears as "figure 3" in [169].

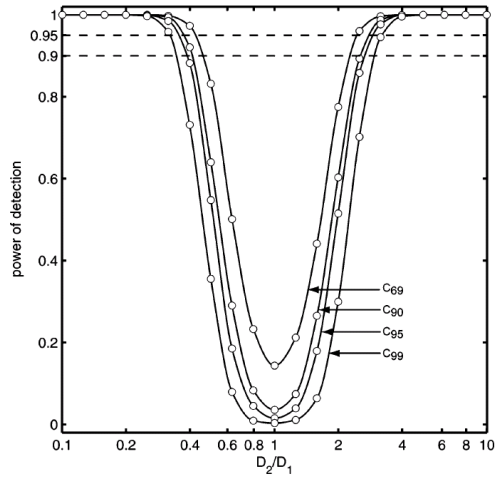

Figure 6.2: Prediction power of MLE approach as a function of the ratio $D_2/D_1$of diffusion coefficients in a trajectory with 200 time points at different confidence intervals. This figure appears in [123] as “Figure 4”.

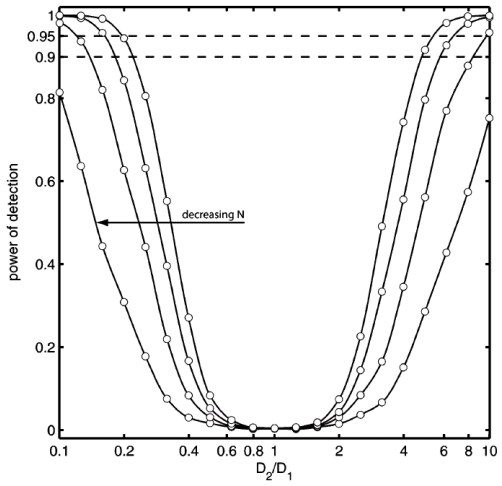

Figure 6.3: Prediction power of MLE approach as a function of the ratio $D_2/D_1$of diffusion coefficients. The track length N is 100, 80, 60, 40, respectively. This figure appears in [123] as "Figure 5".

6.2 Documentation

Compatibility note: All ImageJ macros were developed and tested with ImageJ version 1.36b and TurboReg version July25 2006 with Java 1.6 installed. All matlab scripts and functions were developed and tested using MATLAB version 7 (R14) with the packages image processing and statistics installed. It is recommended to configure ImageJ to use 1,3 GBytes of RAM by adding the run-time option "-mx1300m" to its configuration file (called "run" under Linux).

6.2.1 TurboReg macro for application of given transformations to an image series

Installation instructions

Installation is done by copy deployment. Copy the file "Batch_TurboReg2.txt" from the enclosed CD-ROM to the directory ~/ImageJ/plugins/Macros and restart ImageJ. "~" stands for your home directory.

Documentation

This macro applies rigid transformations necessary for registration of an image series (the reference stack) to another series of image stacks. The transformations must be created by using TurboReg once on a reference stack and storing them in a text file called "landmarks.txt". In the context of this work registration is performed either by invoking TurboReg from within ImageJ (for 4D image stacks) or by using the "Load_And_Register" macros described below on image time series (see chapters 6.2.3 and 6.2.2). Before starting the macro one single image and one image stack with the same pixel format must be open, because TurboReg requires this. The content of these stacks does not matter, because the macro reads in the source

images from the hard drive. After starting the macro the user is required to provide the following information in successive order: A directory containing source images (to be registered), a target directory for registered images, the number of time steps in the image stack, the number of z-Slices in the image stack and path and name of the landmarks file containing the transformation matrix. The transformations are then applied and the registered images are stored to the target directory. The source images are not changed. For detailed instructions on using TurboReg please refer to TurboReg `http://bigwww.epfl.ch/thevenaz/turboreg/`.

6.2.2 Loading and registration of spot-bleached nuclei (SP5)

Installation instructions

Installation is done by copy deployment. Copy the file "FRAP_Load_And_Register.txt" from the enclosed CD-ROM to the directory ~/ImageJ/plugins/Macros and restart ImageJ. "~" stands for your home directory.

Documentation

This macro loads the images generated by a Leica SP5 microscope's FRAP wizard into ImageJ and uses TurboReg to perform registration with affine transformations on them. The registered images are written to a user-specified directory. Note, the Leica SP5 uses a proprietary file format called ".lif". This macro expects a series of TIFF files. The images must be exported using the export function in Leica's LAS AF software prior to using this macro. The macro expects an image format of 256x256 pixels. This can be altered by editing the source file and setting the variables "width" and "height" to alternate values. After starting the macro the user is required to provide the following information in successive order: A directory containing source images (to be loaded and registered), a target

directory for registered images. The images are registered to the first image in the stack (usually this is the first pre-bleach image). The images in the source directory remain unchanged.

6.2.3 Loading and registration of half-bleached nuclei (SP5)

Installation instructions

Installation is done by copy deployment. Copy the file "FRAP_Load_And_Register_half.txt" from the enclosed CD-ROM to the directory ~/ImageJ/plugins/Macros and restart ImageJ. "~" stands for your home directory.

Documentation

This macro loads the images generated by a Leica SP5 microscope's FRAP wizard into ImageJ and uses TurboReg to perform rigid body registration on them. The registered images are written to a user-specified directory. Affine transformations do not work in case of half-bleached nuclei, because after bleaching the overall geometry has changed dramatically. Therefore, rigid body registration is preferred. Note, the Leica SP5 uses a proprietary file format called ".lif". This macro expects a series of TIFF files. The images must be exported using the export function in Leica's LAS AF software prior to using this macro. The macro expects an image format of 256x256 pixels. This can be altered by editing the source file and setting the variables "width" and "height" to alternate values. After starting the macro the user is required to provide the following information in successive order: A directory containing source images (to be loaded and registered), a target directory for registered images. The images are registered to the first image in the stack (usually this is the first pre-bleach image). The images in the source directory remain unchanged.

6.2.4 Creating masks for spot-bleached nuclei

Installation instructions

Installation is done by copy deployment. Copy the file "FRAP_Create_Masks.txt" from the enclosed CD-ROM to the directory ~/ImageJ/plugins/Macros and restart ImageJ. "~" stands for your home directory. This macro uses the FeatureJ package and the MultiThresholder plugins for ImageJ. The FeatureJ plug-in was written by Erik Meijering (`http://www.imagescience.org/meijering/software/featurej/`). The multi-thresholder plug-in was written by Kevin Baler (`http://rsb.info.nih.gov/ij/plugins/multi-thresholder.html`). These plugins must be installed for proper operation, detailed information is found on the author's web sites listed above.

Documentation

This macro automatically generates binary masks for the whole nucleus, the bleached and the unbleached region of a spot-bleached FRAP series. The image series must be loaded into ImageJ prior to execution. This is the case, for example, after using the "Load_And_Register" macros described above (chapter 6.2.2). It is assumed that the order of the images is pre-bleach images, bleached images, post-bleach images. After starting the macro the user is required to provide the following information in successive order: Number of pre-bleach images, number of bleach iterations a smoothing scale and a target directory for storing the mask images. The smoothing scale is used by the "FJ Edges" function in FeatureJ. It determines the amount of smoothing after edge detection. The default value is 4. Generally, this works well. In some cases the edge detection does not result in a closed form geometry (i.e. gaps in the nuclear boundary). The smoothing parameter can then be increased, however at the expense of precision. The mask images are displayed and written to the specified target directory.

6.2.5 Creating masks for half-bleached nuclei

Installation instructions

Installation is done by copy deployment. Copy the file "FRAP_Create_Masks_half.txt" from the enclosed CD-ROM to the directory ~/ImageJ/plugins/Macros and restart ImageJ. "~" stands for your home directory. This macro uses the FeatureJ package and the Multi-Thresholder plugins for ImageJ. The FeatureJ plug-in was written by Erik Meijering
(`http://www.imagescience.org/meijering/software/featurej/`).
The multi-thresholder plug-in was written by Kevin Baler
(`http://rsb.info.nih.gov/ij/plugins/multi-thresholder.html`).
These plugins must be installed for proper operation. Detailed information is found on the author's web sites listed above.

Documentation

This macro automatically generates binary masks for the whole nucleus, the bleached and the unbleached region of a half-bleached nucleus in a FRAP series. The image processing steps are adapted to the geometry and intensity distribution of a half-bleached nucleus compared to the situation found in spot-bleached nuclei (compare 6.2.4). The image series must be loaded into ImageJ prior to execution. This is the case, for example, after using the "Load_And_Register" macros described above (chapter 6.2.3). It is assumed that the order of the images is pre-bleach images, bleached images, post-bleach images. After starting the macro the user is required to provide the following information in successive order: Number of pre-bleach images, number of bleach iterations a smoothing scale and a target directory for storing the mask images. The smoothing scale is used by the "FJ Edges" function in FeatureJ. It determines the amount of smoothing after edge detection. The default value is 4. Generally, this works well. In

some cases the edge detection does not result in a closed form geometry (i.e. gaps in the nuclear boundary). The smoothing parameter can then be increased, however at the expense of precision. The mask images are displayed and written to the specified target directory.

6.2.6 Bleach correction for FRAP image series

Installation instructions

Installation is done by copy deployment. Copy the file "FRAP_normalize.txt" from the enclosed CD-ROM to the directory ~/ImageJ/plugins/Macros and restart ImageJ. "~" stands for your home directory. This macro uses ImageJ's built-in ROI manager.

Documentation

This macro performs a bleach correction as described in chapter 3.1.5. The FRAP image stack must be loaded into ImageJ. The macro uses ImageJ masks which must be defined prior to execution. The easiest way to this is by using rectangle select tool to select a background region and pressing "1", which adds it into the ROI manager. The nuclear outline can be generated by loading the binary mask for the whole nucleus, using the magic wand selection tool and pressing "1". It is mandatory to have the background ROI in position one, the whole nucleus in position 2 of the ROI manager. Also, make sure any result windows created by previous executions are closed. When prompted to allow the measurements, click 'Yes'. A new image stack called "normalized" will be created .

6.2.7 Segmentation of an image series

Installation instructions

Installation is done by copy deployment. Copy the file "Batch_FeatureJ_structure_stackwise.txt" from the enclosed CD-ROM to the directory ~/ImageJ/plugins/Macros and restart ImageJ. "~" stands for your home directory. This macro uses ImageJ's built-in ROI manager. This macro uses the FeatureJ package and the MultiThresholder plugins for ImageJ. This macro uses the Anisotropic diffusion 2D plugin written by Vladimir Pilny
(`http://rsbweb.nih.gov/ij/plugins/anisotropic-diffusion-2d.html`).
The FeatureJ plug-in was written by Erik Meijering
(`http://www.imagescience.org/meijering/software/featurej/`).
The multi-thresholder plug-in was written by Kevin Baler
(`http://rsb.info.nih.gov/ij/plugins/multi-thresholder.html`).
These plugins must be installed for proper operation. Detailed information is found on the author's web sites listed above.

Documentation

This macro segments a 4D image series containing single particle data to create binary masks of the particles. It operates on TIFF image files located in a user-specified directory and writes the binary images to a specified targed directory. After starting the macro the user is required to provide the following information in successive order: A directory containing source images (to be segmented), a target directory for registered images, a basename for the target images, the number of time steps in the image stack, the number of z-Slices in the image stack and channel number to be processed. The basename is a string which is added as a prefix to all file names of the processed images. The segmented images are written to the target directory.

6.2.8 Create TIKAL listfile

Installation instructions

Installation is done by copy deployment. Copy the file "Create_Tikal_Listfile.txt" from the enclosed CD-ROM to the directory ~/ImageJ/plugins/Macros and restart ImageJ. "~" stands for your home directory.

Documentation

This macro generates a list file containing paths and filenames to all images in a directory in a format which TIKAL can read. This enables TIKAL to load a 4D TIFF image series for single particle tracking. After starting the macro the user is required to provide the following information in successive order: A directory containing source images, a name for the listfile, the number of time steps in the image stack, the number of channels in the stack and the number of z-Slices in the image stack. The list file is generated in the source directory based on the images contained in it. The default name for the list file is "listfile.lst". There is no need to change this. Inside Tikal one uses the "Open 4D stack" dialog to specify the path to the listfile. Note, that images must be in 8-bit format.

6.2.9 Extract gray value information

Installation

Installation is done by copy deployment. Copy the file track2gray.m" from the enclosed CD-ROM to the matlab function directory. If the file is copied to another directory, use the "addpath" and "update function path" commands.

Signature

The following input and output variables are used:

```
function [grayvalueMatrix, pixelTrackMatrix, corr] =
    track2gray(graydataPath, graydataBasename,
   maskPath, maskBasename, trackMatrix, trafoMatrix,
    trackIndeces, voxelsize, zSlices)
```

Documentation

This matlab function uses binary masks corresponding to a 4D image stack to read gray value information for each object in the binary mask. Objects are defined by means of a matrix containing tracking data for each object. The output is a matrix containing gray values of each object over time. A correction for undesired bleaching is applied automatically by rescaling all subsequent images to the first image in the series. The intensity in the entire nucleus is used for this purpose. The following table summarizes the meaning of all variables:

Variable name	Description	Specified / generated by
Output variables		
grayvalueMatrix	mxn matrix containing gray value data for each object (e.g. PML body), where m equals number of time steps, n equals number of objects.	track2gray.m

Variable name	Description	Specified / generated by
pixelTrackMatrix	mx3n matrix containing x-, y- and z-coordinates to each object (e.g. PML body). m equals number of time steps, n equals number of objects. This matrix outputs the pixel coordinates to each object over time for later reference.	
corr	Column vector with m elements containing the correction factors for bleach correction for reference. m equals the number of time steps.	
Input variables		
graydataPath	Path to grayvalue image files (e.g. PML bodies)	User
graydataBasename	Leading string of each gray data image file.	User
maskPath	Path to binary masks of grayvalue images (e.g. PML bodies)	User
maskBasename	Leading string of each mask image file.	User

Variable name	Description	Specified / generated by
trackMatrix	mx3n matrix containing physical x-, y- and z-coordinates to each object (e.g. PML body) scaled in micrometers. m equals number of time steps, n equals number of objects. Each object thus consists of a column vector with 3 columns for x-, y- and z-coordinates, respectively.	msdScript.m
trafoMatrix	mx3n matrix containing x-, y- and z- transformations to each object (e.g. PML body). m equals number of time steps, n equals number of objects. Each object thus consists of a column vector with 3 columns for x-, y- and z-coordinates, respectively. This matrix contains any (optional) transformations applied by msdScript.m, such as transformation to the center of mass per time step. If such transformations were applied they need to be reversed in track2gray.m in order to correctly assign gray value information.	msdScript.m

Variable name	Description	Specified / generated by
trackIndeces	mxn binary matrix containing the range of values for each track. m equals number of time steps, n equals number of objects. This matrix allows the user to specify the usable data range for each object, since all trajectories can differ in length. All elements set to 1 are used, while all zero elements in trackIndeces are ignored.	User (during first execution of msdMatrix.m)
voxelsize	3-element row vector specifying the x-, y- and z-dimension of each pixel scaled in micrometers.	User (during first execution of msdMatrix.m)
zSlices	Number of z sections in image stack	User

6.2.10 Calculation of mean square displacement (MSD)

Installation

Installation is done by copy deployment. Copy the file "msd.m" from the enclosed CD-ROM to the matlab function directory. If the file is copied to another directory, use the "addpath" and "update function path" commands.

Signature

The following input and output variables are used:

```
function outputVal = msd(trajectory)
```

Documentation

This matlab function computes the mean square displacement of a trajectory provided as a column vector. It is called by msdScript.m for this purpose. The following table summarizes the meaning of all variables:

Variable name	Description	Specified / generated by
Output variables		
outputVal	Column vector containing mean square displacements. Consecutive entries represent increasing lag times.	msd.m
Input variables		
trajectory	mx3 matrix with x-, y- and z-coordinates of object, respectively. m equals the number of time steps.	msdScript.m

6.2.11 MSD curve fitting and classification of movement type

Installation

Installation is done by copy deployment. Copy the files “msdScript.m”, “msd.m”, “checkIndex.m”, “fitcurve.m”, “lerp.m”, “gaussianfilter_old.m”, “pearsonsr.m”, “displacement.m”, “meanDisplacement.m”, “eudistance.m” and “diffusion.m” from the enclosed CD-ROM to the matlab function directory. If the file is copied to another directory, use the “addpath” and “update function path” commands.

Signature

The following input and output variables are used:

```
[trackMatrix, msdMatrix, estimates, fitMatrix,
   trafoMatrix, totalGrayValueMatrix,
   physicalVolumeMatrix, voxelNumberMatrix, M, N,
   weight, trackUsedInClassification,
   numberOfTracksPerPhase, alphaMatrix] = msdScript(
   ypi, trackNumbers, trackIndeces, timeStamp, ypi2,
    trackPhases, startparameters, dimension,
   voxelsize)
```

Documentation

This matlab script processes complete sets of 3D trajectories, such as generated by TIKAL, to compute mean square displacements and fit them by non-linear regression analysis. The data fitting is used to classify trajectories with regard to their anomality (sub- or superdiffusion). The script can apply transformations, such as translation to all particles’ center of mass

(COM) or a user-specified transformation matrix. The key concept is to provide an interface to all underlying functions and to automate the analysis for a complete tracking data set. The analysis results are displayed graphically as well as output as MATLAB variables. The following table summarizes the meaning of all variables and control parameters:

Variable name	Description	Specified / generated by
Output variables		
trackMatrix	Mx3N matrix containing Cartesian coordinates of trajectories read in from 'ypi', where M stands for the number of time steps and N stands for the number of tracked objects.	msdScript.m
msdMatrix	MxN matrix containing mean square displacement data for each object. M stands for the length of time lag coordinate and N signifies the number of tracked objects.	msdScript.m
estimates	MxNxO matrix containing estimated parameters from curve fitting (D, α or D, α, y-axis intercept). M stands for the number of objects, N is the number of parameters (2 or 3) and N stands for the number of phases.	msdScript.m

Variable name	Description	Specified / generated by
fitMatrix	MxN matrix with curve fitting data for mean square displacement plots. M is the length of the lag time coordinate and N stands for the number of tracked objects.	msdScript.m
trafoMatrix	Mx3 matrix with transformations applied to tracks. If the transformations where read from a file they are output as in the file, if 'COM' transformations where defined they are output here for reference.	msdScript.m or read from file.
totalGrayValueMatrix	MxN matrix containing gray values read from TIKAL tracking file. TIKAL can read gray value data from a reference channel (such as chromatin counter-stain). Caution: If manual corrections after the automatic particle tracking were necessary in TIKAL, there are gaps. Refer to track2gray.m to re-read the gray value data from image series of the reference channel.	read from file.

Variable name	Description	Specified / generated by
physicalVolumeMatrix	MxN matrix containing physical volume of each object over time as read from TIKAL tracking file. TIKAL measures the physical volume of each object. Caution: If manual corrections after the automatic particle tracking were necessary in TIKAL, there are gaps.	read from file
volumeNumberMatrix	MxN matrix containing the number of voxels of each object over time as read from TIKAL tracking file. TIKAL adds the voxel number of each object using a binary mask of each object. Caution: If manual corrections after the automatic particle tracking were necessary in TIKAL, there are gaps.	read from file
M	3xN matrix containing proportional amounts of each movement type (directed, diffusive or obstructed) per phase, N being the number of phases.	msdScript.m
N	3xM matrix containing the amounts of each movement type per phase, M being the number of phases.	msdScript.m

Variable name	Description	Specified / generated by
weight	MxN matrix containing the weights used in movement classification. M stands for the number of objects, N for the number of phases.	msdScript.m
tracksUsedInClassification	MxN matrix specifying which (sub-)tracks where used in classification. A quality criterion for curve fitting of MSD data is set using the variable 'minPearson' inside 'msdScript.m' which specifies a threshold for the Pearson correlation coefficient between MSD data and fit. M stands for the number of objects, N stands for the phase. Therefore, in multi-phase classification N > 1.	msdScript.m
numberOfTracksPerPhase	Sum over tracksUsedInClassification	msdScript.m
alphaMatrix	MxN matrix containing the estimated alpha coefficients with M signifying the number of objects and N being the number of phases.	msdScript.m
Input variables		

Variable name	Description	Specified / generated by
ypi	Base name to tracking data. msdScript expects a set of ASCII files of the form 'ypiN.txt', where 'N' stands for a number specified by 'trackNumbers'. 'ypi' can contain full path information including the base name in a string. If no path is specified, msdScript expects to find the files in its current working directory.	user
trackNumbers	Column vector containing the numbers of tracks to include in the analysis. This allows the user to select which files are included or omitted from the analysis.	user
trackIndeces	MxN matrix specifying which portions of tracks to include in the analysis, where M stands for number of time steps, N stands for number of trajectories. N must match the length of 'trackNumbers'. This allows the user to specify which time steps of the selected tracks are included or omitted from the analysis.	user

Variable name	Description	Specified / generated by
timeStamp	Column vector containing time stamp information for each time step in the trajectory, scaled in seconds. This variable must be created before calling 'msdScript.m', for example by loading it from a file.	user
ypi2	Variable specifying if or which type of transformation is to be applied to the trajectories. Three possible values are allowed: 1) File name to an ASCII file with an Mx3 matrix for transformations. Such transformations could, for example, be created by image registration with TurboReg. 'ypi' can contain full path information including the base name in a string. If no path is specified, msdScript expects to find the files in its current working directory. 2) 'COM' which stands for center of mass. All objects in each time step will be translated to their common COM. 3) Empty set. If nothing is specified, no transformations will be carried out.	user

Variable name	Description	Specified / generated by
trackPhases	Specifies if multi-phase analysis is carried out. Multi-phase analysis means that each track is subdivided into shorther subtracks. For each subtrack a full MSD analysis and movement classification is carried out. 'trackPhases' is a column vector containing M elements equal to the number of time steps. Possible values are all natural numbers smaller than the length of the trajectories. If all elements are equal to one no multi-phase analysis is carried out. This is an optional argument. Default is '1'.	user
startparameters	Row vector containing start parameters for non-linear curve fitting of MSD tracks. The first element is the diffusion coefficient, the second element is the anomalous diffusion parameter. An optional third element is the start value for a variable y-axis intercept. If no third element is specified, the y-axis intercept is fixed to zero. 'startparameters' is an optional argument. Default is [1 1].	user

Variable name	Description	Specified / generated by
dimension	Scalar specifying dimensionality of tracking data. Possible values are 2 or 3. Optional parameter. Default is 2.	user
voxelsize	3-element row vector with physical dimensions along x-, y- and z-coordinates in micrometers. Optional parameter. Default is [1 1 1].	user

6.2.12 Simulation of 1D-random walks

Installation

Installation is done by copy deployment. Copy the file "randomwalk1D.m" from the enclosed CD-ROM to the matlab function directory. If the file is copied to another directory, use the "addpath" and "update function path" commands.

Signature

The following input and output variables are used:

```
function [trajectory, displacements] = randomwalk1D(
   numberOfTimesteps, D, alpha, deltaT, startpos)
```

Documentation

This matlab function implements a one-dimensional diffusion model which simulates a random walk according to the microscopic theory of diffusion

([21]). Anomalous diffusion is available, as well as a defined start position. The latter makes it possible to use the last spatial coordinate of an existing trajectory as the start position of another one to generate trajectories with fluctuating properties (such as diffusion coefficient). The following table summarizes the meaning of all variables:

Variable name	Description	Specified / generated by
Output variables		
trajectory	Column vector containing trajectory of 1D random walk with 'numberOfTimeSteps' elements.	randomwalk1D.m
displacements	Column vector containing the displacemtens of the random walk data, equivalent to the discreet first deviation of the trajectory. Its lenght is 'numberOfTimeSteps' - 1.	randomwalk1D.m
Input variables		
numberOfTimesteps	Skalar specifying the length of the random walk.	user
D	Diffusion coefficient for random walk.	user
alpha	Coefficient of anomalous diffusion.	user
deltaT	Time interval of random walk.	user
startpos	Start position of random walk.	user

6.2.13 Critical region

Installation

Installation is done by copy deployment. Copy the files “criticalRegion.m” and “critical_region.mat” from the enclosed CD-ROM to the matlab function directory. If the file is copied to another directory, use the “addpath” and “update function path” commands.

Signature

The following input and output variables are used:

```
function C = criticalRegion(N, alpha)
```

Documentation

This matlab function’s output is the critical region at a given sample size N and a confidence interval α. The data was originally created using NOE’s algorithm and published in tabulated form in [189]. The intermediate values between the tabulated values were interpolated with a spline function. Because of this it should only be used for N > 10. The function values are read from a matlab variable ’critical_region.mat’ according to user input. The following table summarizes the meaning of all variables:

Variable name	Description	Specified / generated by
Output variables		
C	Scalar value for critical region.	criticalRegion.m
Input variables		
N	Sample size for critical region.	user

Variable name	Description	Specified / generated by
alpha	Confidence interval for critical region. α can have the following values as strings '0.99', '0.95', '0.90', '0.69'.	user

6.2.14 Log-Likelihood ratio

Installation

Installation is done by copy deployment. Copy the files "logLikelihoodRatio.m" and "maximumLikelihoodEstimation.m" from the enclosed CD-ROM to the matlab function directory. If the file is copied to another directory, use the "addpath" and "update function path" commands.

Signature

The following input and output variables are used:

```
function [llr, breakpoints, breakpoints_b] =
   logLikelihoodRatio(x, deltaT, lastXmax, alpha)
```

Documentation

This matlab function computes the log-likelihood ratio of a given displacement vector x (i.e. displacements of a trajectory). The user specifies the time interval and a confidence interval for the computation of the critical region. The function is implemented recursively and terminates if the length of a subtrack is zero. Until then the function passes the 'lastXmax'

parameter to the next recursive call which is used to partition the trajectory into two sub-tracks. The following table summarizes the meaning of all variables:

Variable name	Description	Specified / generated by
Output variables		
llr	Column vector with log-likelihood ratios of given displacements.	logLikelihoodRatio.m
breakpoints	Row vector with breakpoints found by all runs of "logLikelihoodRatio.m" to partition the trajectory into sub-tracks.	logLikelihoodRatio.m
breakpoints_b	Same as 'breakpoints'. Used for experimental functionality during development. Now it is deprecated and only included for compatibility with existing code.	logLikelihoodRatio.m
Input variables		
x	Column vector containing displacements of a given trajectory.	user
deltaT	Time interval of trajectory.	user
lastXmax	Position of maximum in previous run of "logLikelihoodRatio.m". For the first call of the function 'lastXmax' must be equal to 1.	user
alpha	Confidence interval for computation of critical region. α can have the following values as strings '0.99', '0.95', '0.90', '0.69'.	user

6.2.15 Detection of diffusive changes

Installation

Installation is done by copy deployment. Copy the files "MLE_findDiffChangeInterpolated.m", "allocate2DCellArray.m", "weedOutZeros.m", "proximityFilter.m", "maximumLikelihoodEstimation.m" and "estimateAlpha.m" from the enclosed CD-ROM to the matlab function directory. If the file is copied to another directory, use the "addpath" and "update function path" commands.

Signature

The following input and output variables are used:

```
function [iD, iLlr, iBP, iMsqDpl, iTimeStampIndeces,
    iGraydata, vecD, vecA, vecG, vecResnorm,
   veloMatrix, alphaMatrix, resnormMatrix, fitMatrix
   ] = MLE_findDiffChangeInterpolated(trackMatrix,
   trackIndeces, timeStamp, alpha,
   interpolationDepth, interpolationType,
   proximityTolerance, grayvalueMatrix)
```

Documentation

This matlab function is a wrapper which computes diffusion coefficients (D), log-likelihood ratios (llr) and breakpoints (bp) for all sub-tracks in a tracking experiment. It also outputs D, llr, bp and gray values in the chromatin channel as a function of time. Interpolation of tracking data is available. Since the critical region is only available for tracks <= 1000 time steps, longer tracks are automatically partitioned into smaller ones, the computations are performed and the pieces are concatenated afterwards. A treatment of boundary artifacts in finding break points is implemented. Break

points which are found very close to one another can be binned according to a user-specified binning width. The function also calls "msd.m" to compute mean square displacements of each subtrack and performs curve fitting on them to determine the alpha coefficient of anomalous diffusion. The following table summarizes the meaning of all variables:

Variable name	Description	Specified / generated by
Output variables		
iD	MxN cell array containing diffusion coefficients for all sub-tracks in tracking experiment. M is the number of tracks, N the number of break points in each track (i.e. number of sub-tracks - 1).	MLE_findDiff-ChangeInter-polated.m
iLlr	MxNxQ cell array containing log-likelihood ratios as a function of time for each sub-track. M ist the number of tracks, N the number of sub-trakcs and Q the number of time steps per sub-track.	MLE_findDiff-ChangeInter-polated.m
iBP	MxNxQ cell array containing break points as a function of time for each sub-track. M ist the number of tracks, N the number of sub-tracks and Q the number of break points per sub-track.	MLE_findDiff-ChangeInter-polated.m

Variable name	Description	Specified / generated by
iMsqDpl	MxN cell array mean square displacements for all sub-tracks in tracking experiment. M is the number of tracks, N the number of break points in each track (i.e. number of sub-tracks - 1).	MLE_findDiff-ChangeInter-polated.m
iTimeStampIndeces	MxN cell array containing the time stamp information for all sub-tracks corresponding to 'iMspDpl' in tracking experiment. M is the number of tracks, N the number of break points in each track (i.e. number of sub-tracks - 1).	MLE_findDiff-ChangeInter-polated.m
iGraydata	MxN cell array containing gray value data for all sub-tracks in tracking experiment as a function of the time steps specified in 'iTimeStampIndeces'. M is the number of tracks, N the number of break points in each track (i.e. number of sub-tracks - 1).	MLE_findDiff-ChangeInter-polated.m
vecD	MxN Matrix containing plottable version of diffusion coefficients per trajectory, with M as the number of time steps and N as the track number.	MLE_findDiff-ChangeInter-polated.m

Variable name	Description	Specified / generated by
vecA	MxN Matrix containing plottable version of anomalous diffusion coefficients per trajectory, with M as the number of time steps and N as the track number.	MLE_findDiff-ChangeInter-polated.m
vecG	MxN Matrix containing plottable version of gray values in chromatin channel per trajectory, with M as the number of time steps and N as the track number.	MLE_findDiff-ChangeInter-polated.m
vecResnorm	MxN Matrix containing plottable version of error residuals from MSD curve fitting per trajectory, with M as the number of time steps and N as the track number.	MLE_findDiff-ChangeInter-polated.m
veloMatrix	MxN cell array containing velocities over time for each sub-track. M is the number of trajectories, N the number of sub-tracks in each experiment.	MLE_findDiff-ChangeInter-polated.m
alphaMatrix	MxN cell array anomalous diffusion coefficients over time for each sub-track. M is the number of trajectories, N the number of sub-tracks in each experiment.	MLE_findDiff-ChangeInter-polated.m
resnormMatrix	MxN cell array error residuals for each sub-track. M is the number of trajectories, N the number of sub-tracks in each experiment.	MLE_findDiff-ChangeInter-polated.m

Variable name	Description	Specified / generated by
fitMatrix	MxN cell array containing fitted MSD data for each sub-track. M is the number of trajectories, N the number of sub-tracks in each experiment.	MLE_findDiff-ChangeInter-polated.m
Input variables		
trackMatrix	mx3n matrix containing physical x-, y- and z-coordinates to each object (e.g. PML body) scaled in micrometers. m equals number of time steps, n equals number of objects. Each object thus consists of a column vector with 3 columns for x-, y- and z-coordinates, respectively.	user
trackIndeces	MxN matrix specifying which portions of tracks to include in the analysis, where M stands for number of time steps, N stands for number of trajectories. N must match the length of 'trackNumbers'. This allows the user to specify which time steps of the selected tracks are included or omitted from the analysis.	user

Variable name	Description	Specified / generated by
timeStamp	Column vector containing time stamp information for each time step in the trajectory, scaled in seconds. This variable must be created before calling 'msdScript.m', for example by loading it from a file.	user
alpha	Confidence interval for computation of critical region. α can have the following values as strings '0.99', '0.95', '0.90', '0.69'.	user
interpolationDepth	Scalar specifying the interpolation depth for tracking data. Each track is interpolationDepth times longer after interpolation.	user
interpolationType	String variable which determines the method for interpolation of trajectories. All types supported by the standard MATLAB function "interp1.m" are allowed. Default is 'linear'. For more information refer to help file of "interp1.m".	user

Variable name	Description	Specified / generated by
proximityTolerance	Scalar value determining the bin size (number of time steps) for break point detection. Break points closer than 'proximityTolerance' are combined and replaced by their median value. Default is 7 time steps.	user
grayvalueMatrix	MxN matrix containing gray value data for each trajectory as read from a reference channel. M stands for number of time steps, N for the number of objects.	user or "track2gray.m"

Bibliography

[1] 7th International Conference on Pattern Recognition. *Velocity estimation from image sequences with second order differential operators*, 1984.

[2] S.R. Adams and R.Y. Tsien. Preparation of the membrane-permeant biarsenicals FlAsH-EDT2 and ReAsH-EDT2 for fluorescent labeling of tetracysteine-tagged proteins. *Nat Protoc*, 3:1527–1534, 2008.

[3] E. H. Adelson and J. R. Bergen. Spatiotemporal energy models for the perception of motion. *J. Opt. Soc. Am.*, 2(2):284–299, 1985.

[4] H.W. Ai, N.C. Shaner, Z. Cheng, R.Y. Tsien, and R.E. Campbell. Exploration of new chromophore structures leads to the identification of improved blue fluorescent proteins. *Biochemistry*, 46:5904–5910, May 2007.

[5] Bruce Alberts, Alexander Johnson, Julian Lewis, Martin Raff, Keith Roberts, and Peter Walter. *Molecular Biology of the Cell*. Garland Science, 4th edition, 2002.

[6] H. Albiez, M. Cremer, C. Tiberi, L. Vecchio, L. Schermelleh, S. Dittrich, K. Küpper, B. Joffe, T. Thormeyer, J. von Hase, S. Yang, K. Rohr, H. Leonhardt, I. Solovei, C. Cremer, S. Fakan, and T. Cremer. Chromatin domains and the interchromatin compartment form structurally defined and functionally interacting nuclear networks. *Chromosome Res.*, 14:707–733, 2006.

[7] P. Anandan. A computational framework and an algorithm for the measurement of visual motion. *Int. J. Comp. Vision*, 2:283–319, 1989.

[8] S. Arseneau. Structure tensor - tutorial and demonstration of the uses of structure tensors using gradient representation, 2006.

[9] Y. Asakawa and E. Gotoh. A method for detecting sister chromatid exchanges using prematurely condensed chromosomes and immunogold-silver staining. *Mutagenesis*, 12:175–177, May 1997.

[10] D. Axelrod, D.E. Koppel, J. Schlessinger, E. Elson, and W.W. Webb. Mobility measurement by analysis of fluorescence photobleaching recovery kinetics. *Biophys. J.*, 16:1055–1069, Sep 1976.

[11] D. Axelrod, P. Ravdin, D.E. Koppel, J. Schlessinger, W.W. Webb, E.L. Elson, and T.R. Podleski. Lateral motion of fluorescently labeled acetylcholine receptors in membranes of developing muscle fibers. *Proc. Natl. Acad. Sci. U.S.A.*, 73:4594–4598, Dec 1976.

[12] Christian Peter Bacher. *Computational imaging of dynamic nuclear processes in living somatic and germ line cells*. PhD thesis, Universität Heidelberg, 2005.

[13] C.P. Bacher, M. Guggiari, B. Brors, S. Augui, P. Clerc, P. Avner, R. Eils, and E. Heard. Transient colocalization of X-inactivation centres accompanies the initiation of X inactivation. *Nat. Cell Biol.*, 8:293–299, Mar 2006.

[14] C.P. Bacher, M. Reichenzeller, C. Athale, H. Herrmann, and R. Eils. 4-D single particle tracking of synthetic and proteinaceous microspheres reveals preferential movement of nuclear particles along chromatin - poor tracks. *BMC Cell Biol.*, 5:45, Nov 2004.

[15] K. Bacia and P. Schwille. A dynamic view of cellular processes by in vivo fluorescence auto- and cross-correlation spectroscopy. *Methods*, 29:74–85, Jan 2003.

[16] K. G. Baler. Multithresholder, 2005.

[17] I. N. Bankman. *Handbook of medical imaging: Processing and analysis*. Academic Press, 2000.

[18] J.L. Barra, L. Rhounim, J.L. Rossignol, and G. Faugeron. Histone H1 is dispensable for methylation-associated gene silencing in Ascobolus immersus and essential for long life span. *Mol. Cell. Biol.*, 20:61–69, Jan 2000.

[19] F. Bassermann, C. Peschel, and J. Duyster. Mitotic entry: a matter of oscillating destruction. *Cell Cycle*, 4:1515–1517, Nov 2005.

[20] J. Beaudouin, F. Mora-Bermúdez, T. Klee, N. Daigle, and J. Ellenberg. Dissecting the contribution of diffusion and interactions to the mobility of nuclear proteins. *Biophys. J.*, 90:1878–1894, Mar 2006.

[21] Howard C. Berg. *Random walks in biology*. Princeton Paperbacks, 1993.

[22] R. Bernardi, P.P. Scaglioni, S. Bergmann, H.F. Horn, K.H. Vousden, and P.P. Pandolfi. PML regulates p53 stability by sequestering Mdm2 to the nucleolus. *Nat. Cell Biol.*, 6:665–672, Jul 2004.

[23] D. Bhattacharya, A. Mazumder, S.A. Miriam, and G.V. Shivashankar. EGFP-tagged core and linker histones diffuse via distinct mechanisms within living cells. *Biophys. J.*, 91:2326–2336, Sep 2006.

[24] F.M. Boisvert, M.J. Hendzel, and D.P. Bazett-Jones. Promyelocytic leukemia (PML) nuclear bodies are protein structures that do not accumulate RNA. *J. Cell Biol.*, 148:283–292, Jan 2000.

[25] K. Braeckmans, L. Peeters, N.N. Sanders, S.C. De Smedt, and J. Demeester. Three-dimensional fluorescence recovery after photobleaching with the confocal scanning laser microscope. *Biophys. J.*, 85:2240–2252, Oct 2003.

[26] M.R. Branco and A. Pombo. Intermingling of chromosome territories in interphase suggests role in translocations and transcription-dependent associations. *PLoS Biol.*, 4:e138, May 2006.

[27] D.T. Brown. Histone H1 and the dynamic regulation of chromatin function. *Biochem. Cell Biol.*, 81:221–227, Jun 2003.

[28] D.T. Brown, T. Izard, and T. Misteli. Mapping the interaction surface of linker histone H1(0) with the nucleosome of native chromatin in vivo. *Nat. Struct. Mol. Biol.*, 13:250–255, Mar 2006.

[29] K.E. Brown, J. Baxter, D. Graf, M. Merkenschlager, and A.G. Fisher. Dynamic repositioning of genes in the nucleus of lymphocytes preparing for cell division. *Mol. Cell*, 3:207–217, Feb 1999.

[30] K.E. Brown, S.S. Guest, S.T. Smale, K. Hahm, M. Merkenschlager, and A.G. Fisher. Association of transcriptionally silent genes with Ikaros complexes at centromeric heterochromatin. *Cell*, 91:845–854, Dec 1997.

[31] R. Brown. *The Miscellaneous Botanical Works of Robert Brown*. R. Hardwicke, 1866.

[32] P.A. Bubulya, K.V. Prasanth, T.J. Deerinck, D. Gerlich, J. Beaudouin, M.H. Ellisman, J. Ellenberg, and D.L. Spector. Hypophosphorylated SR splicing factors transiently localize around active nucleolar organizing regions in telophase daughter nuclei. *J. Cell Biol.*, 167:51–63, Oct 2004.

[33] M. Bustin, F. Catez, and J.H. Lim. The dynamics of histone H1 function in chromatin. *Mol. Cell*, 17:617–620, Mar 2005.

[34] D. Cai, K.J. Verhey, and E. Meyhöfer. Tracking single Kinesin molecules in the cytoplasm of mammalian cells. *Biophys. J.*, 92:4137–4144, Jun 2007.

[35] J. Cannny. *A Computational Approach to Edge Detection*, volume 8. 1986.

[36] G. Carrero, E. Crawford, M.J. Hendzel, and G. de Vries. Characterizing fluorescence recovery curves for nuclear proteins undergoing binding events. *Bull. Math. Biol.*, 66:1515–1545, Nov 2004.

[37] G. Carrero, D. McDonald, E. Crawford, G. de Vries, and M.J. Hendzel. Using FRAP and mathematical modeling to determine the in vivo kinetics of nuclear proteins. *Methods*, 29:14–28, Jan 2003.

[38] Y.C. Chen, C. Kappel, J. Beaudouin, R. Eils, and D.L. Spector. Live cell dynamics of promyelocytic leukemia nuclear bodies upon entry into and exit from mitosis. *Mol. Biol. Cell*, 19:3147–3162, Jul 2008.

[39] R.W. Ching, G. Dellaire, C.H. Eskiw, and D.P. Bazett-Jones. PML bodies: a meeting place for genomic loci? *J. Cell. Sci.*, 118:847–854, Mar 2005.

[40] J.R. Chubb and W.A. Bickmore. Considering nuclear compartmentalization in the light of nuclear dynamics. *Cell*, 112:403–406, Feb 2003.

[41] D. Cmarko, P.J. Verschure, T.E. Martin, M.E. Dahmus, S. Krause, X.D. Fu, R. van Driel, and S. Fakan. Ultrastructural analysis of transcription and splicing in the cell nucleus after bromo-UTP microinjection. *Mol. Biol. Cell*, 10:211–223, Jan 1999.

[42] D. Cmarko, P.J. Verschure, L.I. Rothblum, D. Hernandez-Verdun, F. Amalric, R. van Driel, and S. Fakan. Ultrastructural analysis of nucleolar transcription in cells microinjected with 5-bromo-UTP. *Histochem. Cell Biol.*, 113:181–187, Mar 2000.

[43] Geoffrey M. Cooper. *The Cell - A Molecular Approach*. Oxford University Press, 2nd edition, 2000.

[44] J. Crank. *Diffusion and chemical reaction.* Oxford University Press, 1975.

[45] T. Cremer and C. Cremer. Chromosome territories, nuclear architecture and gene regulation in mammalian cells. *Nat. Rev. Genet.*, 2:292–301, Apr 2001.

[46] G. Dellaire and D.P. Bazett-Jones. PML nuclear bodies: dynamic sensors of DNA damage and cellular stress. *Bioessays*, 26:963–977, Sep 2004.

[47] G. Dellaire, C.H. Eskiw, H. Dehghani, R.W. Ching, and D.P. Bazett-Jones. Mitotic accumulations of PML protein contribute to the re-establishment of PML nuclear bodies in G1. *J. Cell. Sci.*, 119:1034–1042, Mar 2006.

[48] M.M. Duggan and J.O. Thomas. Two DNA-binding sites on the globular domain of histone H5 are required for binding to both bulk and 5 S reconstituted nucleosomes. *J. Mol. Biol.*, 304:21–33, Nov 2000.

[49] M. Dundr, M.D. Hebert, T.S. Karpova, D. Stanek, H. Xu, K.B. Shpargel, U.T. Meier, K.M. Neugebauer, A.G. Matera, and T. Misteli. In vivo kinetics of Cajal body components. *J. Cell Biol.*, 164:831–842, Mar 2004.

[50] E. Duprez, A.J. Saurin, J.M. Desterro, V. Lallemand-Breitenbach, K. Howe, M.N. Boddy, E. Solomon, H. de Thé, R.T. Hay, and P.S. Freemont. SUMO-1 modification of the acute promyelocytic leukaemia protein PML: implications for nuclear localisation. *J. Cell. Sci.*, 112 (Pt 3):381–393, Feb 1999.

[51] M. Durante, Y. Furusawa, and E. Gotoh. A simple method for simultaneous interphase-metaphase chromosome analysis in biodosimetry. *Int. J. Radiat. Biol.*, 74:457–462, Oct 1998.

[52] M. Ehrenberg and R. Rigler. Fluorescence correlation spectroscopy applied to rotational diffusion of macromolecules. *Q. Rev. Biophys.*, 9:69–81, Feb 1976.

[53] M.V. Ehrensperger, C. Hanus, C. Vannier, A. Triller, and M. Dahan. Multiple association states between glycine receptors and gephyrin identified by SPT analysis. *Biophys. J.*, 92:3706–3718, May 2007.

[54] R. Eils, D. Gerlich, W. Tvaruskó, D.L. Spector, and T. Misteli. Quantitative imaging of pre-mRNA splicing factors in living cells. *Mol. Biol. Cell*, 11:413–418, Feb 2000.

[55] A. Einstein. Über die von der molekularkinetischen theorie der wärme geforderte bewegung von in ruhenden flüssigkeiten suspendierten teilchen. *Annalen der Physik*, 17:549–560, 1905.

[56] M. Elsner, H. Hashimoto, J.C. Simpson, D. Cassel, T. Nilsson, and M. Weiss. Spatiotemporal dynamics of the COPI vesicle machinery. *EMBO Rep.*, 4:1000–1004, Oct 2003.

[57] C.H. Eskiw, G. Dellaire, and D.P. Bazett-Jones. Chromatin contributes to structural integrity of promyelocytic leukemia bodies through a SUMO-1-independent mechanism. *J. Biol. Chem.*, 279:9577–9585, Mar 2004.

[58] C.H. Eskiw, G. Dellaire, J.S. Mymryk, and D.P. Bazett-Jones. Size, position and dynamic behavior of PML nuclear bodies following cell stress as a paradigm for supramolecular trafficking and assembly. *J. Cell. Sci.*, 116:4455–4466, Nov 2003.

[59] R.D. Everett. DNA viruses and viral proteins that interact with PML nuclear bodies. *Oncogene*, 20:7266–7273, Oct 2001.

[60] R.D. Everett, P. Lomonte, T. Sternsdorf, R. van Driel, and A. Orr. Cell cycle regulation of PML modification and ND10 composition. *J. Cell. Sci.*, 112 (Pt 24):4581–4588, Dec 1999.

[61] D. J. Fleet. *Measurement of Image Velocity*. Kluwer Academic Publishers, Dordrecht, 1992.

[62] D. J. Fleet and A. D. Jepson. Computation of component image velocity from local phase information. *Int. J. Comp. Vision*, 5:77–104, 1990.

[63] R.W. Fuller, W.W. Bromer, H.D. Snoddy, and J.C. Baker. Regulation of enzyme activity by glucagon: increased hormonal activity of iodinated glucagon. *Adv. Enzyme Regul.*, 13:201–215, 1975.

[64] A.B. Fulton. How crowded is the cytoplasm? *Cell*, 30:345–347, Sep 1982.

[65] A.J. García-Sáez and P. Schwille. Single molecule techniques for the study of membrane proteins. *Appl. Microbiol. Biotechnol.*, 76:257–266, Aug 2007.

[66] D. Gerlich, J. Beaudouin, M. Gebhard, J. Ellenberg, and R. Eils. Four-dimensional imaging and quantitative reconstruction to analyse complex spatiotemporal processes in live cells. *Nat. Cell Biol.*, 3:852–855, Sep 2001.

[67] D. Gerlich, J. Beaudouin, B. Kalbfuss, N. Daigle, R. Eils, and J. Ellenberg. Global chromosome positions are transmitted through mitosis in mammalian cells. *Cell*, 112:751–764, Mar 2003.

[68] B.N. Giepmans, S.R. Adams, M.H. Ellisman, and R.Y. Tsien. The fluorescent toolbox for assessing protein location and function. *Science*, 312:217–224, Apr 2006.

[69] Evgeny Gladilin, Constantin Kappel, and Roland Eils. Motion detection and pattern tracking in microscopical images using phase correlation approach. *Proc. of SPIE*, 6512:65121V, 2007.

[70] S.M. Görisch, M. Wachsmuth, C. Ittrich, C.P. Bacher, K. Rippe, and P. Lichter. Nuclear body movement is determined by chromatin accessibility and dynamics. *Proc. Natl. Acad. Sci. U.S.A.*, 101:13221–13226, Sep 2004.

[71] S.M. Görisch, M. Wachsmuth, C. Ittrich, C.P. Bacher, K. Rippe, and P. Lichter. Nuclear body movement is determined by chromatin accessibility and dynamics. *Proc. Natl. Acad. Sci. U.S.A.*, 101:13221–13226, Sep 2004.

[72] K.L. Gould and P. Nurse. Tyrosine phosphorylation of the fission yeast cdc2+ protein kinase regulates entry into mitosis. *Nature*, 342:39–45, Nov 1989.

[73] B.A. Griffin, S.R. Adams, and R.Y. Tsien. Specific covalent labeling of recombinant protein molecules inside live cells. *Science*, 281:269–272, Jul 1998.

[74] Y. Gruenbaum, A. Margalit, R.D. Goldman, D.K. Shumaker, and K.L. Wilson. The nuclear lamina comes of age. *Nat. Rev. Mol. Cell Biol.*, 6:21–31, Jan 2005.

[75] G. Guigas, C. Kalla, and M. Weiss. Probing the nanoscale viscoelasticity of intracellular fluids in living cells. *Biophys. J.*, 93:316–323, Jul 2007.

[76] G. Guigas, C. Kalla, and M. Weiss. The degree of macromolecular crowding in the cytoplasm and nucleoplasm of mammalian cells is conserved. *FEBS Lett.*, 581:5094–5098, Oct 2007.

[77] G. Guigas and M. Weiss. Sampling the cell with anomalous diffusion - the discovery of slowness. *Biophys. J.*, 94:90–94, Jan 2008.

[78] C. Gurrieri, P. Capodieci, R. Bernardi, P.P. Scaglioni, K. Nafa, L.J. Rush, D.A. Verbel, C. Cordon-Cardo, and P.P. Pandolfi. Loss of the tumor suppressor PML in human cancers of multiple histologic origins. *J. Natl. Cancer Inst.*, 96:269–279, Feb 2004.

[79] A. Hagting, M. Jackman, K. Simpson, and J. Pines. Translocation of cyclin B1 to the nucleus at prophase requires a phosphorylation-dependent nuclear import signal. *Curr. Biol.*, 9:680–689, Jul 1999.

[80] A. Hagting, M. Jackman, K. Simpson, and J. Pines. Translocation of cyclin B1 to the nucleus at prophase requires a phosphorylation-dependent nuclear import signal. *Curr. Biol.*, 9:680–689, Jul 1999.

[81] E. Haustein and P. Schwille. Fluorescence correlation spectroscopy: novel variations of an established technique. *Annu Rev Biophys Biomol Struct*, 36:151–169, 2007.

[82] E. Haustein and P. Schwille. Fluorescence correlation spectroscopy: novel variations of an established technique. *Annu Rev Biophys Biomol Struct*, 36:151–169, 2007.

[83] D. J. Heeger. Optical flow using spatiotemporal filters. *Int. J. Comp. Vision*, 1:279–302, 1988.

[84] B. Hein, K.I. Willig, and S.W. Hell. Stimulated emission depletion (STED) nanoscopy of a fluorescent protein-labeled organelle inside a living cell. *Proc. Natl. Acad. Sci. U.S.A.*, 105:14271–14276, Sep 2008.

[85] S.W. Hell. Toward fluorescence nanoscopy. *Nat. Biotechnol.*, 21:1347–1355, Nov 2003.

[86] J.E. Herrera, K.L. West, R.L. Schiltz, Y. Nakatani, and M. Bustin. Histone H1 is a specific repressor of core histone acetylation in chromatin. *Mol. Cell. Biol.*, 20:523–529, Jan 2000.

[87] D.A. Hill and A.N. Imbalzano. Human SWI/SNF nucleosome remodeling activity is partially inhibited by linker histone H1. *Biochemistry*, 39:11649–11656, Sep 2000.

[88] B. K. P. Horn and B. Schunk. Determining optical flow. *Artificial Intelligence*, 17:73–101, 1981.

[89] IEEE Conference on Computer Vision and Pattern Recognition. *Vector-Valued Image Regularization with PDE's: A Common Framework for Different Applications*, June 2003.

[90] M. Jackman, C. Lindon, E.A. Nigg, and J. Pines. Active cyclin B1-Cdk1 first appears on centrosomes in prophase. *Nat. Cell Biol.*, 5:143–148, Feb 2003.

[91] S. Jia, K. Noma, and S.I. Grewal. RNAi-independent heterochromatin nucleation by the stress-activated ATF/CREB family proteins. *Science*, 304:1971–1976, Jun 2004.

[92] T. Kamitani, K. Kito, H.P. Nguyen, T. Fukuda-Kamitani, and E.T. Yeh. Characterization of a second member of the sentrin family of ubiquitin-like proteins. *J. Biol. Chem.*, 273:11349–11353, May 1998.

[93] T. Kamitani, H.P. Nguyen, K. Kito, T. Fukuda-Kamitani, and E.T. Yeh. Covalent modification of PML by the sentrin family of ubiquitin-like proteins. *J. Biol. Chem.*, 273:3117–3120, Feb 1998.

[94] S. Khochbin. Histone H1 diversity: bridging regulatory signals to linker histone function. *Gene*, 271:1–12, Jun 2001.

[95] S. Khochbin and A.P. Wolffe. Developmentally regulated expression of linker-histone variants in vertebrates. *Eur. J. Biochem.*, 225:501–510, Oct 1994.

[96] R.W. King, R.J. Deshaies, J.M. Peters, and M.W. Kirschner. How proteolysis drives the cell cycle. *Science*, 274:1652–1659, Dec 1996.

[97] N. Klonis, M. Rug, I. Harper, M. Wickham, A. Cowman, and L. Tilley. Fluorescence photobleaching analysis for the study of cellular dynamics. *Eur. Biophys. J.*, 31:36–51, Mar 2002.

[98] M.H. Koken, G. Linares-Cruz, F. Quignon, A. Viron, M.K. Chelbi-Alix, J. Sobczak-Thépot, L. Juhlin, L. Degos, F. Calvo, and H. de Thé. The PML growth-suppressor has an altered expression in human oncogenesis. *Oncogene*, 10:1315–1324, Apr 1995.

[99] D.E. Koppel, D. Axelrod, J. Schlessinger, E.L. Elson, and W.W. Webb. Dynamics of fluorescence marker concentration as a probe of mobility. *Biophys. J.*, 16:1315–1329, Nov 1976.

[100] V. Kudryavtsev, S. Felekyan, A.K. WoÅºniak, M. KÃ¶nig, C. Sandhagen, R. KÃ¼hnemuth, C.A. Seidel, and F. Oesterhelt. Monitoring dynamic systems with multiparameter fluorescence imaging. *Anal Bioanal Chem*, 387:71–82, Jan 2007.

[101] B. Le Douarin, A.L. Nielsen, J.M. Garnier, H. Ichinose, F. Jeanmougin, R. Losson, and P. Chambon. A possible involvement of TIF1 alpha and TIF1 beta in the epigenetic control of transcription by nuclear receptors. *EMBO J.*, 15:6701–6715, Dec 1996.

[102] T. Lele, S.R. Wagner, J.A. Nickerson, and D.E. Ingber. Methods for measuring rates of protein binding to insoluble scaffolds in living cells: histone H1-chromatin interactions. *J. Cell. Biochem.*, 99:1334–1342, Dec 2006.

[103] T.P. Lele and D.E. Ingber. A mathematical model to determine molecular kinetic rate constants under non-steady state conditions using fluorescence recovery after photobleaching (FRAP). *Biophys. Chem.*, 120:32–35, Mar 2006.

[104] P. Lénárt, C.P. Bacher, N. Daigle, A.R. Hand, R. Eils, M. Terasaki, and J. Ellenberg. A contractile nuclear actin network drives chromosome congression in oocytes. *Nature*, 436:812–818, Aug 2005.

[105] A.K. Leung, D. Gerlich, G. Miller, C. Lyon, Y.W. Lam, D. Lleres, N. Daigle, J. Zomerdijk, J. Ellenberg, and A.I. Lamond. Quantitative kinetic analysis of nucleolar breakdown and reassembly during mitosis in live human cells. *J. Cell Biol.*, 166:787–800, Sep 2004.

[106] J. Lippincott-Schwartz, N. Altan-Bonnet, and G.H. Patterson. Photobleaching and photoactivation: following protein dynamics in living cells. *Nat. Cell Biol.*, Suppl:7–14, Sep 2003.

[107] J. Lippincott-Schwartz, E. Snapp, and A. Kenworthy. Studying protein dynamics in living cells. *Nat. Rev. Mol. Cell Biol.*, 2:444–456, Jun 2001.

[108] K. Luger, A.W. Mäder, R.K. Richmond, D.F. Sargent, and T.J. Richmond. Crystal structure of the nucleosome core particle at 2.8 A resolution. *Nature*, 389:251–260, Sep 1997.

[109] H.-G. Maas. Digital photogrammetry for determination of tracer particle coordinates in turbulent flow research. *Photogrammatic Engineering & Remote Sensing*, 57(12):1593–1597, 1991.

[110] H.-G. Maas. *Digitale Photogrammetrie in der dreidimensionalen Strömungsmesstechnik*. PhD thesis, ETH Zürich, 1992.

[111] D. Magde, E.L. Elson, and W.W. Webb. Fluorescence correlation spectroscopy. II. An experimental realization. *Biopolymers*, 13:29–61, Jan 1974.

[112] N.L. Mahy, P.E. Perry, and W.A. Bickmore. Gene density and transcription influence the localization of chromatin outside of chromosome territories detectable by FISH. *J. Cell Biol.*, 159:753–763, Dec 2002.

[113] N.L. Mahy, P.E. Perry, S. Gilchrist, R.A. Baldock, and W.A. Bickmore. Spatial organization of active and inactive genes and noncoding DNA within chromosome territories. *J. Cell Biol.*, 157:579–589, May 2002.

[114] A. Marcello, A. Ferrari, V. Pellegrini, G. Pegoraro, M. Lusic, F. Beltram, and M. Giacca. Recruitment of human cyclin T1 to nuclear bodies through direct interaction with the PML protein. *EMBO J.*, 22:2156–2166, May 2003.

[115] M.J. Matunis, X.D. Zhang, and N.A. Ellis. SUMO: the glue that binds. *Dev. Cell*, 11:596–597, Nov 2006.

[116] D. MAZIA. How cells divide. *Sci. Am.*, 205:100–120, Sep 1961.

[117] O. Medalia, I. Weber, A.S. Frangakis, D. Nicastro, G. Gerisch, and W. Baumeister. Macromolecular architecture in eukaryotic cells vi-

sualized by cryoelectron tomography. *Science*, 298:1209–1213, Nov 2002.

[118] E. Meijering. Featurej - a java package for image feature extraction.

[119] A. Michelson. *Studies in Optics*. U. of Chicago Press, 1927.

[120] T. Misteli. Protein dynamics: implications for nuclear architecture and gene expression. *Science*, 291:843–847, Feb 2001.

[121] T. Misteli, A. Gunjan, R. Hock, M. Bustin, and D.T. Brown. Dynamic binding of histone H1 to chromatin in living cells. *Nature*, 408:877–881, Dec 2000.

[122] W.E. Moerner. New directions in single-molecule imaging and analysis. *Proc. Natl. Acad. Sci. U.S.A.*, 104:12596–12602, Jul 2007.

[123] D. Montiel, H. Cang, and H. Yang. Quantitative characterization of changes in dynamical behavior for single-particle tracking studies. *J Phys Chem B*, 110:19763–19770, Oct 2006.

[124] S. Müller, M.J. Matunis, and A. Dejean. Conjugation with the ubiquitin-related modifier SUMO-1 regulates the partitioning of PML within the nucleus. *EMBO J.*, 17:61–70, Jan 1998.

[125] M. Muratani, D. Gerlich, S.M. Janicki, M. Gebhard, R. Eils, and D.L. Spector. Metabolic-energy-dependent movement of PML bodies within the mammalian cell nucleus. *Nat. Cell Biol.*, 4:106–110, Feb 2002.

[126] A. Murray and T. Hunt. *The Cell Cycle: An Introduction.* W. H. Freeman and Company, 1993.

[127] J. Reece N. Campbell. *The Cell Cycle, Biology*. Benjamin Cummings/Addison-Wesley, 6 edition, 2001.

[128] H.-H. Nagel. Displacement vectors derived from second-order intensity variations in image sequences. *Computer Graphics and Image Processing*, 21:85–117, 1983.

[129] J. Nakayama, J.C. Rice, B.D. Strahl, C.D. Allis, and S.I. Grewal. Role of histone H3 lysine 9 methylation in epigenetic control of heterochromatin assembly. *Science*, 292:110–113, Apr 2001.

[130] K. Nasmyth. Viewpoint: putting the cell cycle in order. *Science*, 274:1643–1645, Dec 1996.

[131] K. Noma, T. Sugiyama, H. Cam, A. Verdel, M. Zofall, S. Jia, D. Moazed, and S.I. Grewal. RITS acts in cis to promote RNA interference-mediated transcriptional and post-transcriptional silencing. *Nat. Genet.*, 36:1174–1180, Nov 2004.

[132] P. Nurse. Checkpoint pathways come of age. *Cell*, 91:865–867, Dec 1997.

[133] R. Ohi and K.L. Gould. Regulating the onset of mitosis. *Curr. Opin. Cell Biol.*, 11:267–273, Apr 1999.

[134] Kazuo Ohmi. Particle-tracking velocimetry with new algorithms. *Sci. Technol.*, 11:603–616, 2000.

[135] R.D. Phair and T. Misteli. High mobility of proteins in the mammalian cell nucleus. *Nature*, 404:604–609, Apr 2000.

[136] J. Pines and C.L. Rieder. Re-staging mitosis: a contemporary view of mitotic progression. *Nat. Cell Biol.*, 3:3–6, Jan 2001.

[137] D.W. Piston and G.J. Kremers. Fluorescent protein FRET: the good, the bad and the ugly. *Trends Biochem. Sci.*, 32:407–414, Sep 2007.

[138] M. Platani, I. Goldberg, A.I. Lamond, and J.R. Swedlow. Cajal body dynamics and association with chromatin are ATP-dependent. *Nat. Cell Biol.*, 4:502–508, Jul 2002.

[139] G. Rabut, V. Doye, and J. Ellenberg. Mapping the dynamic organization of the nuclear pore complex inside single living cells. *Nat. Cell Biol.*, 6:1114–1121, Nov 2004.

[140] A. R. Rao and B. G. Schunck. Computing oriented texture fields. *CVGIP: Graphical Models and Image Processing*, 53(2):157–185, 1991.

[141] T. Regad and M.K. Chelbi-Alix. Role and fate of PML nuclear bodies in response to interferon and viral infections. *Oncogene*, 20:7274–7286, Oct 2001.

[142] E.A. Reits and J.J. Neefjes. From fixed to FRAP: measuring protein mobility and activity in living cells. *Nat. Cell Biol.*, 3:E145–147, Jun 2001.

[143] E.J. Richards and S.C. Elgin. Epigenetic codes for heterochromatin formation and silencing: rounding up the usual suspects. *Cell*, 108:489–500, Feb 2002.

[144] C.L. Rieder and R.W. Cole. Entry into mitosis in vertebrate somatic cells is guarded by a chromosome damage checkpoint that reverses the cell cycle when triggered during early but not late prophase. *J. Cell Biol.*, 142:1013–1022, Aug 1998.

[145] R. Rigler and M. Ehrenberg. Molecular interactions and structure as analysed by fluorescence relaxation spectroscopy. *Q. Rev. Biophys.*, 6:139–199, May 1973.

[146] R. Rigler and M. Ehrenberg. Fluorescence relaxation spectroscopy in the analysis of macromolecular structure and motion. *Q. Rev. Biophys.*, 9:1–19, Feb 1976.

[147] H. Rinia, K.N. Burger, M. Bonn, and M. Müller. Quantitative label-free imaging of lipid composition and packing of individual cellular lipid droplets using multiplex CARS microscopy. *Biophys. J.*, Aug 2008.

[148] L.G. Rodriguez, S.J. Lockett, and G.R. Holtom. Coherent anti-stokes Raman scattering microscopy: a biological review. *Cytometry A*, 69:779–791, Aug 2006.

[149] K. Rohr. On 3d differential operators for detecting point landmarks. *Image and Vision Computing*, 15(3):219–233, 1997.

[150] K. Rohr, H. S. Stiehl, R. Sprengel, T. M. Buzug, J. Weese, and M. H. Kuhn. Landmark-based elastic registration using approximating thin-plate splines, Jun 2001.

[151] U. Rothbauer, K. Zolghadr, S. Tillib, D. Nowak, L. Schermelleh, A. Gahl, N. Backmann, K. Conrath, S. Muyldermans, M.C. Cardoso, and H. Leonhardt. Targeting and tracing antigens in live cells with fluorescent nanobodies. *Nat. Methods*, 3:887–889, Nov 2006.

[152] J.D. Rowley, H.M. Golomb, and C. Dougherty. 15/17 translocation, a consistent chromosomal change in acute promyelocytic leukaemia. *Lancet*, 1:549–550, Mar 1977.

[153] P. Salomoni and P.P. Pandolfi. The role of PML in tumor suppression. *Cell*, 108:165–170, Jan 2002.

[154] M.J. Saxton. Lateral diffusion in an archipelago. Dependence on tracer size. *Biophys. J.*, 64:1053–1062, Apr 1993.

[155] M.J. Saxton. Lateral diffusion in an archipelago. Single-particle diffusion. *Biophys. J.*, 64:1766–1780, Jun 1993.

[156] M.J. Saxton. Chemically limited reactions on a percolation cluster. *J. Chem. Phys.*, 116:203–205, 2002.

[157] I.F. Sbalzarini, A. Mezzacasa, A. Helenius, and P. Koumoutsakos. Effects of organelle shape on fluorescence recovery after photobleaching. *Biophys. J.*, 89:1482–1492, Sep 2005.

[158] J.S. Seeler, A. Marchio, D. Sitterlin, C. Transy, and A. Dejean. Interaction of SP100 with HP1 proteins: a link between the promyelocytic leukemia-associated nuclear bodies and the chromatin compartment. *Proc. Natl. Acad. Sci. U.S.A.*, 95:7316–7321, Jun 1998.

[159] N.C. Shaner, P.A. Steinbach, and R.Y. Tsien. A guide to choosing fluorescent proteins. *Nat. Methods*, 2:905–909, Dec 2005.

[160] T.H. Shen, H.K. Lin, P.P. Scaglioni, T.M. Yung, and P.P. Pandolfi. The mechanisms of PML-nuclear body formation. *Mol. Cell*, 24:331–339, Nov 2006.

[161] E.D. Siggia, J. Lippincott-Schwartz, and S. Bekiranov. Diffusion in inhomogeneous media: theory and simulations applied to whole cell photobleach recovery. *Biophys. J.*, 79:1761–1770, Oct 2000.

[162] S. Simonsson and J. Gurdon. DNA demethylation is necessary for the epigenetic reprogramming of somatic cell nuclei. *Nat. Cell Biol.*, 6:984–990, Oct 2004.

[163] M. Smoluchowski. Zur kinetischen theorie der brownschen molekularbewegung und der suspensionen. *Annalen der Physik*, 21:756–780, 1906.

[164] E.L. Snapp, N. Altan, and J. Lippincott-Schwartz. Measuring protein mobility by photobleaching GFP chimeras in living cells. *Curr Protoc Cell Biol*, Chapter 21:Unit 21.1, Aug 2003.

[165] D.M. Soumpasis. Theoretical analysis of fluorescence photobleaching recovery experiments. *Biophys. J.*, 41:95–97, Jan 1983.

[166] D.L. Spector. Nuclear domains. *J. Cell. Sci.*, 114:2891–2893, Aug 2001.

[167] B.L. Sprague and J.G. McNally. FRAP analysis of binding: proper and fitting. *Trends Cell Biol.*, 15:84–91, Feb 2005.

[168] B.L. Sprague, F. Müller, R.L. Pego, P.M. Bungay, D.A. Stavreva, and J.G. McNally. Analysis of binding at a single spatially localized cluster of binding sites by fluorescence recovery after photobleaching. *Biophys. J.*, 91:1169–1191, Aug 2006.

[169] B.L. Sprague, R.L. Pego, D.A. Stavreva, and J.G. McNally. Analysis of binding reactions by fluorescence recovery after photobleaching. *Biophys. J.*, 86:3473–3495, Jun 2004.

[170] T. Sternsdorf, K. Jensen, and H. Will. Evidence for covalent modification of the nuclear dot-associated proteins PML and Sp100 by PIC1/SUMO-1. *J. Cell Biol.*, 139:1621–1634, Dec 1997.

[171] T. Sternsdorf, K. Jensen, D. Züchner, and H. Will. Cellular localization, expression, and structure of the nuclear dot protein 52. *J. Cell Biol.*, 138:435–448, Jul 1997.

[172] F. Strauss and A. Prunell. Nucleosome spacing in rat liver chromatin. A study with exonuclease III. *Nucleic Acids Res.*, 10:2275–2293, Apr 1982.

[173] N. Stuurman, A. de Graaf, A. Floore, A. Josso, B. Humbel, L. de Jong, and R. van Driel. A monoclonal antibody recognizing nuclear matrix-associated nuclear bodies. *J. Cell. Sci.*, 101 (Pt 4):773–784, Apr 1992.

[174] C. Szent-Gyorgyi, B.F. Schmidt, B.A. Schmidt, Y. Creeger, G.W. Fisher, K.L. Zakel, S. Adler, J.A. Fitzpatrick, C.A. Woolford, Q. Yan, K.V. Vasilev, P.B. Berget, M.P. Bruchez, J.W. Jarvik, and A. Waggoner. Fluorogen-activating single-chain antibodies for imaging cell surface proteins. *Nat. Biotechnol.*, 26:235–240, Feb 2008.

[175] C.G. Takizawa and D.O. Morgan. Control of mitosis by changes in the subcellular location of cyclin-B1-Cdk1 and Cdc25C. *Curr. Opin. Cell Biol.*, 12:658–665, Dec 2000.

[176] C.W. Tang, A. Maya-Mendoza, C. Martin, K. Zeng, S. Chen, D. Feret, S.A. Wilson, and D.A. Jackson. The integrity of a lamin-B1-dependent nucleoskeleton is a fundamental determinant of RNA synthesis in human cells. *J. Cell. Sci.*, 121:1014–1024, Apr 2008.

[177] B. Terris, V. Baldin, S. Dubois, C. Degott, J.F. Flejou, D. Hénin, and A. Dejean. PML nuclear bodies are general targets for inflammation and cell proliferation. *Cancer Res.*, 55:1590–1597, Apr 1995.

[178] L. Trinkle-Mulcahy and A.I. Lamond. Toward a high-resolution view of nuclear dynamics. *Science*, 318:1402–1407, Nov 2007.

[179] L. Trinkle-Mulcahy and A.I. Lamond. Toward a high-resolution view of nuclear dynamics. *Science*, 318:1402–1407, Nov 2007.

[180] W. Tvaruskó, M. Bentele, T. Misteli, R. Rudolf, C. Kaether, D.L. Spector, H.H. Gerdes, and R. Eils. Time-resolved analysis and visualization of dynamic processes in living cells. *Proc. Natl. Acad. Sci. U.S.A.*, 96:7950–7955, Jul 1999.

[181] M. Ulrich, C. Kappel, J. Beaudouin, S. Hezel, J. Ulrich, and R. Eils. Tropical–parameter estimation and simulation of reaction-diffusion models based on spatio-temporal microscopy images. *Bioinformatics*, 22:2709–2710, Nov 2006.

[182] Markus Ulrich. *Tropical - software for quantitative analysis of FRAP experiments*. PhD thesis, Universität Heidelberg, 2008.

[183] P.J. Verschure, I. van Der Kraan, E.M. Manders, and R. van Driel. Spatial relationship between transcription sites and chromosome territories. *J. Cell Biol.*, 147:13–24, Oct 1999.

[184] A.E. Visser, F. Jaunin, S. Fakan, and J.A. Aten. High resolution analysis of interphase chromosome domains. *J. Cell. Sci.*, 113 (Pt 14):2585–2593, Jul 2000.

[185] E.V. Volpi, E. Chevret, T. Jones, R. Vatcheva, J. Williamson, S. Beck, R.D. Campbell, M. Goldsworthy, S.H. Powis, J. Ragoussis, J. Trowsdale, and D. Sheer. Large-scale chromatin organization of the major histocompatibility complex and other regions of human chromosome 6 and its response to interferon in interphase nuclei. *J. Cell. Sci.*, 113 (Pt 9):1565–1576, May 2000.

[186] M. Wachsmuth, W. Waldeck, and J. Langowski. Anomalous diffusion of fluorescent probes inside living cell nuclei investigated by spatially-resolved fluorescence correlation spectroscopy. *J. Mol. Biol.*, 298:677–689, May 2000.

[187] M. Wachsmuth, T. Weidemann, G. Müller, U.W. Hoffmann-Rohrer, T.A. Knoch, W. Waldeck, and J. Langowski. Analyzing intracellular binding and diffusion with continuous fluorescence photobleaching. *Biophys. J.*, 84:3353–3363, May 2003.

[188] Y.L. Wang, K.M. Hahn, R.F. Murphy, and A.F. Horwitz. From imaging to understanding: Frontiers in Live Cell Imaging, Bethesda, MD, April 19-21, 2006. *J. Cell Biol.*, 174:481–484, Aug 2006.

[189] L.P. Watkins and H. Yang. Detection of intensity change points in time-resolved single-molecule measurements. *J Phys Chem B*, 109:617–628, Jan 2005.

[190] J. Weickert. Coherence-enhancing diffusion filtering. *Int. J. Comp. Vision*, 31(2):111–127, 1999.

[191] T. Weidemann, M. Wachsmuth, T.A. Knoch, G. Müller, W. Waldeck, and J. Langowski. Counting nucleosomes in living cells with a combination of fluorescence correlation spectroscopy and confocal imaging. *J. Mol. Biol.*, 334:229–240, Nov 2003.

[192] M. Weiss, M. Elsner, F. Kartberg, and T. Nilsson. Anomalous subdiffusion is a measure for cytoplasmic crowding in living cells. *Biophys. J.*, 87:3518–3524, Nov 2004.

[193] M. Weiss, M. Elsner, F. Kartberg, and T. Nilsson. Anomalous subdiffusion is a measure for cytoplasmic crowding in living cells. *Biophys. J.*, 87:3518–3524, Nov 2004.

[194] M. Weiss, H. Hashimoto, and T. Nilsson. Anomalous protein diffusion in living cells as seen by fluorescence correlation spectroscopy. *Biophys. J.*, 84:4043–4052, Jun 2003.

[195] F.S. Wouters, P.J. Verveer, and P.I. Bastiaens. Imaging biochemistry inside cells. *Trends Cell Biol.*, 11:203–211, May 2001.

[196] X.S. Xie, J. Yu, and W.Y. Yang. Living cells as test tubes. *Science*, 312:228–230, Apr 2006.

[197] Q. Ye and H.J. Worman. Interaction between an integral protein of the nuclear envelope inner membrane and human chromodomain proteins homologous to Drosophila HP1. *J. Biol. Chem.*, 271:14653–14656, Jun 1996.

[198] S. Zhong, P. Salomoni, and P.P. Pandolfi. The transcriptional role of PML and the nuclear body. *Nat. Cell Biol.*, 2:85–90, May 2000.

[199] A. Zumbusch, G.R. Holtom, and X.S. Xie. Three-dimensional vibrational imaging by coherent anti-stokes raman scattering. *phys rev let*, 82:4142–4145, 1999.